University of Arkansas, Fayetteville
ScholarWorks@UARK

Theses and Dissertations

5-2018

Near Bandgap Two-photon Excited Luminescence of InAs Quantum Dots

Xian Hu
University of Arkansas, Fayetteville

Follow this and additional works at: http://scholarworks.uark.edu/etd

 Part of the Optics Commons, and the Semiconductor and Optical Materials Commons

Recommended Citation
Hu, Xian, "Near Bandgap Two-photon Excited Luminescence of InAs Quantum Dots" (2018). *Theses and Dissertations*. 2748.
http://scholarworks.uark.edu/etd/2748

This Dissertation is brought to you for free and open access by ScholarWorks@UARK. It has been accepted for inclusion in Theses and Dissertations by an authorized administrator of ScholarWorks@UARK. For more information, please contact scholar@uark.edu, ccmiddle@uark.edu.

Near Bandgap Two-photon Excited Luminescence of InAs Quantum Dots

A dissertation submitted in partial fulfillment
of the requirements for the degree of
Doctor of Philosophy in Physics

by

Xian Hu
Soochow University
Bachelor of Science in Optical Information Science and Technology, 2010
University of Arkansas
Master of Science in Physics, 2015

May 2018
University of Arkansas

This dissertation is approved for recommendation to the Graduate Council.

Gregory J. Salamo, Ph.D.
Dissertation Director

Surendra P. Singh, Ph.D.
Committee Member

Laurent Bellaiche, Ph.D.
Committee Member

Shui-Qing Yu, Ph.D.
Committee Member

Salvador Barraza-Lopez, Ph.D.
Committee Member

Abstract

Semiconductor quantum dots (QDs) confine carriers in three dimensions, resulting in atomic-like energy levels as well as size-dependent electrical and optical properties. Self-assembled III-V QD is one of the most studied semiconductor QDs thanks to their well-established fabrication techniques and versatile optical properties. This dissertation presents the photoluminescence (PL) study of the InAs/GaAs QDs with both above bandgap continuous-wave excitation (one-photon excitation) and below-bandgap pulse excitation (two-photon excitation). Samples of ensemble QDs, single QD (SQD), and QDs in a micro-cavity, all grown by molecular beam epitaxy, are used in this study. Morphology of these samples was examined using atomic force microscope and transmission electron microscope. Two-photon excitation uses energy near half of the QDs ground state transition, all the way up to half of the GaAs matrix bandgap. Power dependent QDs PL with both one-photon and two-photon excitation can be described by power laws, with power index of 1 for one-photon excitation and two for two-photon excitation. Photoluminescence excitation spectroscopy then provides evidence of direct two-photon absorption into the QDs when the two-photon excitation energy is resonant with the QDs state. For SQD without cavity, we observed PL of a SQD with excitation near its half bandgap. The QDs in a micro-cavity sample consists one layer of InAs QDs in a GaAs spacer sandwiched between two distributed Bragg reflectors made of alternating layers of GaAs and AlAs. We successfully observed PL from SQD emitted from the cavity mode with excitation slightly above half of the QD's transition. These observations help us to understand the nonlinear optical property of InAs QDs and can be potentially used in all-optical computation or reflective optical limiters.

Acknowledgements

Fayetteville is a lovely place and I am grateful for the opportunity to study at the University of Arkansas. My study and life here would not be this enjoyable without the help of many nice people. And I find it is difficult for this limited acknowledgment list and my imperfect English to fully express my appreciation for all of them.

First and foremost, I would like to give my deepest thanks to my advisor, Prof. Gregory Salamo, for the tremendous help and encouragement he provided during my Ph.D. study. I could not even imagine getting through all the challenges and difficulties without his support. His passion and attitude about physics set a positive research environment in our group which I feel very lucky to work in. Prof. Salamo is also a wonderful mentor and role model. What I learned from him these years is not only the enthusiasm for working but also the kindness for people.

I would like to thank Prof. Surendra P. Singh, Prof. Laurent Bellaiche, Prof. Shui-Qing Yu, and Prof. Salvador Barraza-Lopez for being on my committee. I am grateful for their time and support during my Ph.D. study.

I would like to give special thanks to Dr. Wolfgang Braun from Arizona State University for his java program that I used for simulation of cavity.

This work would not have been done with the help of my research group colleagues. I'm deeply grateful to Dr. Dorel Guzun, for his knowledge of optics and skills in optical setups. We spent a lot of fun time in the lab together. Prof. Morgan E. Ware has been very nice and supportive during these years. He taught me to use the Horiba LabRAM system and the Shimadzu 3600uv system. We also had a lot of discussion about the single quantum dot. I'm grateful for his patience and kindness. Dr. Yuriy I. Mazur is "the boss" of our optics lab. I am grateful for his coordination in the lab and the motivation he had on me. Dr. Mourad Benamara

is the expert on electron microscopes. I thank him for all the knowledge and skill about the microscopes that he taught me and the help he provided on transmission electron microscope. I also want to thank Dr. Vasyl Kunets for teaching me molecular beam epitaxy growth. His rigorous towards research sets a very good example for all the students who work with him. Many thanks go to Yusuke Hirono, who assisted with all my samples' growth, including the 12-hour-long cavity samples' growth. His industrious and approach towards science impresses me a lot. I would like to thank Timothy Morgan for his training on microscope sample preparation and research discussion. Many thanks go to Dr. Robert Sleezer for atomic force microscope training and continuous encouragement. My appreciation goes to my group member Chen Li and Sabina Koukourinkova for their moral support. Great appreciation goes to my dear friend and labmate Yang Wu. Her optimism always cheers me up. The friendship we developed during our Ph.D. study would definitely go further in our life.

Last but not the least, I would like to thank my family. My parents Yuan Hu, and Rongying Zhang provide me with good education and freedom. They always have trust in me and support whatever decision I made. My husband, Anindy Ambuj, has been the closet comrade during my Ph.D. study. He has always been there for me when there were tough times and together we made this Ph.D. journey beautiful. Ash, our blessed son, is always the happiest person in the house. He is our bringer of hope and his lovely smile is the magical treatment for any negative emotion. At last, I would like to thank my grandpa, Zheng Hu. He could not finish his Ph.D. in the U.S. due to the unstable situation in China in the 1950s. But he always encouraged his descendants and students to pursuit study overseas. Although I did not have the chance to discuss quantum physics or electronics with him, I hope he could be proud of me for finishing my Ph.D. study.

Table of Contents

1 Introduction 1

2 Background 5

2.1 Sample and Growth 5

2.1.1 QDs Sample Description and Growth 5

2.1.2 QDs-in-cavity Sample Design and Growth 9

2.2 Energy Structure of Quantum Dots and Carrier Relaxation Process 10

2.3 Rate Equation Model for Excitation Power Dependent PL 12

2.4 Two-photon Absorption 16

2.5 Distributed Bragg Reflector and Cavity Mode 21

3 Photoluminescence of Ensemble Quantum Dots 24

3.1 Sample Morphology and PL Characterization 24

3.2 One-photon Excited Power Dependent PL of EQDs 28

3.3 Two-photon Excited Power Dependent PL of EQDs 30

3.4 Two-photon Excited Power Dependent PL of WL and GaAs 34

3.5 Two-photon PLE of EQDs 37

4 Photoluminescence of Single Quantum Dot 40

4.1 Sample Morphology and PL Characterization 40

4.2 One-photon Excited Power Dependent PL of SQD 42

4.3 One-photon Excited Temperature Dependent PL of SQD 44

4.4 Two-photon Excited PL of SQD 47

5 Photoluminescence of Single Quantum Dot in Micro-Cavity 52

5.1 Sample Morphology, Reflectance and PL Characterization 52

5.2 One-photon Excited Power Dependent PL of SQD-in-cavity 54
5.3 One-photon Excited Temperature Dependent PL of SQD-in-cavity 57
5.4 Two-photon Excited PL of SQD-in-cavity 59
6 Conclusion and Outlook 61
Reference 64
Appendix 71
A. Molecular Beam Epitaxy 71
B. AFM Characterization 74
C. TEM Characterization 79
D. PL & PLE Measurement Setup 81
E. Two-photon Excitation Source System 84
F. Publication list 86

List of Figures

Figure 2.1. RHEED patterns (left panel) and their corresponding growth process (right panel) [38] 6

Figure 2.2. Structure diagram of a QDs-in-cavity sample. 10

Figure 2.3. (a) Schematic of the energy levels of an InAs/GaAs QD system. 11

Figure 2.4. Energy diagram of a QD system. Radiative transitions are indicated by straight arrows while non-radiative transitions are indicated by curved arrows. 12

Figure 2.5. Diagrams of three types of TPA: (a) direct TPA; (b) indirect TPA; (c) Auger-type process. 17

Figure 2.6. (a) Reflectance for different number of GaAs/AlAs DBR pairs. (b) Wavelength-dependent reflectance for 25 GaAs/AlAs DBR pairs designed for 1μm. 22

Figure 2.7. (a) Simulation (magenta) and experimental (black) results of the reflectance of sample SF078. (b) Experimental reflectance (black) of sample SF078 and photoluminescence of the same sample at RT (black) and 10K (red). 23

Figure 3.1. $1\times1\mu m^2$ AFM image of SF094 at different positions (left panel) and their corresponding QDs height histograms (right panel). (a) p2, (c) p6, (e) p7, (g) p8, (i) p5. 25

Figure 3.2. Photoluminescence spectra of sample SF094 with gradient QDs at 9 different locations (L5-L13) on sample along the indium flux gradient. 27

Figure 3.3 Normalized 1hυ excited PL spectra of EQDs with varying excitation power. 100% power equals to I_{10} ~ 6mW. 29

Figure 3.4. (a) Excitation power dependent integrated PL intensity of EQDs with 1hυ excitation. Red line is the power law fitting: $PL = a \cdot I^s$ with power index s = 1.07. 30

Figure 3.5. Normalized 2hυ excited PL spectra of EQDs with 0.622eV excitation. 33

Figure 3.6. (a) Excitation power dependent integrated PL intensity of EQDs with 0.622eV excitation. Red line is the power law fitting: $PL = a \cdot I^s$ with power index s = 2.19. (b) Power law index of multiple EQDs samples at various 2hυ excitation energies. .. 33

Figure 3.7. (a) One-photon excitation power dependent integrated PL intensity of WL and GaAs substrate. Straight line is the power law fitting: $PL = a \cdot I^s$ with power index s = 1.72 for WL and 2.02 for GaAs substrate. (b) Power law indexes of multiple WL samples and GaAs substrate samples. Error bars present the standard error of power law fitting. 34

Figure 3.8.Two-photon excited PL spectra of (a) WL only area of SF094 and (b) GaAs substrate with 2hυ excitation energy of 1.244eV. 35

Figure 3.9. (a) Excitation power dependent integrated PL intensity of WL and GaAs substrate with 1.244eV excitation. Straight line is the power law fitting: $PL = a \cdot I^s$ with power index s = 3.87 for WL and 4.92 for GaAs. (b) Power law index of WL and GaAs at various 2hυ excitation energies. 36

Figure 3.10. Integrated QDs PL as a function of 2hυ excitation energy. 38

Figure 4.1. TEM image of a single InAs/GaAs QD. 40

Figure 4.2. PL spectrum of a SQD at 5K. 41

Figure 4.3. Normalized 1hυ excited PL spectra of SQD with varying excitation power. 100% power equals to I_{10} ~ 6mW. 42

Figure 4.4. Excitation power dependent integrated PL intensity of four SQD peaks with 1hυ excitation. Straight line is the power law fitting: $PL = a \cdot I^s$ with power index s = 0.95 for s-shell X, 1.22 for s-shell X*, 1.10 for p-shell X, and 1.26 for p-shell X*. 43

Figure 4.5. Normalized temperature dependent SQD PL with 1hυ excitation. 45
Figure 4.6. (a) FWHM and (b) peak center of the X and X* peaks in S-shall and P-shell as a function of temperature. Solid lines are fitting functions: 46
Figure 4.7. SQD spectra with various 2hυ excitation energies at 5K. 48
Figure 4.8. SQD PL with 2hυ excitation at two powers. PL with 1hυ excitation is plotted for comparison. 49
Figure 4.9. Two-photon excited SQD PL at various temperatures. The bottom red curve is 1hυ excited SQD PL at 10K, plotted for comparison. 50
Figure 4.10. Ground transition (gray area in Figure 4.9) peak position as a function of temperature. Solid line is the fitting function by Varshni Law as in Eq.(4.2). 51
Figure 5.1. (a) TEM image of QDs-in-cavity sample. (b) Zoom in image of the cavity. 52
Figure 5.2. Simulated and measured reflectance spectrum of SF096. 53
Figure 5.3. PL from different positions on SF096. Insert shows the rough positions on the sample. Dashed line is the quarter-inch wafer and solid line is where the sample was cleaved. 54
Figure 5.4. Normalized PL spectra of SQD-in-cavity at different 1hυ excitation powers. 100% power equals to I_{10} ~ 6mW. 55
Figure 5.5. Excitation power dependent integrated PL intensity of a SQD-in-cavity at 10K. 56
Figure 5.6. Normalized 1hυ excited temperature dependent PL of a SQD-in-cavity. 57
Figure 5.7. Varshni Law fit of the center position of p1, p2, and p3. 58
Figure 5.8. Normalized PL of SQD-in-cavity at various 2hυ and 1hυ excitation powers. 60
Figure A.1. Schematic diagram of a typical MBE growth chamber (top view) [A1]. 71
Figure A.2. Photo of Riber 32P MBE (taken by author). 72

Figure B.1. Basic AFM tapping mode working principal. 74
Figure B.2. Photo of Veeco Dimension V AFM (taken by author). 75
Figure B.3. (a) AFM image of SF044 and (b) cross-section of QDs structure. (c) Histogram of height and diameter of QDs in (a). 76
Figure B.4. AFM image of SF046 at (a) p5, (b) p4, (c) p3. (d) Height histogram of QDs at these three positions. 77
Figure C.1. Simplified schematics of TEM. 79
Figure C.2. Photo of Titan TEM (taken by author). 80
Figure D.1. Schematic of Horiba LabRAM HR800 system. 81
Figure D.2. Photo of Horiba LabRAM HR800 system (taken by author). 82
Figure E.1.Two-photon excitation laser system. 84
Figure E.2. Spectra of the 2hυ excitation laser. 85

List of Tables

Table 2.1. QDs samples grown for this dissertation. 8

Table 2.2. Description and result for the cavity samples. 10

Table 4.1. Fitting parameters for each peak plotted in Figure 4.6 (a). 46

Table 4.2. Fitting parameters for each peak position as a function of temperature. 47

Table 5.1. Fitting parameters for each peak position as a function of temperature. 58

List of Abbreviations

1hυ	One-photon
2hυ	Two-photon
2D	Two-dimensional
3D	Three-dimensional
AFM	Atomic Force Microscopy
AlAs	Aluminum Arsenide
AlGaAs	Aluminum Gallium Arsenide
AlGaN	Aluminum Gallium Nitride
CB	Conduction Band
CCD	Charge-coupled device
DBR	Distributed Bragg Reflector
EQD	Ensemble Quantum Dot
FWHM	Full With at Half Maximum
GaAs	Gallium Arsenide
GaN	Gallium Nitride
He-Ne	Helium-Neon
IB	Intermediate Band
IBSC	Intermediate-band Solar Cells
InAs	Indium Arsenide
MBE	Molecular Beam Epitaxy
MEE	Migration-enhanced Epitaxy
ML	Monolayer

OPA	Optical Parametric Amplifier
PL	Photoluminescence
PLE	Photoluminescence Excitation
QD	Quantum Dot
RHEED	Reflection High Energy Electron Diffraction
SHG	Second Harmonic Generation
Si	Silicon
S.I.	Semi-insulating
SK	Stranski-Krastanov
SQD	Single Quantum Dot
TEM	Transmission Electron Microscopy
TPA	Two-photon Absorption
UHV	Ultra-High Vacuum
VB	Valence Band
WL	Wetting Layer

1 Introduction

Nanomaterials are objects or structures that are at the nanoscale. We have known that the same substance at the nanoscale has different properties from its bulk counterpart [1]. This is because when structures come down to the nanoscale, the physical size of the object is comparable to the de Broglie wavelength of a charge carrier, restricting the charge carrier's motion in specific energy levels. Therefore, nanomaterials open the door to a new world of materials. The properties of nanomaterials are not only different from those of their corresponding bulk, but they are also closely related to the materials' sizes and shapes [1], [2]. This tunability makes nanomaterial and nanotechnology one of the critical research fields of the 21st century.

Quantum dots (QDs) are particles at the nanoscale in all three dimensions. The term "quantum dots" was coined by Reed *et al.* [3] in 1985, when they first provided evidence of energy quantization in this completely spatially quantized system. The QDs in their study was made by electron-beam lithography of a heterojunction system grown by molecular beam epitaxy (MBE). Nowadays, QDs can be prepared in several ways, including colloidal synthesis [4], plasma synthesis [5], [6], epitaxial growth, fabrication, etc. Characterization of the fundamental electronic and optical properties of QDs as well as the development of new fabrication techniques have also been advanced since the QDs invention.

Optical nonlinearity of a material studies the modification of a material system's optical property by the incident light. This field remained unexplored until the invention of the laser in 1960 since the laser is intense enough, comparing to the atomic electric field, to cause the dielectric polarization to respond nonlinearly to the electric field of the illumination light. In return, the applications of lasers are greatly extended by the discovered optical nonlinearity of

material, including second harmonic generation (SHG), Q-switching, and mode-locking. Two-photon absorption (TPA), as a form of multi-photon absorption, is one of the important optical nonlinearities of material since it can dominate over linear absorption at high illumination intensities. During a TPA process, the material absorbs two photons at the same time. The transition energy equals the sum energy of these absorbed photons. Application of TPA can be found in many fields: microfabrication [7], [8], optical power limiting and stabilization [9], [10], three-dimensional imaging [11], to name a few.

Two-photon absorption by QDs has attracted a lot of research interest and have been studied across many disciplines because of its wide application. For example: material characterization by two-photon spectroscopy can use one laser as a fundamental pump and the other laser with variable energy to probe energy levels [12]–[14]; two-photon fluorescence for biological labeling and imaging [15], [16] uses infrared light to excite QDs so that a bigger penetration depth is achieved; intermediate-band solar cells (IBSC) [17]–[20] utilizes TPA through their intermediate-band to harvest infrared photons.

Epitaxial-grown QDs are one of the most interested semiconductor QDs due to their well-established fabrication techniques. As one of the most compelling nonlinear optical properties, TPA of III-V QDs has been investigated for fundamental physics as well as engineering applications. In this case, the two-photon excitation energy is focused mainly on above the inter-band transition or within the sub-band transition. For instance, two-photon spectral hole burning of QDs [21] and Rabi oscillation resulted from two-photon resonant excitation of a single QD (SQD) [22] used two-photon excitation of biexciton states; up-conversion luminescence of matrix bandedge based on TPA in QDs [23], SQD [24], and QDs embedded in photonic-crystal waveguide [25] used excitation above QDs bandgap but below matrix bandedge; TPA into the

sub-band used infrared excitation longer than 10μm [26], [27]. In addition, Gautham *et al.* [28] studied the time dependence and the spin-flip time between the dark and bright states of GaAs QDs by investigating the luminescence resulting from two-photon excitation near the QDs bandgap. Li *et al.* [29] reported photocurrent generated by below-bandgap two-step TPA in InAs QD solar cells. At the SQD level, TPA has been examined in InAs/GaAs SQD [22], [24], [30], as well as InGaN/GaN SQD [31]–[33]. However, direct TPA in InAs/GaAs QDs with excitation near its half-bandgap and the resulted PL has not been reported. This dissertation would fill this blank.

When QDs emit photons, the photons go in all directions without any control. One effective way to collect the photon from one direction is to put the QDs in a micro-post etched out of micro-cavity made of distributed Bragg reflectors (DBR) [34], [35]. Such a sample can be grown and fabricated using well-established techniques. A micro-post not only can make the photons to be emitted from the top of the post but also can choose the emission wavelength, since only the wavelength at the cavity mode can escape from the cavity. In this way, the cavity can act as a filter to help to isolate SQD from a QD ensemble.

In this dissertation, we present a photoluminescence (PL) study of InAs/GaAs QDs with both above-bandgap one-photon (1hυ) excitation and below-bandgap two-photon (2hυ) excitation. The 2hυ excitation energy we used is near the half-bandgap of the QDs. PL by excitation in this range of InAs QDs and the mechanisms of TPA have not been reported to the best of our knowledge. The dissertation is organized as follows. Chapter 2 provides the background knowledge of this dissertation. It includes the samples we used; what happens when the sample is under laser excitation; fundamental theory of TPA; and the theory about the light cavity. Chapter 3 presents and discusses the PL results of ensemble QDs (EQDs). It includes the

excitation power dependent PL of EQDs under 1hυ excitation and 2hυ excitation; photoluminescence excitation (PLE) spectroscopy study of EQDs under 2hυ excitation. The excitation power dependent PL of wetting layer (WL) and GaAs substrate is also included for better understanding of the EQDs data. In Chapter 4, PL study of SQD is presented. It includes the SQD PL with 1hυ and 2hυ excitation, and the temperature dependent PL with 1hυ excitation. Chapter 5 examines the PL of SQD in a micro-cavity. PL study with 1hυ and 2hυ excitation is presented. The growth technique we used to get all of our samples is MBE growth. Sample characterization techniques we used including atomic force microscope (AFM), transmission electron microscope (TEM), PL and PLE. More details about these techniques and the experimental setups can be found in the Appendix.

2 Background

2.1 Sample and Growth

The sample used in this study was grown by molecular beam epitaxy (MBE). MBE is an epitaxial growth technique in which one or several atomic or molecular beams interact on the surface of a crystalline substrate, forming a new layer of crystal. Invented by J. R. Arthur [36] and A. Y. Cho [37] in the late 1960s, MBE has gone through significant development in order to achieve more precise atomic scale deposition, which enables us to explore new materials with different composition or interface as well as innovative devices with unique structures. A basic introduction of the MBE chamber can be found in Appendix A.

2.1.1 QDs Sample Description and Growth

The QDs we studied are self-assembled InAs QDs grown on GaAs under Stranski-Krastanov (SK) growth mode. SK mode is a "layer-plus-island growth" mode, in which a complete two-dimensional (2D) layer (up to several monolayers) is formed first, followed by three-dimensional (3D) island shape growth once deposition is beyond the critical thickness to release strain due to lattice mismatch. In our case, the lattice constant of InAs is about 7% larger than that of GaAs. When InAs is deposited on GaAs, first a couple of monolayers (MLs) of InAs form a 2D layer called "wetting layer" (WL). This layer is strained to the GaAs lattice. Once the deposition is beyond the critical thickness of InAs/GaAs system, which is 1.7ML, QDs start to form to release the strain. During growth, this 2D to 3D transition process can be monitored by the reflection high energy electron diffraction (RHEED) *in-situ*. 2D growth will appear a streaky pattern, whereas 3D growth will appear a spotty pattern. Figure 2.1 [38] illustrates the RHEED patterns (left panel) and their corresponding growth process (right panel) of this transition. So as soon as we observe the spotty pattern like Figure 2.1(e), we know that InAs QDs are formed.

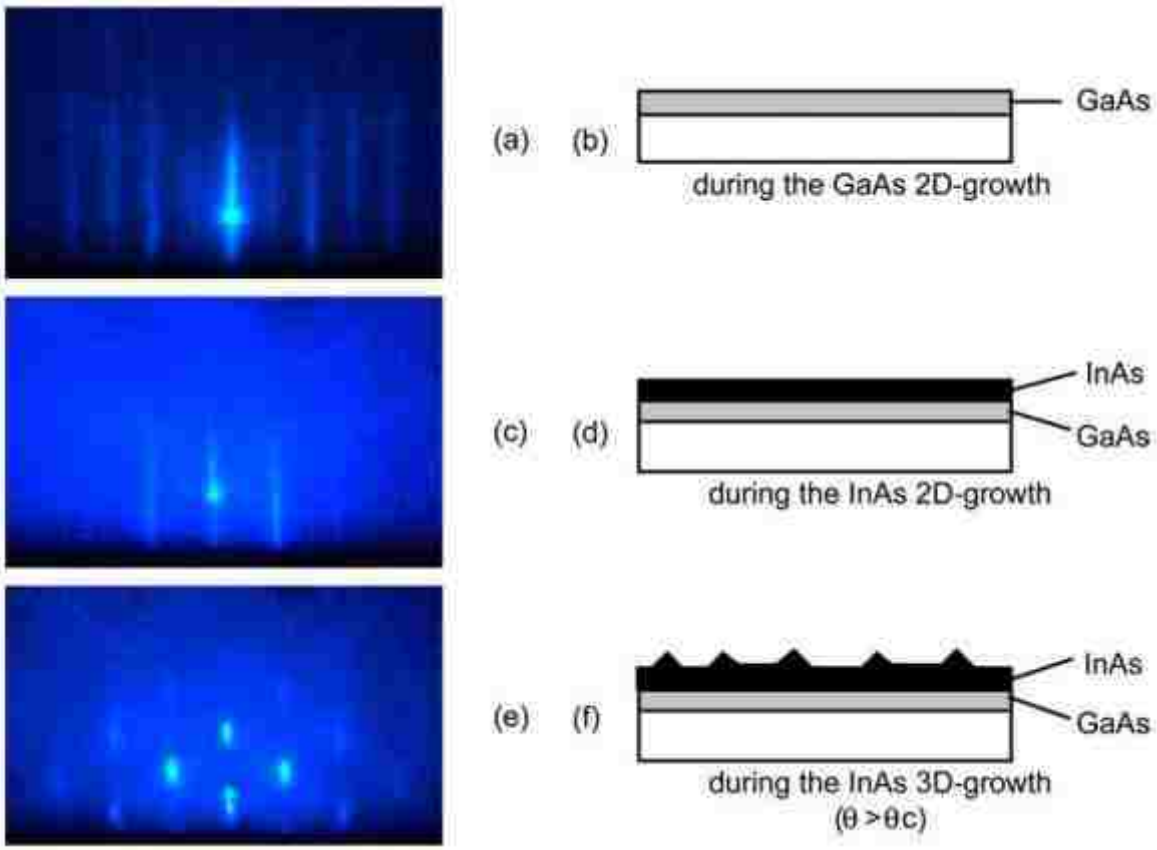

Figure 2.1. RHEED patterns (left panel) and their corresponding growth process (right panel) [38] .

Usually, people want to grow uniform size QDs on one sample for large device purpose. But for our optical setup and study, we want to have a gradient density and size distribution of QDs on one sample. There are two main advantages about such a sample. Firstly, it gives us the option to choose the PL main peak position we want because bigger QDs have a lower PL energy whereas smaller QDs have a higher PL energy due to quantum confinement. In our case, we want the QDs emits below 1μm to get good detection efficiency with our silicon charge-coupled device (Si-CCD). Secondly, such a gradient density sample enables us to locate an area with QDs or without QDs (WL only) on our Micro-PL setup which has a motor controlled stage. Plus, it will be easier to locate and separate an SQD in the low-density area.

To achieve such a gradient density QDs sample, one straightforward way is to create a gradient InAs deposition on the sample during the QDs growth. Consequently, area where InAs deposition is above the critical thickness will form QDs, whereas area where InAs deposition is below the critical thickness will only form WL. This can be realized by tilting the manipulator away from its optimal epitaxy position so that an indium flux gradient is created on the surface of the substrate.

To catch the recipe of such a gradient density QDs sample, we went through a process containing ten samples as summarized in Table 2.1. The sample number is based on the MBE chamber growth log. Since there are samples grown by the same chamber for other projects, the sample number shows discontinuity. The results column briefly shows the quality of the sample. All samples were characterized by atomic force microscope (AFM) first and some of them were further characterized by PL. Detailed AFM and PL characterization of SF046, SF077, and SF094 (indicating by *) will be shown and discussed in this dissertation. The setup of AFM and PL is introduced in Appendix B and D respectively.

All samples were grown on GaAs (100) semi-insulating (S.I.) substrate. After being transferred into the growth chamber, the substrate goes through oxide desorption first at around 585°C for 10 minutes. Then a 500nm thick high-quality GaAs buffer was grown at 580°C to make an atomic flat surface. Different recipes were then implemented for InAs QDs growth, followed by a 40s annealing. The QDs were normally covered with a GaAs cap layer for better PL signal [39]. Then another layer of InAs QDs was grown with the same recipe as the previous layer for morphology characterization.

Table 2.1. QDs samples grown for this dissertation.

Sample Number	Recipe	Result
SF026	1.7ML InAs at 0.075ML/s, 520°C; no tilt.	Elongated islands with tiny QDs clusters due to indium shutter failure.
SF027	1.7ML InAs at 0.075ML/s by MEE, 520°C; no tilt.	QDs are not uniform in size or distribution.
SF037	2.0ML InAs at 0.075ML/s, 510°C; tilt 10°.	No QDs, elongated islands.
SF038	2.0ML InAs at 0.075ML/s, 520°C; tilt 20°.	No QDs, elongated islands.
SF044	2.0ML InAs at 0.075ML/s, 510°C; no tilt.	High density QDs, not uniform size.
*SF046	2.0ML InAs at 0.075ML/s, 510°C; tilt 5°.	Big QDs; PL center > 1μm.
SF054	1.8ML InAs at 0.043ML/s, 510°C; no tilt.	High density big QDs
*SF077	1.8ML InAs at 0.022ML/s, 510°C; no tilt.	Big uniform QDs deduced from PL result; PL center > 1μm.
SF092	1.7ML InAs at 0.022ML/s, 480°C; no tilt.	Bi-size distribution QDs; PL center >1μm.
*SF094	1.7ML InAs at 0.022ML/s, 460°C; tilt 5°.	Gradient QDs density and size; low QDs density region PL center < 1μm.

As can be seen from Table 2.1, the deposition rate was decreased from 0.075ML/s to 0.022ML/s to achieve low-density QDs [40]–[42]. But low growth rate leads to the increase in QDs' size. Therefore, the growth temperature for QDs was decreased from 520°C to 460°C for smaller QDs sizes [43]. Meanwhile, the deposition amount was also reduced for the same goal. Manipulator with 10° and 20° tilt down from its optimal epitaxy position resulted in no QD formed so we reduced the tilt angle to 5° to create a proper indium flux gradient. We attempted migration-enhanced epitaxy (MEE) on sample SF027, shooting for lower density and more uniformity [44]. But the result was not ideal and we decided to go with SK growth mode for the rest of the samples.

2.1.2 QDs-in-cavity Sample Design and Growth

This sample is for the study of 2hυ absorption of the QDs inside of a cavity. This structure is also a very good candidate for the reflective type optical limiter [45]. When the radiance is below the threshold, it transmits through the cavity mode since the 2hυ absorption effect is negligible. When the radiance is high, the 2hυ absorption kicks in and the cavity mode is destroyed, turning the structure into a mirror for the incident light. And whole structure become reflective.

Figure 2.2 shows the structure diagram of the QDs-in-cavity sample. Same as the QDs sample listed in the previous section, all QDs-in-cavity samples were grown on GaAs (100) S.I. substrate. After the oxide desorption process, a 420nm GaAs buffer is grown at 580°C first. Then a superlattice consisting of 15 repetitions of 1nm GaAs/AlAs layer was grown as a dislocation filter [46], followed by another 25nm GaAs buffer layer. Then 25 repetitions of quarter-wavelength (λ/4) thick GaAs/AlAs layers are grown as the bottom DBR. The cavity is a one-wavelength thick GaAs region, in the middle of which one layer of QDs is grown. Finally, 11 repetitions of quarter-wavelength thick GaAs/AlAs layers are grown as the top DBR. The design and operation theory of such a structure will be discussed in Section 2.5.

Three samples were grown to test out the QDs-in-cavity sample. Table 2.2 briefly discusses their structure and result. Some TEM, PL, and reflectance results of SF078 and SF096 (indicated by *) will be shown in this dissertation.

Figure 2.2. Structure diagram of a QDs-in-cavity sample.

Table 2.2. Description and result for the cavity samples.

Sample Number	Description	Result
SF023	Bottom DBR & half cavity designed for 1μm	Multi-layers are uniform in most of the area.
*SF078	Micro-cavity designed for 1μm with one layer of SF077 QDs in the middle	Cavity mode > 1μm
*SF096	Micro-cavity designed for 1μm with one layer of SF094 QDs in the middle	Cavity mode < 1μm

2.2 Energy Structure of Quantum Dots and Carrier Relaxation Process

Sometimes referred to as artificial atoms, QDs have discrete energy levels similar to atoms. Figure 2.3(a) shows the energy diagram of an InAs QD embedded in GaAs matrix. The QD's ground state (E_0) is the lowest energy state in this system. But due to quantum confinement, it is much higher than the InAs bandgap (E_{InAs}). Depending on its size, a QD may have 0, 1 (E_1), 2 (E_1 and E_2) or more excited states above its ground state. The 2D WL has the second highest energy (E_{WL}) after GaAs bandgap since its thickness is only about 1nm.

The energy levels of QD dependent on its size and can be characterized by PL or capacitance measurement. As an example, the PL spectrum of sample SF077 at 10K is shown in Figure 2.3(b). From the low energy side, we can observe the QDs' ground state and up to the 4th excited states (labeled E_0 to E_4 in the figure) successively. Then above 1.4eV, there is E_{WL} at 1.452eV and E_{GaAs} at 1.515eV.

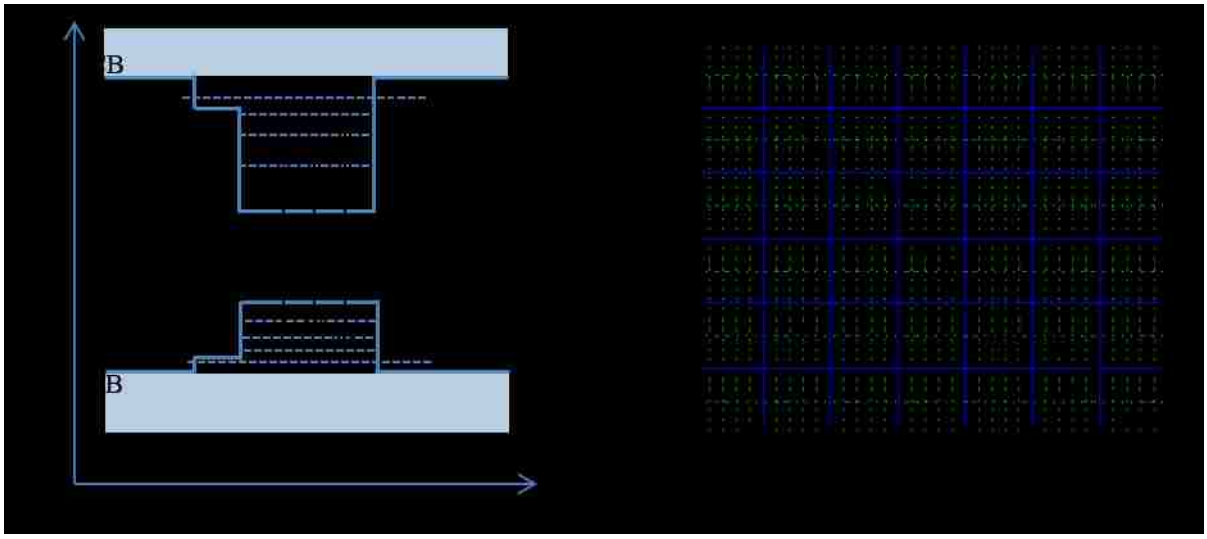

Figure 2.3. (a) Schematic of the energy levels of an InAs/GaAs QD system. (b) Photoluminescence spectrum of SF077, showing features of four excited states, WL state and the GaAs bandgap.

A perturbed system tends to return to its equilibrium in nature. Therefore photo-excited carriers in a QDs system would relax to lower energy levels after they are pumped from their original state. Investigation of this relaxation process not only reveals the underlying physics but also helps to control the carriers, e.g. keep carriers in coherence or stay in certain state. Below we will discuss the process in a non-resonant excitation case where carriers are generated in the barrier. The resonant excitation case follows the same relaxation process once carriers are captured into the QDs. Previous studies also show that electron and hole are being captured separately into QDs and relax separately in the QDs [47], [48]. We will discuss the process of electrons below and the same mechanisms can be applied for holes.

With non-resonant excitation, electrons are initially excited from the valence band (VB) into the conduction band (CB) of the barrier. Very rapidly [49], [50], the electrons are captured into the excited states of QDs through WL state by scattering and diffusion. There are two main relaxation mechanisms within a QD: phonon-assist relaxation and Auger process. In phonon-assist relaxation, although there is no intermediate state in the QD for emission of a single optical or acoustic phonon, it is possible for a multi-phonon process of several optical and acoustic phonons [51]–[54]. These phonons can be from the GaAs barrier, the WL, the QD or defect at the interface [55]. In Auger-type relaxation, an electron at excited state relax to lower state by giving its energy to another electron in an excited state or WL state [50], [51]. At low excitation power, phonon-assist relaxation dominates while Auger process is more efficient at high excitation power since it depends on the carrier density.

2.3 Rate Equation Model for Excitation Power Dependent PL

Based on the energy structure of QD and the carrier relaxation process discussed in the previous section, we develop a rate equation model for the carriers in a QD system to get the relationship between the excitation power and the PL intensity. This helps us to understand the excitation power dependent PL data with 1hυ

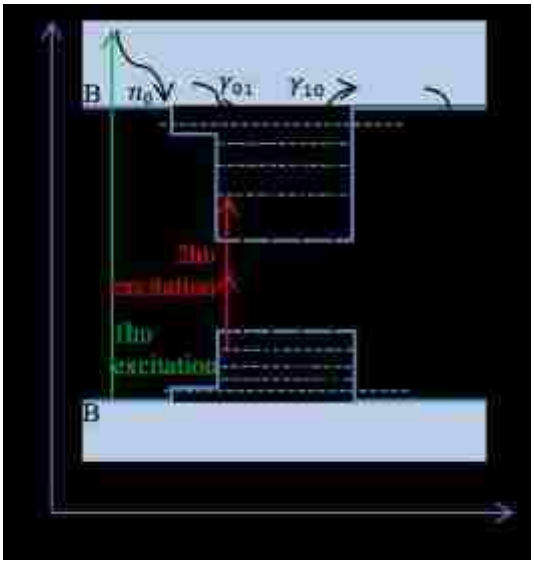

Figure 2.4. Energy diagram of a QD system. Radiative transitions are indicated by straight arrows while non-radiative transitions are indicated by curved arrows.

excitation and to predict the result with 2hυ excitation. We will describe the model with 1hυ excitation case below.

In this model, we consider the electron densities in GaAs bandedge (n_0), WL (n_1), QD second excited state (n_2), QD first excited state (n_3) and QD ground state (n_4). We include two excited states of QD in this model because the PL study of the QDs sample (SF094) used for power dependent PL shows potential of having two excited states. In fact, in the model we will see that the number of excited states does not change the excitation power and PL intensity relation. The energy diagram of such a QD system and the transitions we considered in this model is presented in Figure 2.4. The process considered in this model, presented by their transition rates, including: electron capture by WL from GaAs barrier (γ_{01}), electron capture by QDs excited states from WL (γ_{12}), cascade relaxation in the QD (γ_{23}, γ_{34}); electron thermal escape from WL to matrix (γ_{10}), from QDs to WL (γ_{21}), and from a lower level to a upper level inside of a QD (γ_{32}, γ_{43}); electron-hole radiatively recombination (γ_i^r, $i = 0,1,2,3,4$) and non-radiatively recombination ($\gamma_i^{nr}, i = 0,1,2,3,4$) from each level. In the model, we will consider low excitation power at which the photo-generated carriers are not saturated in the QDs. With 1hυ excitation, carriers are generated in the GaAs barrier with a rate gI, where g is the generation coefficient and I is the excitation power. The rate equations for the electron density at each level can then be written as:

GaAs: $$\frac{dn_0}{dt} = gI + n_1\gamma_{10} - n_0\gamma_{01} - n_0\gamma_0^r - n_0\gamma_0^{nr}. \quad (2.1)$$

WL: $$\frac{dn_1}{dt} = n_0\gamma_{01} + n_2\gamma_{21} - n_1\gamma_{10} - n_1\gamma_{12} - n_1\gamma_1^r - n_1\gamma_1^{nr}. \quad (2.2)$$

QD 2nd excited state: $$\frac{dn_2}{dt} = n_1\gamma_{12} + n_3\gamma_{32} - n_2\gamma_{21} - n_2\gamma_2^r - n_2\gamma_2^{nr}. \quad (2.3)$$

QD 1st excited state: $$\frac{dn_3}{dt} = n_2\gamma_{23} + n_4\gamma_{43} - n_3\gamma_{32} - n_3\gamma_3^r - n_3\gamma_3^{nr}. \quad (2.4)$$

QD ground state: $$\frac{dn_4}{dt} = n_3\gamma_{34} - n_4\gamma_{43} - n_4\gamma_4^r - n_4\gamma_4^{nr}. \quad (2.5)$$

Three assumptions are made to eliminate variables in the above equations. Firstly, at our experimental temperature 77K, thermal energy $k_BT \approx 6.64$meV which is an order of magnitude less than the energy interval between QD states (30-70meV [56], [57]), as well as the interval between WL and GaAs bandgap. Therefore, we expect the thermal escape $n_i\gamma_{i(i-1)}$ $(i = 1,2,3,4)$ to be negligible. Secondly, at low excitation power, we don't observe PL from WL level or GaAs bandgap. So we can assume that carriers has a much higher rate to be captured by the QDs than radiatively recombine in GaAs barrier or WL, namely $n_0\gamma_{01} \gg n_0\gamma_0^r$, $n_1\gamma_{12} \gg n_1\gamma_1^r$. Thirdly, non-radiative recombination in QDs and WL has mainly two channels, the first one is through Auger recombination, and the second one is through nearby defect levels. Auger recombination is extrapolated to be long-lived (ns to μs range) [58], and defect is suppressed by crystalline around the QDs. Therefore γ_i^{nr} $(i = 1,2,3,4)$ is insignificant. With these assumptions and under steady states condition, we can derive from the above equations:

Eq. (2.1) => $$gI \approx n_0\gamma_{01} + n_0\gamma_0^{nr} \Longrightarrow n_0 \approx \frac{gI}{\gamma_{01} + \gamma_0^{nr}} \sim I. \quad (2.6)$$

Eq. (2.2) => $$n_0\gamma_{01} \approx n_1\gamma_{12} \Longrightarrow n_1 \approx n_0\frac{\gamma_{01}}{\gamma_{12}} \sim I. \quad (2.7)$$

Eq. (2.3) => $$n_1\gamma_{12} \approx n_2\gamma_{23} \Longrightarrow n_2 \approx n_1\frac{\gamma_{12}}{\gamma_{23}} \sim I. \quad (2.8)$$

Eq. (2.4) => $$n_2\gamma_{23} \approx n_3\gamma_{34} \Longrightarrow n_3 \approx n_2\frac{\gamma_{23}}{\gamma_{34}} \sim I. \quad (2.9)$$

Eq. (2.5) => $$n_3\gamma_{34} \approx n_4\gamma_4^r \Longrightarrow n_4 \approx n_3\frac{\gamma_{34}}{\gamma_4^r} \sim I. \quad (2.10)$$

We can see that the electron density in each level is proportional to the excitation power. The relationship between the hole density p_i ($i = 0,1,2,3,4$) and the excitation power can be derived similarly. And they are proportional to the excitation power too.

Then let's consider the relationship between PL intensity and the excitation power. PL intensity of each level i ($i = 0,1,2,3,4$) can be written as:

$$PL_i \sim F_i n_i p_i + E_i n_i \sim F_i n_i^2 + E_i n_i \sim F_i I^2 + E_i I. \quad (2.11)$$

Here we treat $p_i \sim n_i$ since they have the same I dependence. $F_i n_i p_i$ is free carrier (or un-correlated electron and hole) recombination with a coefficient F_i, and $E_i n_i$ is exciton (or correlated electron and hole) recombination [47], [59], [60] with a coefficient E_i. Hence, if free carrier dominates in the recombination process, PL intensity will have a square relationship with the excitation power; if exciton recombination dominates, PL intensity will have a linear relationship with the excitation power. The exciton Bohr radius of bulk InAs is about 34nm [61], much bigger than our QDs height and comparable with the QDs radius. Thus carriers are strongly confined in the QDs, which make them much easier to form exciton. So in QDs, exciton recombination dominates and PL intensity is proportional to the excitation power. In GaAs barrier, there is no quantum confinement, thus free carrier recombination dominates, giving a quadratically-increased PL intensity with the excitation power. In WL, there is one-dimensional quantum confinement, but the confinement is not as strong as it is in QDs. Carriers in WL can still interact with carriers in the GaAs matrix. Therefore, we expect the PL-excitation power relation to be between linear and quadratic. In summary, we can write: $PL_{QDs} \sim I$, $PL_{GaAs} \sim I^2$, and $PL_{WL} \sim I^s$, where $1 < s < 2$.

2.4 Two-photon Absorption

In our 2hυ excited PL measurement, the relaxation and recombination process after carriers are created is the same as 1hυ excitation. The difference lies in the absorption part. There are mainly three types of TPA: direct TPA, indirect (two-step) TPA, and Auger-type process. Figure 2.5 shows the diagrams of these three mechanisms and we will explain them in the frame of our energy system. Direct TPA means an electron is pumped from valence band (VB) to conduction band (CB) by absorbing two photons simultaneously. Direct TPA is a one-step process and there is no real intermediate band (IB) required in this process. Indirect TPA and Auger-type process are two-step processes, and real IBs are required for these two types. Indirect TPA means an electron is pumped from VB to IB by absorbing one photon in the first step. In the second step, this electron absorbs another photon and gets pumped to CB from IB before it relaxes or recombines. In Auger-type process, two electrons are pumped from VB to IB by absorbing two photons in the first step. In the second step, one electron relaxes to VB and gives out energy, which is absorbed by the other electron and this electron gets pumped from IB to CB. In reality, the transition rate of direct TPA is much lower compared with the other two processes. Thus, the direct TPA is usually not considered unless the excitation power is high (e.g. pulse laser excitation). Indirect TPA and Auger-type process can coexist. If the carrier has a long lifetime at the intermediate level, it is likely that indirect TPA will dominate. But if the carrier recombines fast from the intermediate level, then the Auger process is more likely to dominate. For all these three TPA mechanisms, the carrier density has a quadratic dependence on the excitation power.

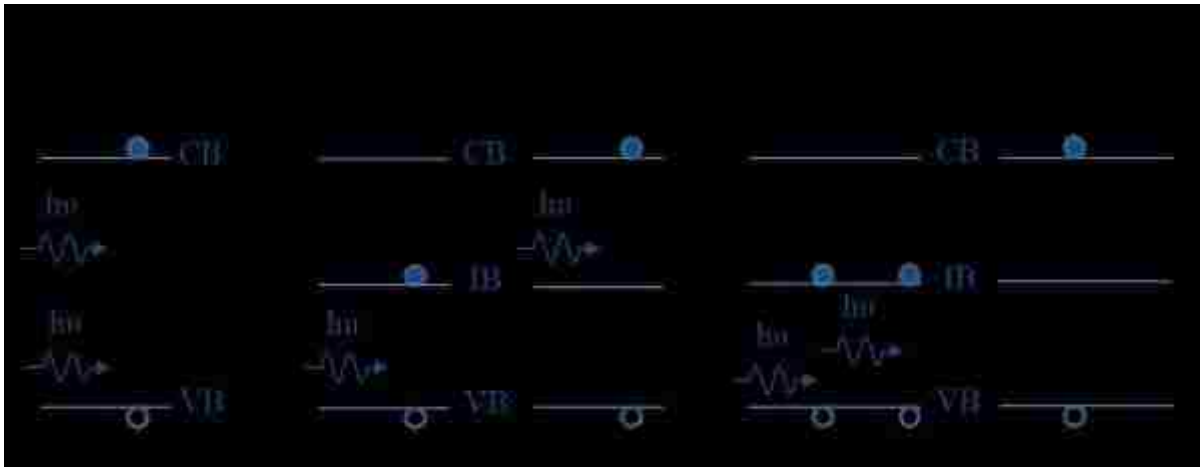

Figure 2.5. Diagrams of three types of TPA: (a) direct TPA; (b) indirect TPA; (c) Auger-type process.

Mathematically, TPA can be described by quantum mechanics and the rate at which TPA processes occur can be calculated by solving the time-dependent Schrödinger equation through second-order perturbation theory. Below we rehash the derivation of TPA processes for an atomic system in reference [62].

Assume that the atomic wave-function $\psi(\mathbf{r},t)$ obeys the time-dependent Schrödinger equation

$$i\hbar\frac{\partial\psi(\mathbf{r},t)}{\partial t} = \hat{H}\psi(\mathbf{r},t) = \left(\hat{H}_0 + \hat{V}(t)\right)\psi(\mathbf{r},t), \tag{2.12}$$

where $\hat{H}_0$ is the Hamiltonian for a free atom and $\hat{V}(t)$ is the interaction between the atom and the applied laser field presented by the form $\vec{E}(t) = Ee^{-i\omega t} + E^* e^{i\omega t}$. $\hat{V}(t)$ is represented as

$$\hat{V}(t) = -\hat{\mu}\vec{E}(t), \qquad \text{where } \hat{\mu} = -e\hat{r}\,. \tag{2.13}$$

Assume that the solutions to Schrödinger equation for a free atom are in the form

$$\psi_n(\mathbf{r},t) = u_n(\mathbf{r})e^{-i\omega_n t}\,, \tag{2.14}$$

where $\omega_n = E_n/\hbar$ is associated with the eigenstates, and n refers the various eigenstate. And the spatially varying part of the wavefunction $u_n(\mathbf{r})$ satisfies eigenvalue equation

$$\hat{H}_0 u_n(\mathbf{r}) = E_n u_n(\mathbf{r}) \,. \tag{2.15}$$

The solutions are chosen so that they constitute a complete, orthonormal set, satisfying

$$\int u_m^* u_l d^3r = \delta_{ml} \,. \tag{2.16}$$

The solution for Eq. (2.12) can then be expressed as a linear combination of these eigenstates as

$$\psi(\mathbf{r}, t) = \sum_l a_l(t) u_l(t) e^{-i\omega_l t} \,. \tag{2.17}$$

Substitute the above equation into Eq. (2.12) and apply the orthonormal condition (Eq. (2.16)), we obtain

$$i\hbar \frac{da_m}{dt} = \sum_l a_l(t) V_{ml} e^{-i\omega_{lm} t} \,, \tag{2.18}$$

where

$$V_{ml} \equiv \langle u_m | \hat{V} | u_l \rangle = \int u_m^* \, \hat{V} u_l d^3r \tag{2.19}$$

is the matrix elements of the interaction Hamiltonian $\hat{V}$, and $\omega_{lm} = \omega_l - \omega_m$.

Now we use perturbation techniques to solve Eq. (2.18) by introducing an expansion parameter η, which varies between 0 and 1 and $\eta = 1$ corresponds to our physical situation. We replace V_{ml} by ηV_{ml}, and expand $a_m(t)$ in powers of the interaction as

$$a_m(t) = a_m^{(0)}(t) + \eta a_m^{(1)}(t) + \eta^2 a_m^{(2)}(t) + \cdots \,. \tag{2.20}$$

Then we equal the powers of η on each side of Eq. (2.18) to get

$$i\hbar \frac{da_m^{(N)}(t)}{dt} = \sum_l a_l^{(N-1)} V_{ml} e^{-i\omega_{lm} t} \,, \qquad N = 1,2,3, \ldots \,. \tag{2.21}$$

$N = 1$ corresponds to first-order interaction, meaning linear absorption. And $N = 2$ corresponds to TPA. We assume that the atom is in the ground state g when there is no applied laser field so that

$$a_g^{(0)}(t) = 1, \;\; a_l^{(0)}(t) = 0 \;\text{ for } l \neq g \,. \tag{2.22}$$

With Eq. (2.13) and Eq. (2.19), we can present V_{mg} as

$$V_{mg} = \; -\mu_{mg}\left(E e^{-i\omega t} + E^* e^{i\omega t}\right). \tag{2.23}$$

Substitute Eq. (2.22) and Eq. (2.23) into Eq. (2.21) and integrate, we get

$$a_m^{(1)}(t) = \frac{\mu_{mg} E}{\hbar(\omega_{mg} - \omega)}\left[e^{i(\omega_{mg}-\omega)t} - 1\right] + \frac{\mu_{mg} E^*}{\hbar(\omega_{mg} + \omega)}\left[e^{i(\omega_{mg}+\omega)t} - 1\right]. \tag{2.24}$$

This is the probability amplitude of the first-order interaction. The first term can become resonant for linear absorption, where the energy difference between the ground state (g) and the excited state (m) equals to the applied photon energy. The second term can become resonant for simulated emission, if the state m is below state g. We will drop the second term when we only consider linear absorption.

Similarly, for $N = 2$ we can get

$$a_f^{(2)}(t) = \sum_m \frac{\mu_{fm}\mu_{mg} E^2}{\hbar^2(\omega_{mg} - \omega)}\left[\frac{e^{i(\omega_{mg}-2\omega)t} - 1}{\omega_{fg} - 2\omega}\right], \tag{2.25}$$

where state *f* is the final state and state *m* is the intermediate state. So the probability for the atom to be in state *f* is

$$p_f^{(2)}(t) = \left|a_f^{(2)}(t)\right|^2 = \left|\sum_m \frac{\mu_{fm}\mu_{mg} E^2}{\hbar^2\left(\omega_{mg} - \omega\right)}\right|^2 2\pi t \delta\left(\omega_{fg} - 2\omega\right). \tag{2.26}$$

The delta function on the right-hand side is not realistic in the physical world. In fact, the final state *f* is spread into a density of states $\rho_f(\omega_{fg})$, defined such that $\rho_f(\omega_{fg})d\omega_{fg}$ is the

probability that the transition frequency lies between ω_{fg} and $\omega_{fg} + d\omega_{fg}$. And the density of states is normalized such that

$$\int_0^\infty \rho_f(\omega_{fg}) d\omega_{fg} = 1. \tag{2.27}$$

Then the probability for the atom to be in state *f* must be averaged over all possible transition frequency as

$$\begin{aligned} p_f^{(2)}(t) &= \left| \sum_m \frac{\mu_{fm}\mu_{mg}E^2}{\hbar^2(\omega_{mg} - \omega)} \right|^2 t \int_0^\infty \rho_f(\omega_{fg}) 2\pi\delta(\omega_{fg} - 2\omega) d\omega_{fg} \\ &= \left| \sum_m \frac{\mu_{fm}\mu_{mg}E^2}{\hbar^2(\omega_{mg} - \omega)} \right|^2 2\pi t \rho_f(\omega_{fg} = 2\omega). \end{aligned} \tag{2.28}$$

Define transition rate as

$$R = \frac{p(t)}{t}. \tag{2.29}$$

Then the transition rate for TPA is

$$R_{fg}^{(2)} = \left| \sum_m \frac{\mu_{fm}\mu_{mg}E^2}{\hbar^2(\omega_{mg} - \omega)} \right|^2 2\pi \rho_f(\omega_{fg} = 2\omega). \tag{2.30}$$

There are a couple of things that we can tell from Eq. (2.30). Firstly, the TPA rate is a function of $|E|^4$, meaning square of the laser field intensity. Secondly, when the intermediate state transition frequency resonates with the laser field frequency ($\omega_{mg} \approx \omega$), $R_{fg}^{(2)}$ becomes significant. This is the case for indirect TPA. For direct TPA, there is no real intermediate state, we can imagine the "virtual intermediate state" to be any state exists in the system. This results in a big frequency difference (($\omega_{mg} - \omega$) is big), thus small TPA rate.

2.5 Distributed Bragg Reflector and Cavity Mode

In Section 2.1.2, we introduce our QDs-in-cavity sample. In this section, we will discuss the theory behind it. Two mirrors can form a Fabry-Perot cavity and only the cavity mode can be transmitted out of the cavity. In semiconductor micro-cavity, two sets of distributed Bragg reflector (DBR) play the role of the mirrors. One pair of DBR consists of an alternating sequence of high and low refractive index layers with quarter-wavelength thickness. This arrangement makes the reflection from each interface adds constructively to produce a high reflectance. The reflectance of the DBR can be calculated by matrix propagation method [63]. With 2N pairs of quarter-wavelength layers at normal incidence, reflectance can be given as [64]:

$$R = \left[\frac{1 - \frac{n_l}{n_f}\left(\frac{n_1}{n_2}\right)^{2N}}{1 + \frac{n_l}{n_f}\left(\frac{n_1}{n_2}\right)^{2N}} \right]^2, \tag{2.31}$$

where n_f and n_l are the refractive indexes of the first and last layer that the incident light interacts. Typically, the first layer would be air and the last would be substrate. n_1 and n_2 are the refractive indexes of the two different materials forming DBR. It would be easier to see the relation between R, $\frac{n_1}{n_2}$, and N if we define $a = \frac{n_l}{n_f}$ and rewrite the above expression as:

$$R = \left[\frac{1}{1 + a\left(\frac{n_1}{n_2}\right)^{2N}} - \frac{1}{1 + \frac{1}{a\left(\frac{n_1}{n_2}\right)^{2N}}} \right]^2. \tag{2.32}$$

As we can see, a larger value of $\frac{n_1}{n_2}$ or a bigger N (providing $\frac{n_1}{n_2} < 1$) would result in a higher reflectance. Therefore, choosing materials with bigger refractive index difference or increasing the number of DBR pairs could give us mirrors with higher reflectivity.

However, there are more factors need to be considered in the structural design in reality. For example, the lattice mismatch between the two material needs to be small for epitaxial growth. That's why GaAs/AlAs is the most widely used pair in semiconductor micro-cavity DBR [34], [35]. For a DBR stack designed for an incident light at 1μm, the relation between reflectance and the number of GaAs/AlAs DBR pairs is plotted in Figure 2.6(a). Insert is a zoom-in for the 10-20 pairs region. As we can see, in order to achieve reflectance above 99.5% (highly-reflective mirror for laser cavity), 20 pairs or more of DBR are required. In our QDs-in-cavity structure, 25 pairs of DBR are implemented as the bottom mirror and 11 pairs of DBR are used as the top mirror. Less number of DBR is implemented for the top mirror so that most of the light can be emitted from the top. Reflectance as a function of wavelength for a 25-pair GaAs/AlAs DBR designed for 1μm is plotted in Figure 2.6(b). A high reflectance is achieved between 960nm and 1030nm.

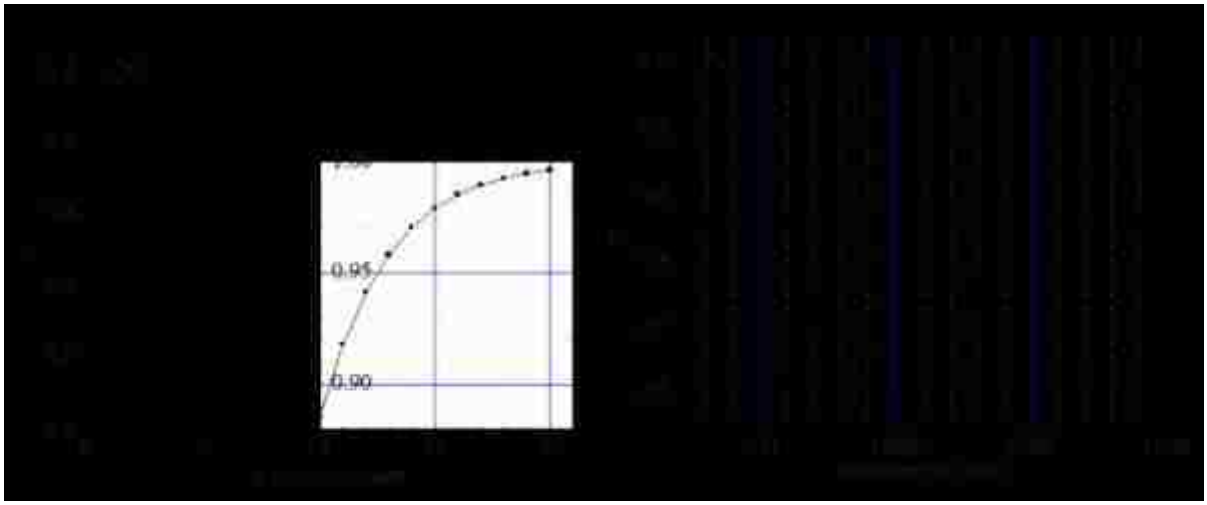

Figure 2.6. (a) Reflectance for different number of GaAs/AlAs DBR pairs. (b) Wavelength-dependent reflectance for 25 GaAs/AlAs DBR pairs designed for 1μm.

When two DBR mirrors are put together with a cavity in between, a cavity mode is created in the middle of the high reflectance band. The wavelength at this mode can be coupled out of the cavity. If we put QDs inside of the cavity, only the PL aligned with the cavity mode

can be coupled out. Thus, the cavity acts as a filter which can help us to isolate SQD. Figure 2.7(a) shows the simulation and experimental results of the reflectance of a QDs-in-cavity sample (SF078). The experimental result is normalized to its maximum value. The sharp notch at 1066nm with a width of 2.5nm on the simulation curve is the cavity mode. On the experimental curve, this notch has a width of 5.8nm, wider and shallower than simulation due to the sample quality. In Figure 2.7(b), PL of sample SF078 at RT (black) and 10K (red) is presented. We can see that the PL's position and width match with the cavity notch. At 10K, the PL shift to the short wavelength side for 17nm. This provides information about direction and amount that the cavity notch shifts when the temperature is at 10K since the instrument cannot directly measure reflectance at low temperature.

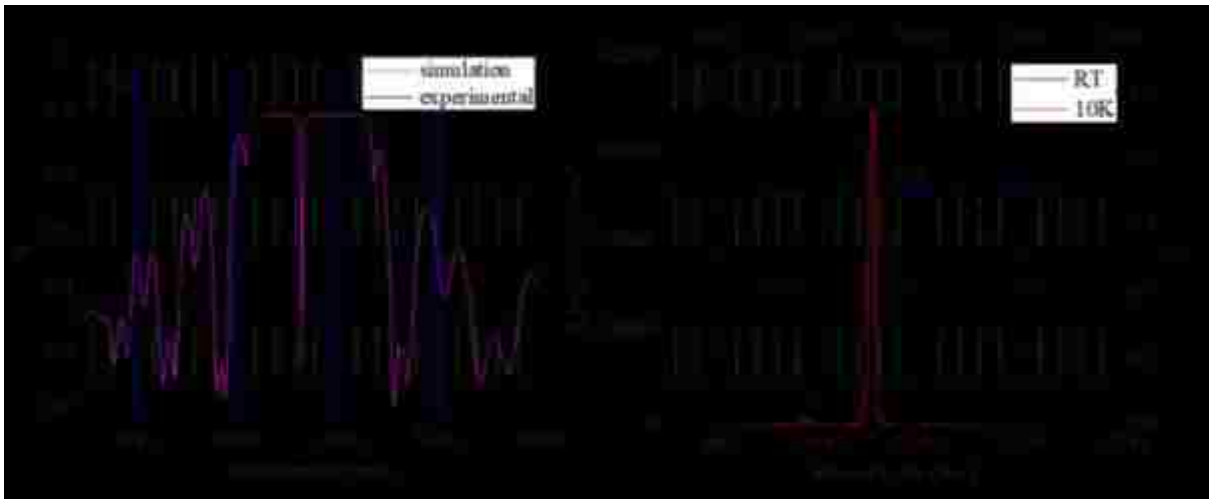

Figure 2.7. (a) Simulation (magenta) and experimental (black) results of the reflectance of sample SF078. (b) Experimental reflectance (black) of sample SF078 and photoluminescence of the same sample at RT (black) and 10K (red).

3 Photoluminescence of Ensemble Quantum Dots

3.1 Sample Morphology and PL Characterization

In this chapter, we will discuss PL behavior of ensemble InAs/GaAs QDs under 1hυ and 2hυ excitation. The EQDs sample used in this chapter is the high QDs density area of SF094. Sample SF094 is grown with 1.7ML InAs at 0.022ML/s, manipulator was tilted downwards by 5°. AFM image of this sample at five different positions along the indium flux is shown in Figure 3.1: (a) position 2 (p2), (c) position 6 (p6), (e) position 7 (p7), (g) position 8 (p8), and (i) position 5 (p5). QDs density for each position is: p2 -- 220/μm^2, p6 -- 100/μm^2, p7 -- 28/μm^2, p8 -- 8/μm^2 respectively. At p5, the indium coverage is below the critical thickness, therefore almost no QD is formed. The QDs have a lens shape in general, with a diameter 30±10nm and a height below 5nm. Since the height of QDs is much smaller than its diameter, quantum confinement effect is much stronger in the vertical direction than in lateral. Thus, the height plays a more significant role in determining the QD's energy level, which will be reflected in the QD's PL spectrum. Therefore we focus more on the distribution of QDs height other than diameter when anticipating their PL. The QDs height histogram of each position is shown to the right of their corresponding AFM image in Figure 3.1.

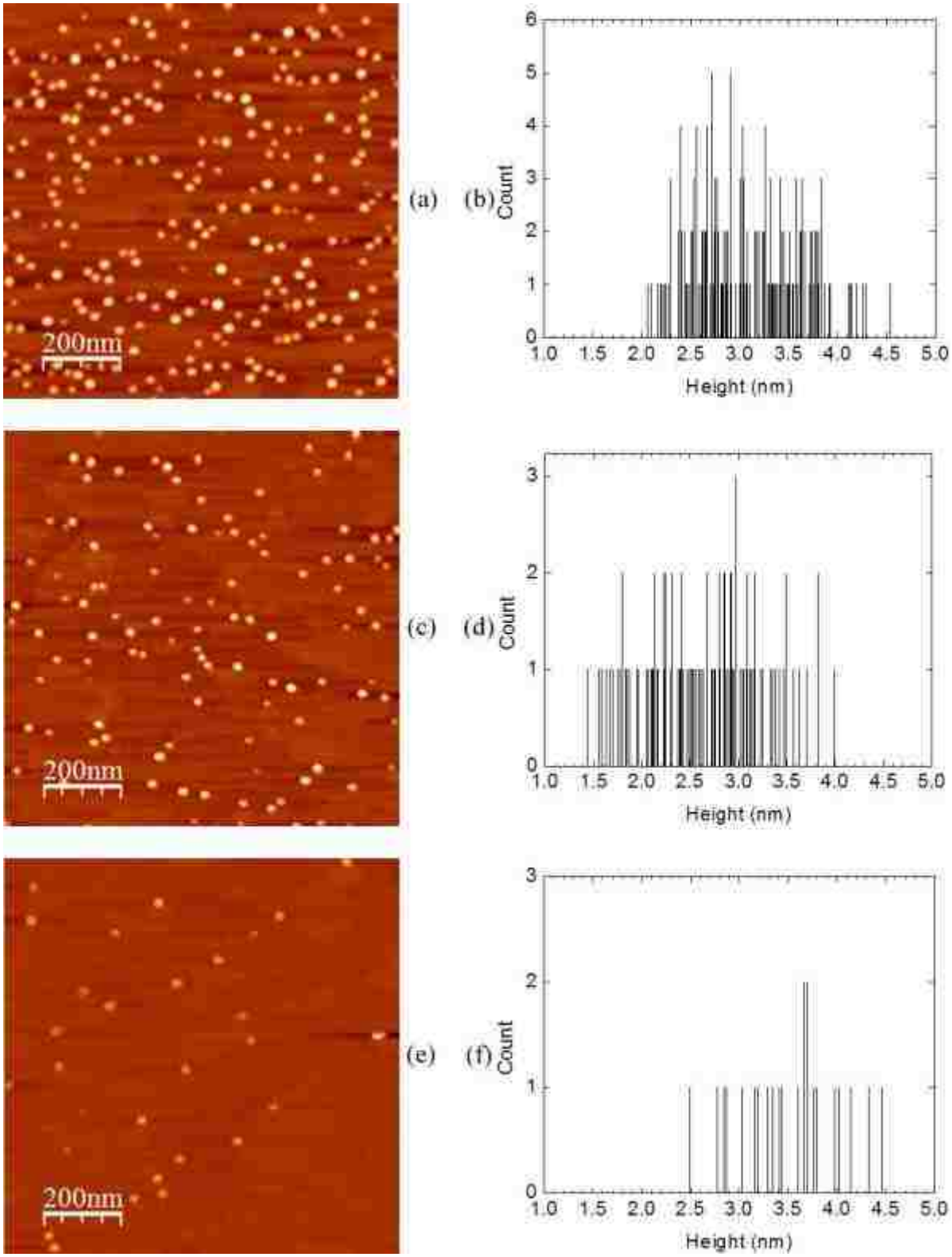

Figure 3.1. $1\times1\mu m^2$ AFM image of SF094 at different positions (left panel) and their corresponding QDs height histograms (right panel). (a) p2, (c) p6, (e) p7, (g) p8, (i) p5.

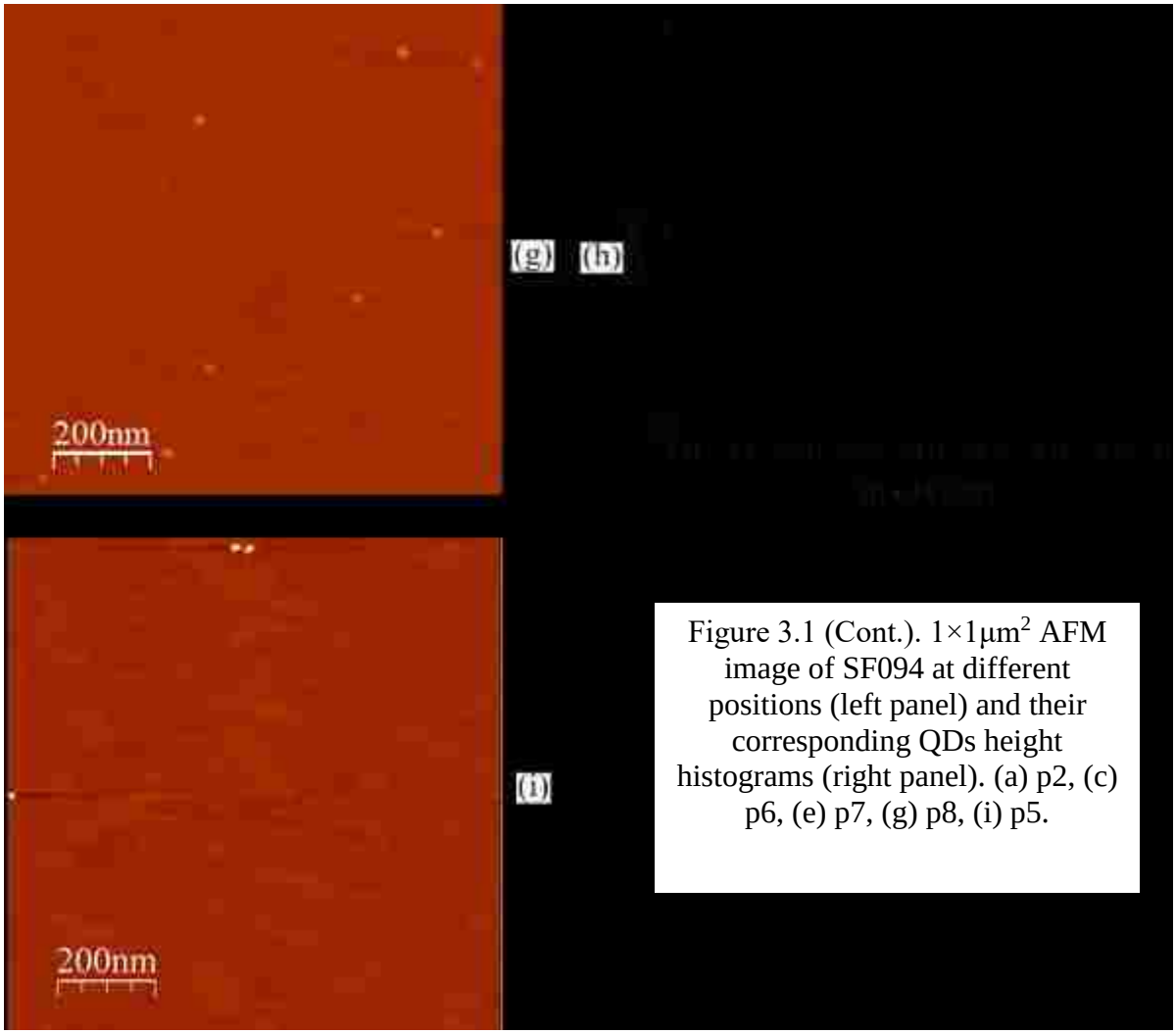

Figure 3.1 (Cont.). $1\times1\mu m^2$ AFM image of SF094 at different positions (left panel) and their corresponding QDs height histograms (right panel). (a) p2, (c) p6, (e) p7, (g) p8, (i) p5.

Photoluminescence characterization is done with an excitation source of 532nm at a power of $32mW/cm^2$ from a frequency-doubled neodymium-doped yttrium aluminum garnet (Nd: YAG) laser. The sample was kept at 10K using a closed-cycle helium optical cryostat. In Figure 3.2, PL of different locations (labeled L5-L13) along the indium flux gradient on sample SF094 is shown. At L5 and L6, only WL PL is observed. This indicates that at these locations the InAs coverage is below the InAs QDs critical thickness, therefore, no QD is formed. Starting from L7, we can see QDs emitting below 1.4eV. From L7 to L8, the QDs PL becomes much more distinguishable but still low in intensity. Meanwhile, the WL PL still presents. This

indicates that between L7 and L8 is the low QDs density region. From L5 to L8, the WL PL center shifts from 1.433eV to 1.419eV due to thickness increases and broadens from 11.5meV to 13.5meV due to increase in thickness fluctuation. After L8, QDs emission becomes strong and the WL PL intensity drops, indicating there are more QDs and carriers now have more low energy states to fill first. The QDs PL has a single broad Gaussian shape, which echoes well with our AFM observation in QDs height distribution. The QDs PL first red shifted from 1.258eV at L8 to 1.226eV at L10. This is because as the InAs coverage increase, the QDs get bigger. But as the InAs coverage keeps increasing, competition for space between QDs starts, therefore, smaller QDs are formed on L11, L12, and L13. PLs from these three locations stay around 1.241eV with a full width at half maximum (FWHM) about 77meV. This implies that the formation of QDs reaches an equilibrium and any excess indium is not consumed.

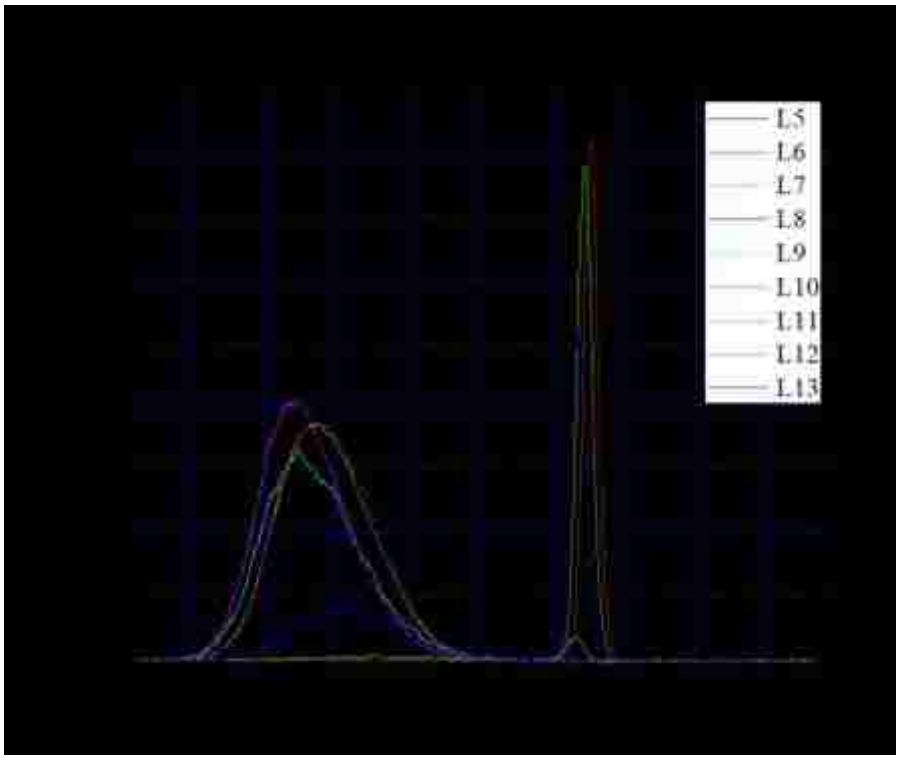

Figure 3.2. Photoluminescence spectra of sample SF094 with gradient QDs at 9 different locations (L5-L13) on sample along the indium flux gradient.

3.2 One-photon Excited Power Dependent PL of EQDs

In this section, we will show the power dependent PL study of EQDs with 1hυ excitation. The experiment was conducted with a Horiba LabRAM HR800 system equipped with a He-Ne laser, a 0.75m spectrometer, and a thermoelectrically cooled Si-CCD. The detailed apparatus can be found in Appendix D. The laser has a maximum power I_{10}~6mW. In the notation of the laser power, the first subscript "1" indicates 1hυ excitation, for 2hυ excitation it would be "2". And the second subscript "0" indicates the maximum power. The samples were cooled to 77K in a continuous flow cryostat using liquid nitrogen. The excitation power was varied by a set of neutral density optical filters. Since the excitation energy is higher than the GaAs bandgap, the light will be absorbed by the GaAs matrix and carriers (electrons and holes) will be generated in GaAs. At low excitation power, these carriers will quickly fall into the QDs ground states which have lower energy levels compare to GaAs bandedge. Then they will recombine radiatively (emitting photons) or non-radiatively (not emitting photons). As power increases, carriers would fill up the QDs ground states and start to fill their excited states. If the power keeps increasing, carriers would start to fill higher energy levels like the WL states or even the GaAs bandedge. Normalized power dependent PL of EQDs with 1hυ excitation is shown in Figure 3.3. Each spectrum is vertically shifted by 1 for clarity. At low excitation power, only the QDs PL is observed. At 1×10^{-4}% power, the PL centers around 1.238eV and has a FWHM about 60.7meV. As power increases, the QDs PL broadens and shows a blue shift. At 0.1% power, it centers around 1.252eV and the FWHM increases to 73.2meV. This implies that 1hυ excitation generated carriers have filled up the QDs ground states and start to fill the excited state. The excited states emission are not well resolved in this process, we attribute this to the large variation in the QDs size on this sample. At 1% power, WL emission at 1.431eV and GaAs

bandedge emission at 1.51eV start to show. These two peaks become more distinct at 5% and 10% power.

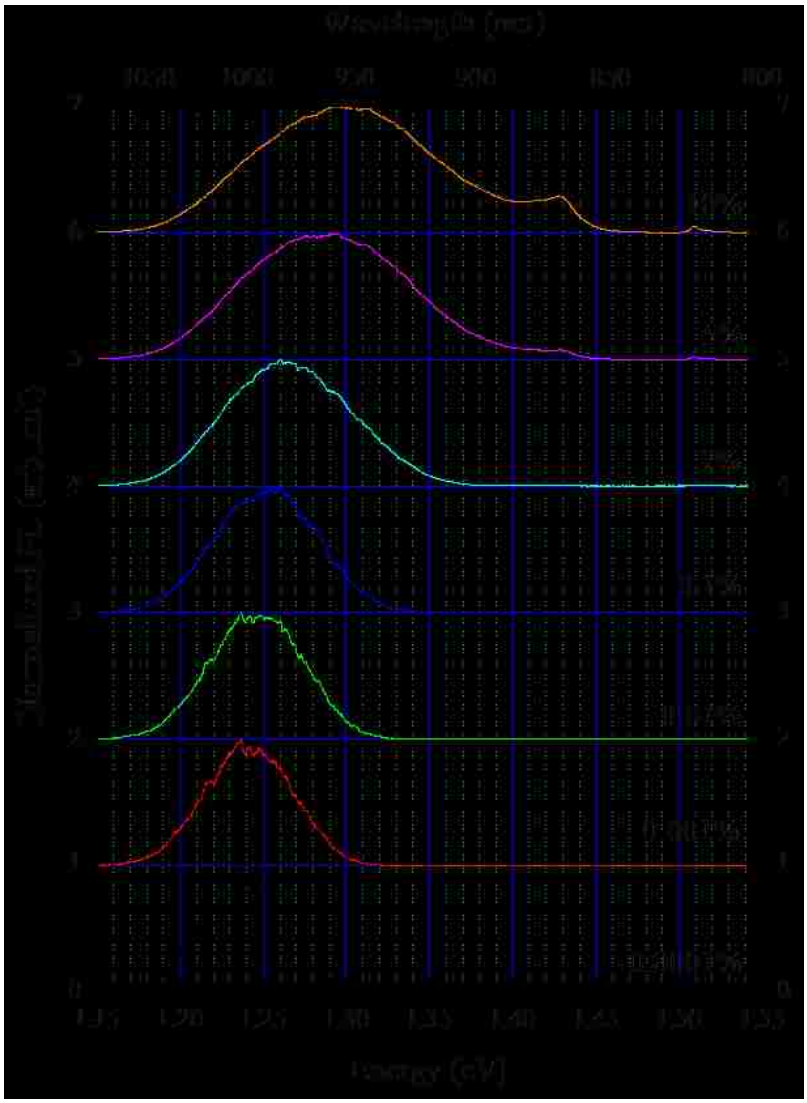

Figure 3.3 Normalized 1hυ excited PL spectra of EQDs with varying excitation power. 100% power equals to I_{10} ~ 6mW.

Then let us look at the QDs PL integrated intensity as a function of excitation power fraction (I_1/I_{10}). A representative data of the PL collected from one spot on the EQDs region is plotted in log-log scale in Figure 3.4(a). As we can see the relation can be well fitted with function $PL \sim I^s$ represented by the red straight line. When the power is below 10% of I_{10}, the slope is very close to unity. And when the power goes beyond 10% of I_{10}, the slope is less than

one due to carrier saturation in QDs. This linear relationship between excitation power and the QDs integrated intensity is explained with the equation model described in Section 2.3. We examined multiple spots and the power law indexes of them are shown in Figure 3.4(b). The unity index can be repeated quite well.

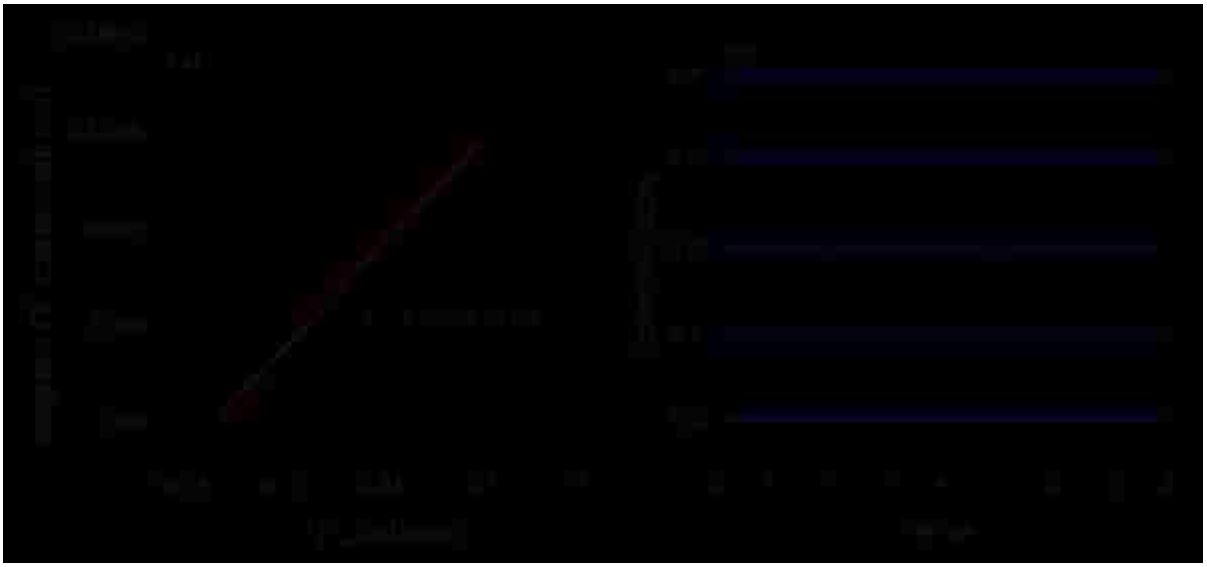

Figure 3.4. (a) Excitation power dependent integrated PL intensity of EQDs with 1hυ excitation. Red line is the power law fitting: $PL = a \cdot I^s$ with power index s = 1.07. (b) Power law indexes of multiple EQDs samples. Error bars indicate the standard error of power law fitting.

3.3 Two-photon Excited Power Dependent PL of EQDs

In this section, we will show the power dependent PL study of EQDs with 2hυ excitation. The experiment setup that we used for 2hυ excited PL is the same as 1hυ excited PL mentioned in the previous section apart from the excitation source. For 2hυ excitation, we used an external infrared 100fs linearly polarized pulse laser with 250kHz repetition rate. It is generated from an optical parametric amplifier which uses the output of another optical amplifier (seeded with another 800nm pulse laser with 80MHz repetition) as the pump light. Appropriate optical filters were put in the excitation path to make sure that there is no excitation above GaAs bandgap. The

energy range that we used for 2hυ excitation is from 0.60eV to 0.77eV, corresponding to the 2hυ energy range between QDs ground states and the GaAs bandedge. Details of this excitation source system and the 2hυ excitation laser spectra can be found in Appendix E.

Now that the photons from the excitation source have energy lower than half of the GaAs bandgap, in theory, 1hυ or even 2hυ has a very low probability to be absorbed by the GaAs. However, 2hυ energy is higher than the QDs ground states, so there is the possibility that electrons in QDs can absorb two photons at the same time and get excited from VB to CB of the QDs. Then followed by the relaxation process, we would observe PL from QDs. If this happens, we would expect the PL intensity of QDs to have a square relationship with the excitation power. Because now the electron density and excitation power relationship can be derived as:

$$\frac{dn_2}{dt} = g'I \cdot g'I - n_2\gamma_2^r - n_2\gamma_2^{nr} - n_2\gamma_{21} \Longrightarrow n_2 \sim I^2. \quad (3.1)$$

With 2hυ, excitons are created in the QD itself. Therefore, during recombination process, exciton recombination dominates again and PL intensity will be linear with electron density, which has a square relationship with the excitation power.

We performed excitation power dependent PL measurement at various excitation energies. The excitation power dependent evolution of PL spectra with these excitations are very similar. Here we only present the PL spectra of EQDs with 0.622eV excitation in Figure 3.5. The spectra are normalized to the maximum of QDs peak. At low power, we observed only QDs PL. It centers at 1.245eV and has a FWHM of 67meV. Very close to the QDs PL with 1hυ excitation at 0.06μW (0.001% in Figure 3.3). As power increases, WL PL and GaAs bandgap emission start to arise even when the 2hυ excitation energies are below the WL or GaAs bandgap.

The WL PL and GaAs bandedge emission are unexpected since the excitation is only half of the QDs ground state energy. We suspected that the WL and barrier PL were from up-

conversion via QDs states. Up-conversion in InAs QDs and SQD with continuous wave laser was previously reported by Paskov *et al.* [23] and Kammerer *et al.* [24]. Paskov *et al.* observed barrier PL when the excitation energy is resonant with the QDs excited states or the WL states. This up-converted PL disappeared when the excitation went below the QDs ground states energy. The authors attribute this up-conversion to two-step TPA through the QDs state. Kammerer *et al.* observed up-converted SQD and WL PL when the excitation energy is below their transition energies. They attribute this to two-step TPA through a band tail of WL formed by the WL roughness. In order to confirm our suspicion that the WL and barrier PL are from up-conversion via QDs states, we performed 2hυ excitation on another two samples: one is the area where there is only WL (no QD is formed) of SF094, the other is a S.I. GaAs substrate (the same material we grew all our samples on). It can help us to investigate the role of QDs by comparing the PL behavior of QDs area and WL area. The role of WL would be revealed by comparing the PL behavior of WL area and the GaAs substrate. Results of these two samples are discussed in the next section.

QDs PL integrated intensity in Figure 3.5 as a function of excitation power fraction (I_2/I_{20}) is presented in Figure 3.6(a). The relation can again be fitted with $PL \sim I^s$, and the s value is 2.19. The slopes are close to 2 as we expected for TPA in QDs. The power law indexes with other 2hυ excitation energies are shown in Figure 3.6(b). Energy between 1.2eV to 1.3eV corresponds to the QDs ground transition, and 1.43eV corresponds to WL transition. As we can see the index is close to 2 for both cases.

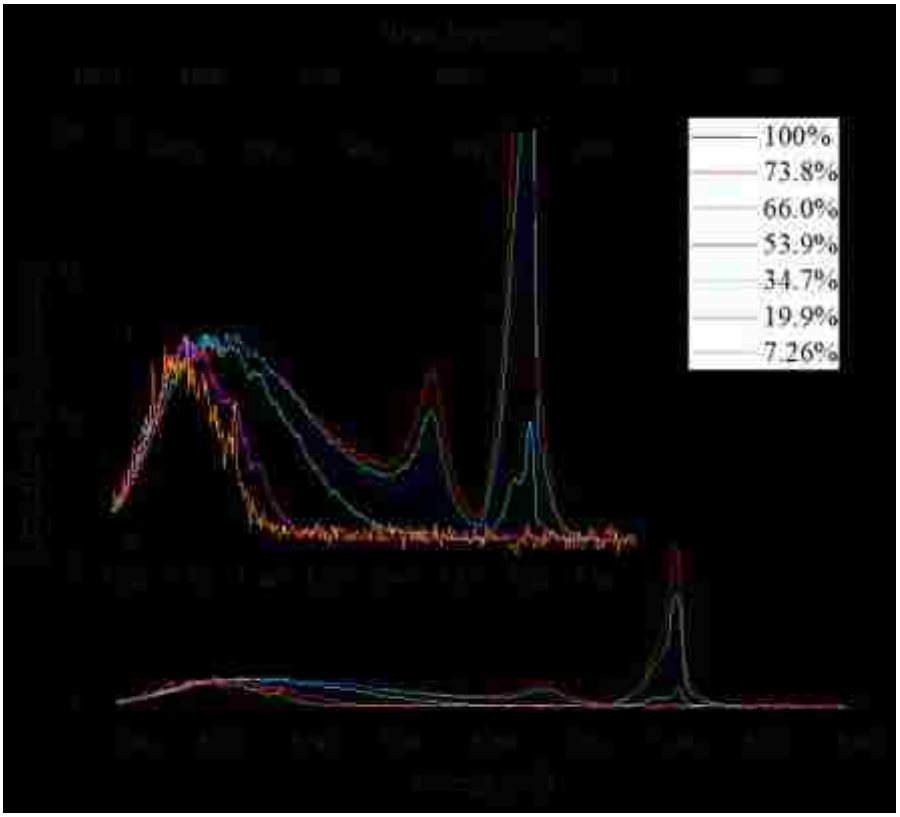

Figure 3.5. Normalized 2hυ excited PL spectra of EQDs with 0.622eV excitation.


Figure 3.6. (a) Excitation power dependent integrated PL intensity of EQDs with 0.622eV excitation. Red line is the power law fitting: $PL = a \cdot I^s$ with power index s = 2.19. (b) Power law index of multiple EQDs samples at various 2hυ excitation energies.

3.4 Two-photon Excited Power Dependent PL of WL and GaAs

Before we study the PL behavior of WL and GaAs substrate with 2hυ excitation, let's review their PL behavior with 1hυ excitation. In the end of Section 2.3, we conclude based on our rate equation model that with 1hυ excitation, $PL_{GaAs} \sim I^2, PL_{WL} \sim I^s$, where $1 < s < 2$. This is confirmed with the results of their 1hυ excitation power dependent PL as shown in Figure 3.7. Figure 3.7(a) is a representative data of the integrated PL intensity as a function of excitation power fraction (I_1/I_{10}). As we can see, the integrated GaAs PL has a quadratic dependent with the 1hυ excitation intensity, while the integrated WL PL has a power dependent between linear and quadratic. Multiple spots on the WL only region and the GaAs substrate were investigated and the power indexes of them are presented in Figure 3.7(b). An index of 2 for GaAs and between 1 and 2 for WL is quite repeatable.

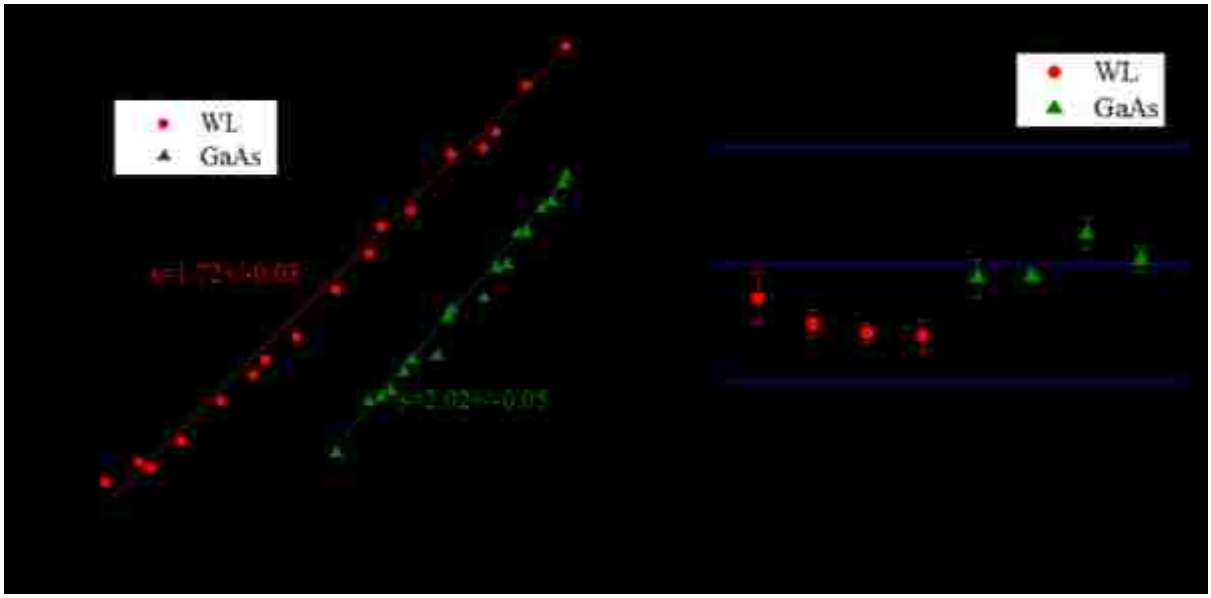

Figure 3.7. (a) One-photon excitation power dependent integrated PL intensity of WL and GaAs substrate. Straight line is the power law fitting: $PL = a \cdot I^s$ with power index s = 1.72 for WL and 2.02 for GaAs substrate. (b) Power law indexes of multiple WL samples and GaAs substrate samples. Error bars present the standard error of power law fitting.

With 2hυ excitation energy of 1.244eV, below WL and GaAs bandgap, the normalized PL spectra of WL only area on SF094 and a piece of GaAs substrate at different excitation power

are shown in Figure 3.8(a) and (b). The WL spectra are normalized to the WL peak, while the GaAs spectra are normalized to the GaAs peak. On both samples, the peak at 1.244eV is the second harmonic generation of the excitation from the bulk GaAs. This peak moves as the excitation energy moves and it always present at twice of the excitation energy. On the WL sample, the WL peak first starts to show at low excitation power, then GaAs bandgap starts to emit as the power increases. The GaAs peak is lower than the WL peak at the beginning but it grows faster than the WL peak and surpasses the WL peak after 74% I_{20}. This observation of the WL and GaAs emission on the no QDs region indicate that the 2hυ excited WL and GaAs emission are not, or not fully, from a process involving QDs state. On the GaAs substrate, the bandgap emission is also observed even with 2hυ excitation energy of 1.244eV. And its intensity is in the same order of magnitude as the GaAs peak from the WL only region. This implies that, in our samples, the WL is not playing the major role in the GaAs emission.

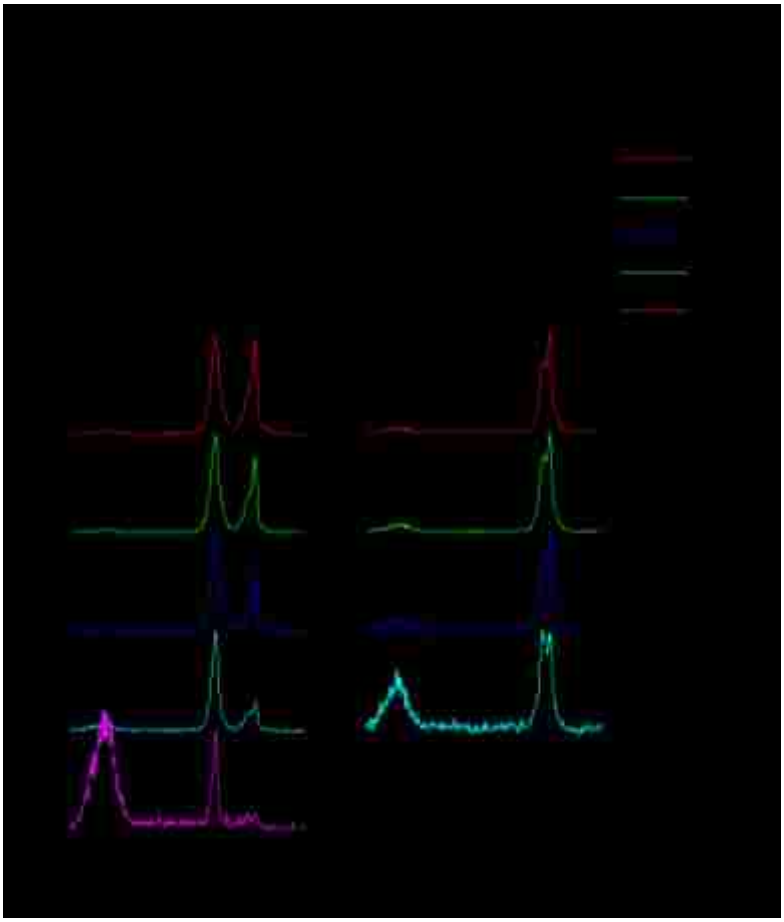

Figure 3.8.Two-photon excited PL spectra of (a) WL only area of SF094 and (b) GaAs substrate with 2hυ excitation energy of 1.244eV.

The power law fitting of the WL peak and the GaAs peak from the GaAs substrate are presented in Figure 3.9(a).

The power index for WL peak is about 3.87 and that for GaAs peak is about 4.92. We performed excitation power dependent study with various 2hυ energies. The power law exponents with these excitations are presented in Figure 3.9(b). As we can see, the WL power index falls between 3 and 5, more than twice of its 1hυ excited PL power index (between 1 and 2). The GaAs power index, falling between 4 and 6, is also more than twice of its 1hυ excited PL power index (which is 2). This indicates there is multiple-photon (more than two) involved in the absorption process of the WL only region and the GaAs substrate.

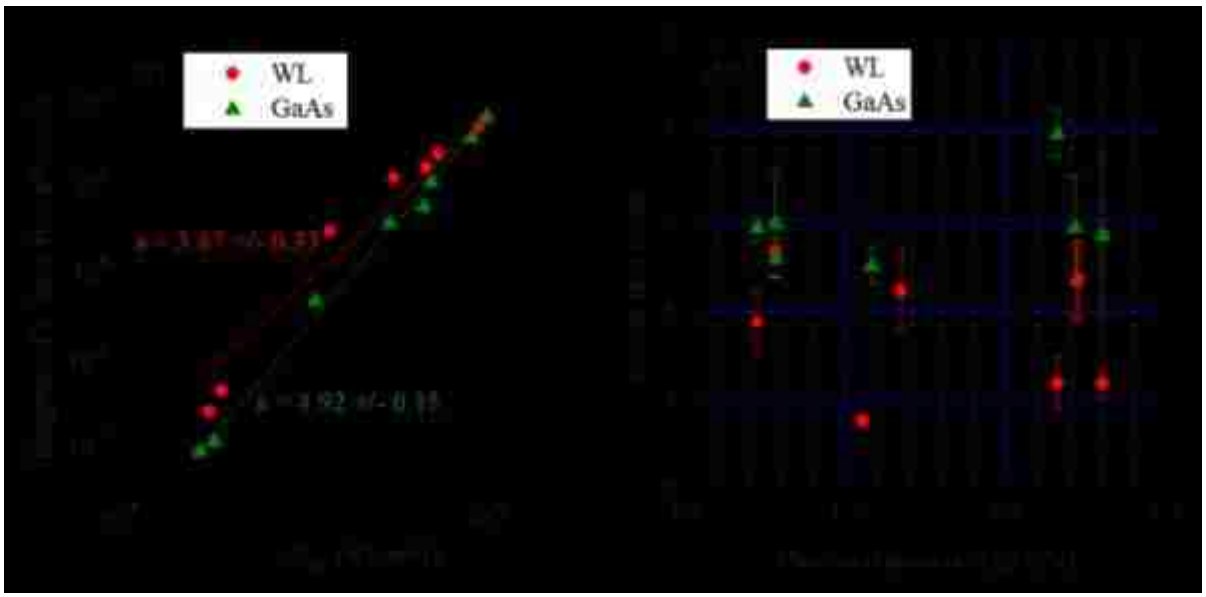

Figure 3.9. (a) Excitation power dependent integrated PL intensity of WL and GaAs substrate with 1.244eV excitation. Straight line is the power law fitting: $PL = a \cdot I^s$ with power index s = 3.87 for WL and 4.92 for GaAs. (b) Power law index of WL and GaAs at various 2hυ excitation energies.

Up-converted PL of S.I. GaAs was reported before by Johnson *et al.* [65] and Quagliano and Nather [66]. In Johnson *et al.* 's study, they observed up-converted GaAs PL with 1.39eV continuous-wave laser excitation. They attributed this upconversion to a two-step excitation through the deep level – defect formed electron-level 2 – as indicated by their PLE study, in which a continuously increasing GaAs PL was observed from 1.35eV to 1.50eV. Quagliano and Nather observed GaAs bandgap emission with 1.17eV continuous-wave laser excitation. This

up-conversion is explained by two-step TPA in which defects formed deep centers serve as the intermediate level. In contrast to our results, the up-converted GaAs PL in their research has a linear dependence with the 1.17eV excitation. They explained this linear behavior by saturation of one of the two transitions involved in the up-conversion. In their photoluminescence excitation (PLE) study, a gradually increased GaAs PL was observed when the excitation energy increased from 0.8eV to 1.25eV. In addition to these two research, Sturge [67] investigate the absorption of high-resistivity GaAs in the range of 0.6 to 2.75eV. He found that absorption below the GaAs bandedge varies substantially from sample to sample, and is presumably due to impurities. Based on these discoveries and our power law index, we can conclude that the 2hυ excited GaAs emission in our case is from three-photon absorption through deep levels formed by defects.

3.5 Two-photon PLE of EQDs

In Section 3.3, we leant that the EQDs have a quadratic relationship with the 2hυ excitation power. This tells us that there is 2hυ process involved in the absorption. But whether it is direct TPA or indirect TPA though some intermediate levels we don't know. To further distinguish this two process, we performed PLE measurement with 2hυ excitation. PLE is a useful tool to elucidate absorption channels. In a PLE measurement, a fixed emission energy is monitored while the excitation energy is scanned. Peaks in a PLE spectrum often represent the absorption lines of the sample. In our 2hυ PLE measurement of the EQDs sample, the integrated PL of QDs within the range of 1.20eV to 1.30eV is monitored while the 2hυ excitation energy is scanned from 1.22eV to 1.53eV, corresponding to 0.610eV to 0.765eV 1hυ energy. If the TPA is through some intermediate levels, when the excitation energy is in resonance with it there should

be an enhancement in the EQDs PL. On the other hand, if the TPA is direct TPA in QDs, there will be enhancement when the 2hυ excitation energy is in resonance with the QDs transition energies.

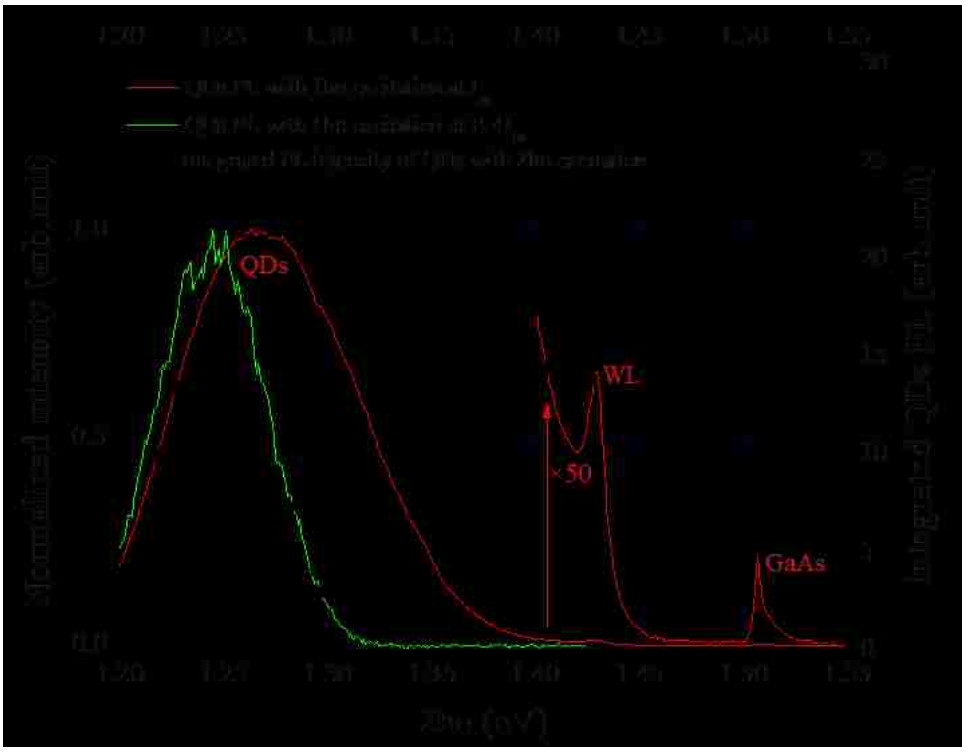

Figure 3.10. Integrated QDs PL as a function of 2hυ excitation energy.

Figure 3.10 shows the EQDs emission as a function of 2hυ excitation energy as black squares, the black line is for eye guidance. Normalized QDs PL with 1hυ excitation at low (0.01%I_{10}) / high (I_{10}) power is also shown in the figure as green/red curve for comparison. The low power 1hυ excited PL reveals the ground states distribution of the QDs, and the high power one illustrates the distribution of excited states of QDs as well as the WL states and GaAs bandedge. The WL and GaAs peaks are magnified by 50 (marked by a red arrow) to make them easier to be seen. As we can see from the graph, starting from the low energy side, the PLE spectrum represents quite well the energy distribution of the ground state of the QDs ensemble. This indicates that there is 2hυ absorption into the QDs ground state. When the 2hυ excitation

energy is between 1.30eV and 1.43eV, there are two rises on the PLE curve around 1.32eV and 1.39eV. We attribute these to 2hυ absorption in the first and second excited state of QDs. Although the excited states of these QDs are not resolved in the 1hυ PL characterization due to the wide size distribution of the QD ensemble, we can estimate their positions by published values and our similar sample, like SF077. For SF077 (Figure 2.3(b)), the ground transition is located at 1.10eV and the energy difference between each excited state is about 60meV. As for SF094, the ground transition is at 1.24eV, higher than those of SF077, indicating smaller QDs. Therefore, their excited state would have a bigger energy difference than SF077. An energy difference between 30 to 70meV has been reported for In(As)Ga QDs [56], [57]. So the assumption that the energy difference between the states of SF094 is about 70meV is reasonable, and the enhancement of the PLE signal at 1.32eV and 1.39eV can be assigned to 2hυ absorption in the excited states of the QDs. When the excitation crosses the WL state at 1.43eV, the PLE signal climbs again, demonstrating 2hυ absorption in the WL. Therefore, with this PLE result, we can tell that direct TPA is the main absorption mechanism in our QDs 2hυ excited PL.

4 Photoluminescence of Single Quantum Dot

4.1 Sample Morphology and PL Characterization

In this chapter, we will discuss PL behavior of a single InAs/GaAs QD under 1hυ and 2hυ excitation. The sample used in this chapter is the low QDs density area of SF094 (p8 in Figure 3.1). The density of QD is below $10^8 cm^{-2}$, which makes it easier to optically isolate a SQD. Figure 4.1 shows the TEM image of a typical uncapped self-assembled InAs SQD on GaAs. It has a lens shape with a height of 6.0nm and base diameter of 32.1nm.

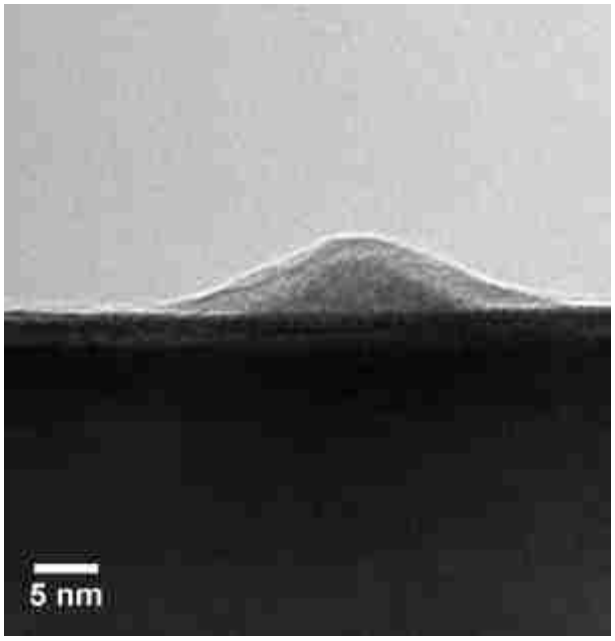

Figure 4.1. TEM image of a single InAs/GaAs QD.

PL characterization is done with Horiba LabRAM HR800 system and He-Ne laser. The sample was kept at 5K in a cryostat with liquid Helium flow. Figure 4.2 shows the spectrum of a SQD. We can see this SQD has three energy shells: s-shell (ground state) at 1.30eV, p-shell (1^{st} excited state) at 1.35eV and d-shell (2^{nd} excited state) at 1.40eV. The s, p, d denotation is in analogy to atomic physics. There are two main reasons that we assign these three emissions as the three shells from a SQD instead of from three QDs. Firstly, the three emissions are from the same physical location on the sample. Considering the low QD density ($1\mu m^{-2}$), the probability of three QDs located at one spot within 0.5μm resolution is low. Secondly, the energy separation between these three emissions is about 50meV which agrees with the reported value [56], [57].

These QD energy shells can hold an increasing number of carriers according to the Pauli exclusion principle. In a QD with perfect symmetry and without considering the Coulomb interactions between carriers, energy levels within one shell are degenerate. The ground state is two-fold spin degenerate and can hold two electron-hole pairs. The 1st excited state is doubly degenerate and can hold up to four electron-hole pairs. The 2nd excited state is six-fold degenerate and can hold up to six electron-hole pairs. But in reality, the degeneracy is removed by multicarrier interactions, and the energy levels are further split up by the asymmetry of the QD as well as the electron-electron, hole-hole, and electron-hole exchange interaction. Therefore, multiple emission peaks from each shell are observed. Identification of each of these peaks requires analysis from different measurements including excitation power dependent PL, bias dependent PL [68], polarized PLE [69] and magneto-PL [57].

Figure 4.2. PL spectrum of a SQD at 5K.

4.2 One-photon Excited Power Dependent PL of SQD

In this section, we will show the power dependent PL study of a SQD with 1hυ excitation. The experiment was performed with Horiba LabRAM HR800 system and He-Ne laser. The sample was cooled to 5K in a continuous flow cryostat using liquid helium.

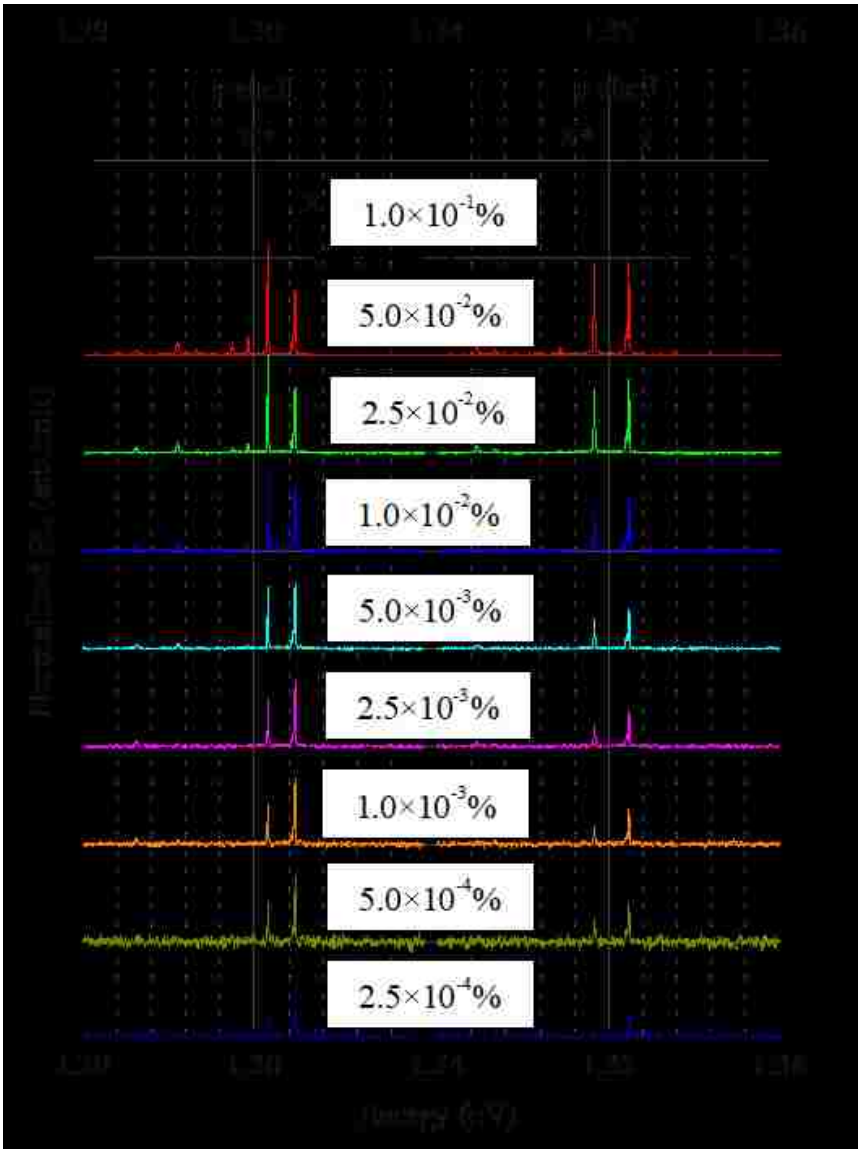

Figure 4.3. Normalized 1hυ excited PL spectra of SQD with varying excitation power. 100% power equals to I_{10} ~ 6mW.

Power dependent PL of SQD with 1hυ excitation is shown in Figure 4.3. The intensity is normalized to the peak at 1.3024eV (labeled as X of s-shell in the figure). Here we only show the

evolution of s-shell and p-shell peaks since the d-shell only appeared at high power. We pick four highest peaks for further analysis: 1.3008eV, 1.3024eV, 1.3493eV and 1.3512eV. They are identified as s-shell neutral exciton (X) and charged exciton (X*) transition, p-shell neutral exciton (X) and charged exciton (X*) transition respectively. The identification process will be discussed below.

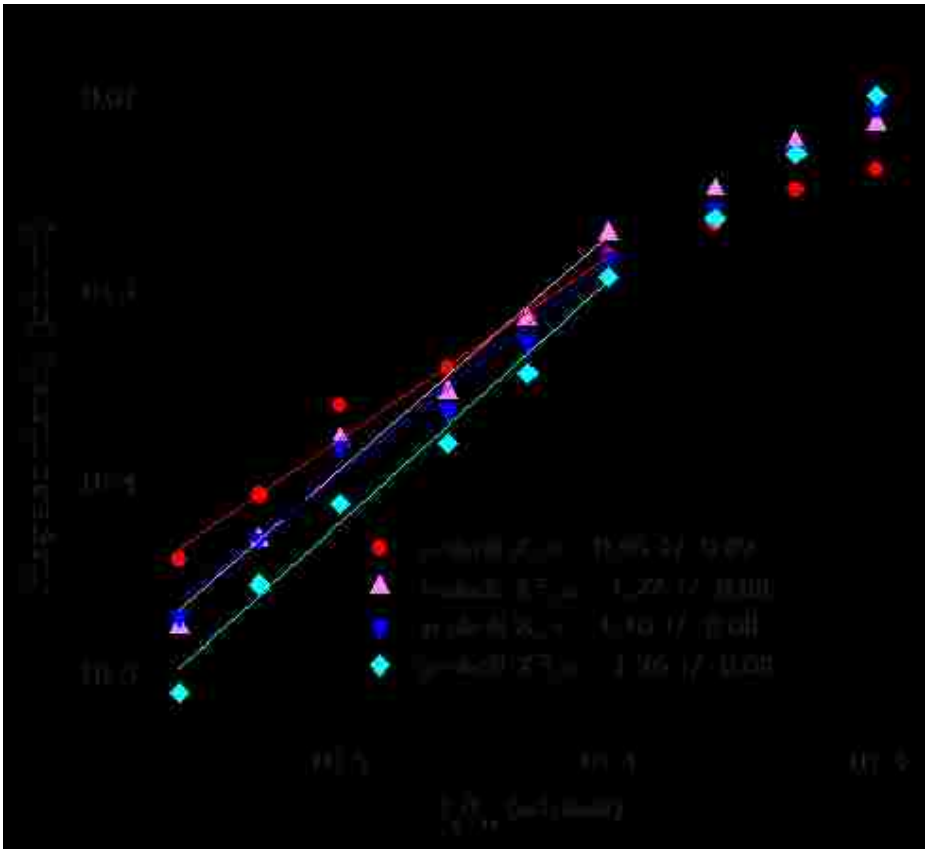

Figure 4.4. Excitation power dependent integrated PL intensity of four SQD peaks with 1hυ excitation. Straight line is the power law fitting: $PL = a \cdot I^s$ with power index s = 0.95 for s-shell X, 1.22 for s-shell X*, 1.10 for p-shell X, and 1.26 for p-shell X*.

With non-resonant excitation, a QD captures electrons and holes separately and may be populated with an uneven number of electrons and holes. At low excitation power, fewer carriers are created therefore the X line of s-shell should show first as it requires the minimum number of carriers (one electron and one hole). As power increases, X* of s-shell would show second. Its

energy will be a few meV from the X line, on either the higher or the lower side [70], as the extra carrier (electron or hole) shifted its energy through additional Coulomb interactions. If the QD is populated with more carriers, XX (neutral biexciton) transition would show up next. After this, carriers will start to fill the P-shell. Similarly, the X line of P-shell will appear first, followed by X* line. Apart from this appearance order, the relationship between PL intensity and excitation power can help us to distinguish XX from X and X* since XX intensity has a square dependence on excitation power while X and X* increases linearly with excitation power [56], [71], [72]. The intensity v.s. excitation power relation of the four highest peaks in Figure 4.3 is plotted in Figure 4.4. Straight lines are the power law fitting. The points above 1E-4 I_1/I_{10} are excluded from the fitting since there may be saturation in the PL intensity at high excitation power. As we can see all four peaks is linearly dependent with excitation power, indicating they are either X or X*. We assign the 1.3008eV peak as s-shell X* since its intensity is lower than the 1.3024eV peak at low excitation power, but higher at high power. Because at high power, more carriers are generated, and it is more likely to form X*. The 1.3024eV is then assigned as s-shell X peak. Same reason, the 1.3493eV peak is identified as P-shell X* and the 1.3512eV peak is identified as p-shell X.

4.3 One-photon Excited Temperature Dependent PL of SQD

Temperature dependent PL of the same SQD is presented in Figure 4.5. Intensity is normalized to s-shell X or X* peak, whichever is higher. As we can see, all the emission lines show broadening and redshift as temperature increases. We will discuss in detail the FWHM and peak center as a function of the temperature of the four peaks that we identified in the previous section.

Figure 4.5. Normalized temperature dependent SQD PL with 1hυ excitation.

At 10K, the peaks show a Lorentzian profile with a FWHM of about 150μeV, limited by the instrument resolution. As temperature increases, a broad background emission band appears on both sides of all the peaks. This background is due to acoustic phonon scattering [73]. Figure 4.6(a) displays the temperature dependent FWHM of the X and X* peaks of s-shell and p-shell. The solid line is the fitting function [74]:

$$\omega = \omega_0 + aT + b/(\exp(\frac{E_{LO}}{kT}) - 1) \ . \tag{4.1}$$

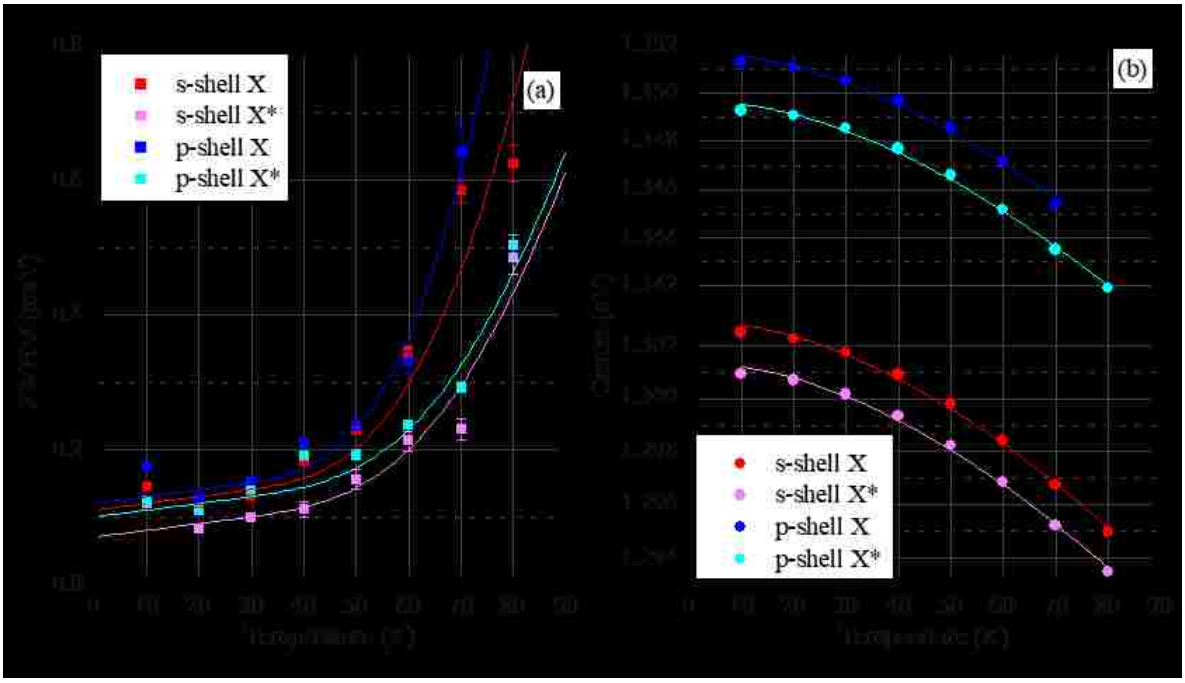

Figure 4.6. (a) FWHM and (b) peak center of the X and X* peaks in S-shall and P-shell as a function of temperature. Solid lines are fitting functions:
(a) $\omega = \omega_0 + aT + b/(\exp(\frac{E_{LO}}{kT}) - 1)$; (b) $E = E_0 - \alpha T^2/(T + \beta)$. The error bars in (a) indicated standard error of fitting each peak with a Lorentzian function. The error bars in (b) is in the order of 10^{-6}, thus too small to see.

The term ω_0 is the temperature-independent broadening due to scattering by impurities and imperfections. The second term aT represents the acoustic phonon broadening, which is linearly dependent on temperature. The last term $b/(\exp(\frac{E_{LO}}{kT}) - 1)$ is the optical phonon broadening and it is proportional to the Bose function for the LO-phonon occupation number. Table 4.1 lists the fitting parameters for each peak. When $T <$ 50K, the PL broadens slowly mainly due to acoustic phonon scattering; when $T > 50$K, fast PL broadening is observed because of optical phonon scattering.

Table 4.1. Fitting parameters for each peak plotted in Figure 4.6 (a).

Fitting function: $\omega = \omega_0 + aT + b/(\exp(\frac{E_{LO}}{kT}) - 1)$			
	ω_0(meV)	a(μeV/K)	b(meV)
s, X	0.11	1.00	35
s, X*	0.07		7
p, X	0.12		19
p, X*	0.10		7

Figure 4.6(b) displays the temperature dependent peak center of the X and X* peaks of s-shell and p-shell. The temperature-dependent energy shift is believed to arise from two mechanisms: volume dilatation and electron-lattice interaction. The first one is nonlinear with T at low temperature and linear with T at high temperature. The second one is the major contribution to the energy shift and it is linearly-dependent with temperature when $T \gg \theta$, and quadratically-dependent with temperature when $T \ll \theta$, where θ is the Debye temperature. The peak energy for our four peaks can be well fitted to Varshni Law [75]:

Table 4.2. Fitting parameters for each peak position as a function of temperature.

Varshni Law: $E = E_0 - \alpha T^2/(T+\beta)$, $\beta = 271K$.			
	E_0(eV)	α (μeV/K)	Adj.R^2
s, X	1.3029	426.76	0.9955
s, X*	1.3014	424.10	0.9960
p, X	1.3517	422.66	0.9959
p, X*	1.3497	423.36	0.9920

$$E = E_0 - \frac{\alpha T^2}{T+\beta} \quad , \tag{4.2}$$

where E_0 is the energy at 0K, α and β are constants. For InAs material, we take $\beta = 271K$ [76]. Table 4.2 lists the fitting results for each peak.

4.4 Two-photon Excited PL of SQD

In this section, we will show the 2hυ excited PL of the SQD discussed in the previous two sections. The experiment setup is the same as the one used for 2hυ excitation of EQDs described in Section3.3. But the sample temperature was kept at 5K. For SQD PL study, we suppose to use the 1200g/mm grating in the spectrometer so that the linewidth of the SQD's PL can be resolved. But we could not get any signal beyond the noise with this grating. With 150g/mm grating, which has a higher efficiency, the SQD PL became detectable. But we lost the linewidth information.

Based on the previous result of 2hυ excited EQDs, we know that the QDs PL presents with 2hυ excitation ranging from QDs ground state all the way up to barrier bandedge. Therefore, after locating a SQD with 1hυ excitation, we start with 2hυ excitation resonate with the WL state and scan the 2hυ excitation all the way to the SQD's ground state. The PL result is shown in Figure 4.7. The legend denotes the micrometer reading of the wavelength tuning crystal of the OPA. PL with 1hυ excitation is plotted at the bottom for comparison. As we can see, when 2hυ excitation is higher than the SQD's excited state (from M6p25 to M5p95), both the SQD's ground state and excited state emission can be clearly observed. From M5p80 to M5p50, when

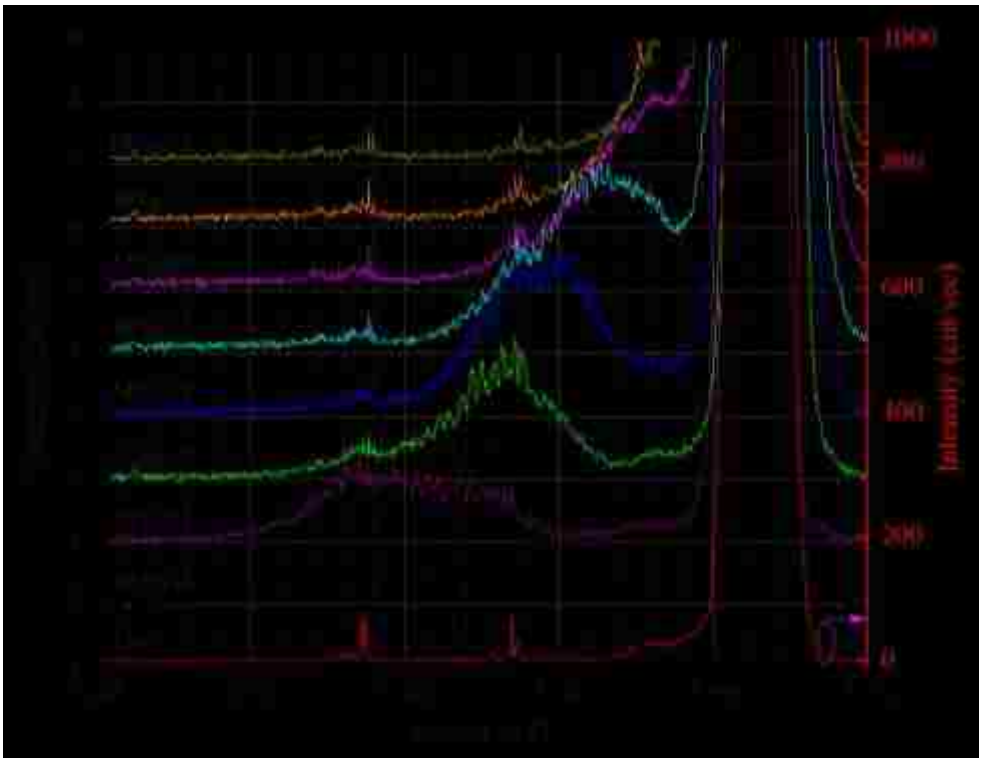

Figure 4.7. SQD spectra with various 2hυ excitation energies at 5K.

the 2hυ excitation energy comes across with the SQD's excited state, the ground state emission is still clearly seen whereas the excited state emission becomes indistinguishable because of the SHG peak of the excitation. Similarly, as the excitation move to the SQD's ground state (M5p35 and M5p30), the SHG peak overlaps with the SQD's PL, making the features of the SQD's PL

indistinct. In our attempt of excitation power dependent and temperature dependent study discussed below, we used 2hυ excitation energy resonates with the SQD's excited state. Therefore we resonantly excite the SQD and we are still able to monitor the PL from the ground state transition.

In our attempt of excitation power dependent study, the ground state transition can only be observed within a very small change of excitation power. Figure 4.8 shows the SQD PL spectra at $0.35I_{20}$ and $0.07I_{20}$. At lower power, the PL signal immerses into the noise while at higher power it submerges into the tail of the SHG peak. Therefore, our experimental setup is limited for power dependent study of SQD with 2hυ excitation.

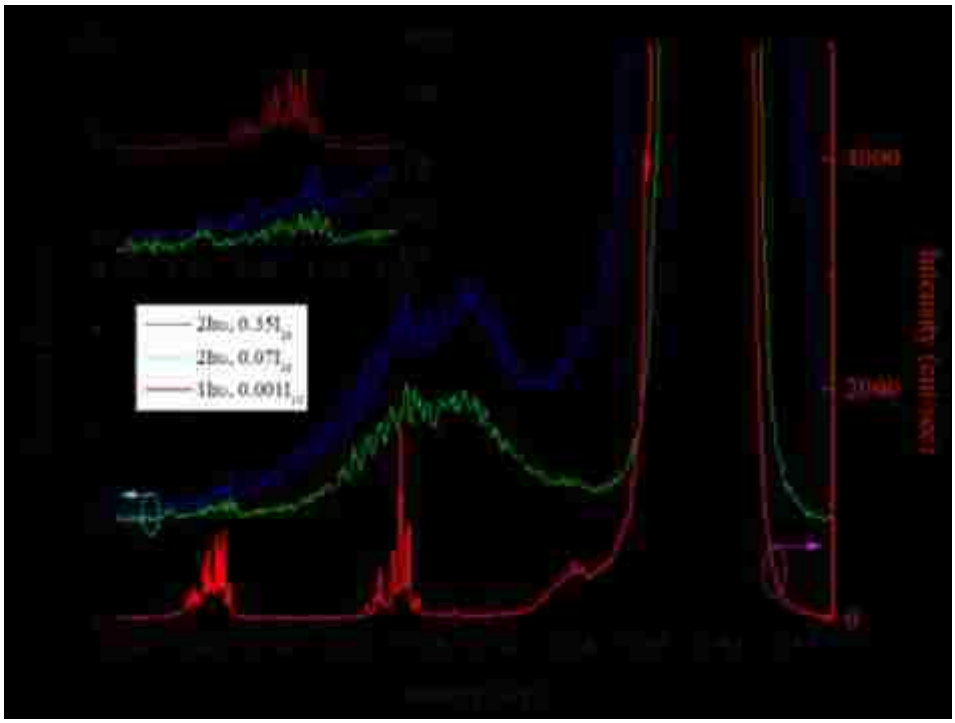

Figure 4.8. SQD PL with 2hυ excitation at two powers. PL with 1hυ excitation is plotted for comparison.

In our attempt of temperature dependent SQD PL study, we are able to monitor the ground state emission's position change as a function of the temperature. Figure 4.9 shows the spectra of the SQD PL with 2hυ excitation at different temperatures. The ground transition can

be seen in the shaded area. Figure 4.9(b) plots the ground transition peak position as a function of temperature for both 1hυ and 2hυ excitation. The solid line is the fitting function by Varshni Law (Eq.(4.2)) for 2hυ excited peak with fitting parameters: $E_0 = 1.3027\text{eV}$, $\beta = 271\text{K}$, $\alpha = 425.46\text{meV}$. The peak center by 2hυ excitation coincides with the one by 1hυ excitation, and it follows the Varshni Law well, confirming its identity as SQD PL. Linewidth information, as mentioned before, is limited by the low-resolution grating we used.

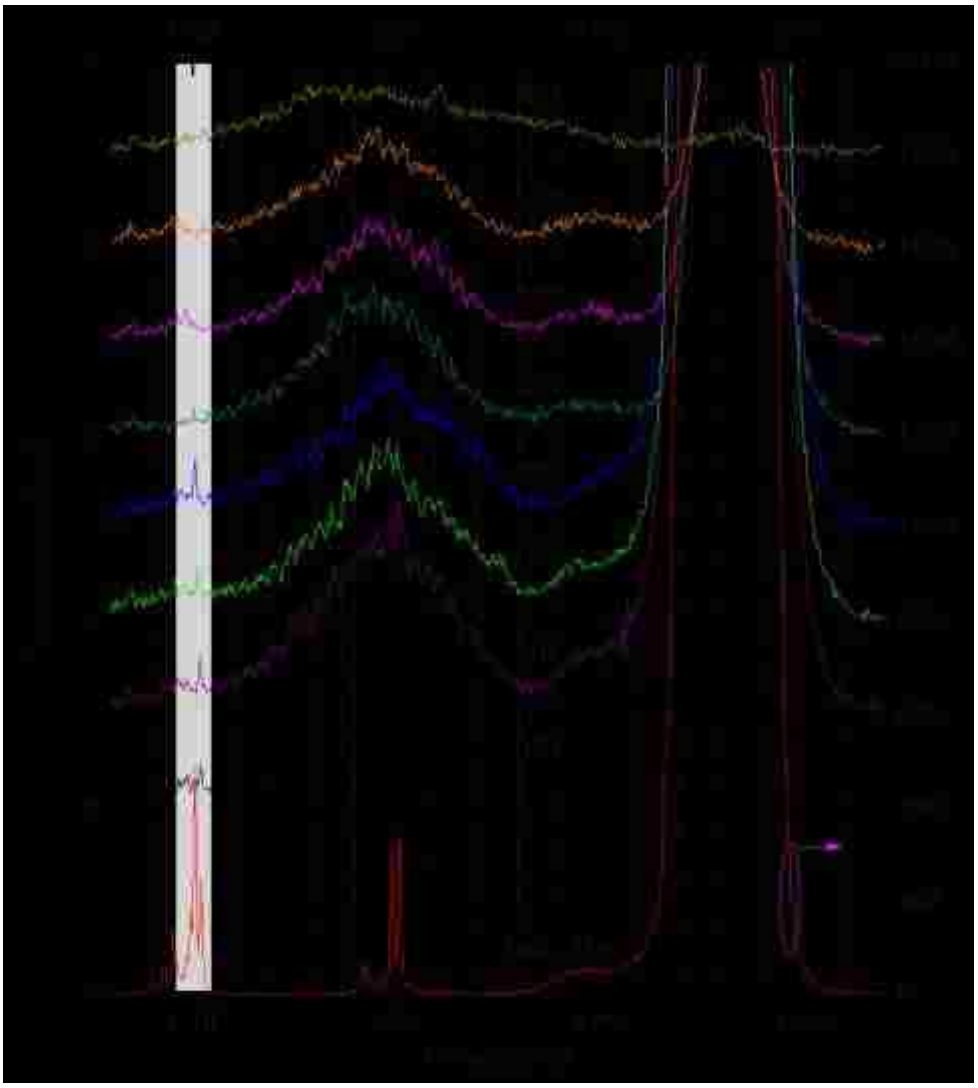

Figure 4.9. Two-photon excited SQD PL at various temperatures. The bottom red curve is 1hυ excited SQD PL at 10K, plotted for comparison.

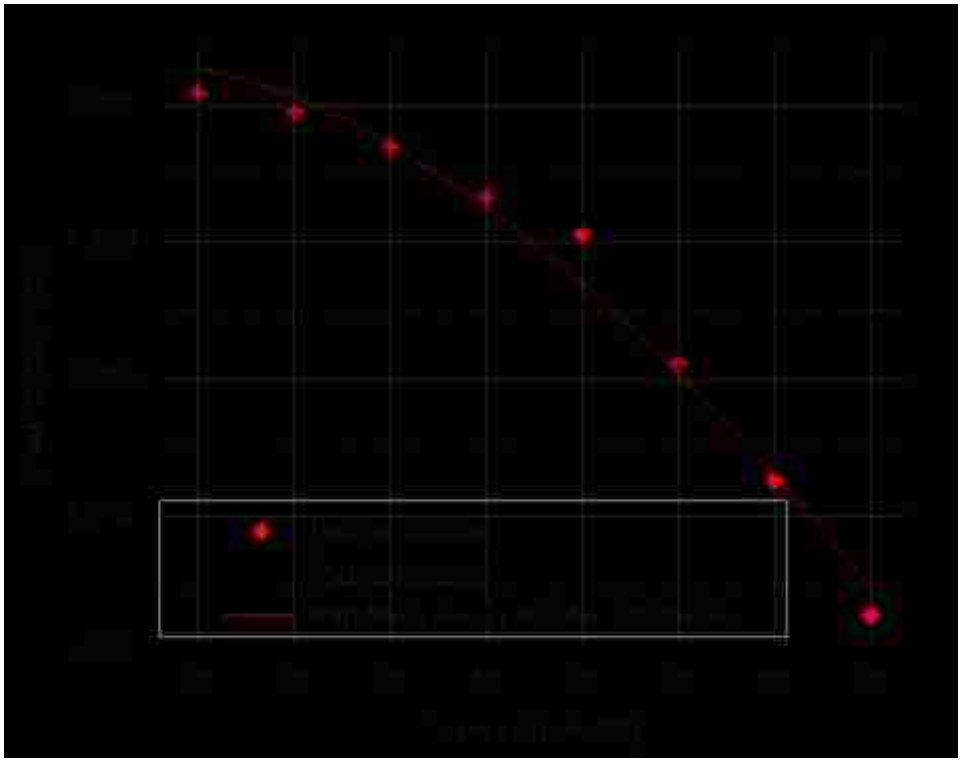

Figure 4.10. Ground transition (gray area in Figure 4.9) peak position as a function of temperature. Solid line is the fitting function by Varshni Law as in Eq.(4.2).

5 Photoluminescence of Single Quantum Dot in Micro-Cavity

5.1 Sample Morphology, Reflectance and PL Characterization

SF096 is the sample used for QDs-in-cavity study. It consists of 25.5 pairs of AlAs/GaAs DBR on the bottom, 11 pairs DBR on the top and one-wavelength GaAs cavity in between with one layer of InAs QDs in the middle of the cavity. A TEM image of the structure is shown in Figure 5.1. Details about the transmission electron microscope can be found in Appendix C. The image is taken under dark-field mode, in which material with less nuclear mass will appear darker. So in Figure 5.1(a), the dark stripes are AlAs and light stripes are GaAs. The brightest spots in Figure 5.1(b) are InAs QDs.

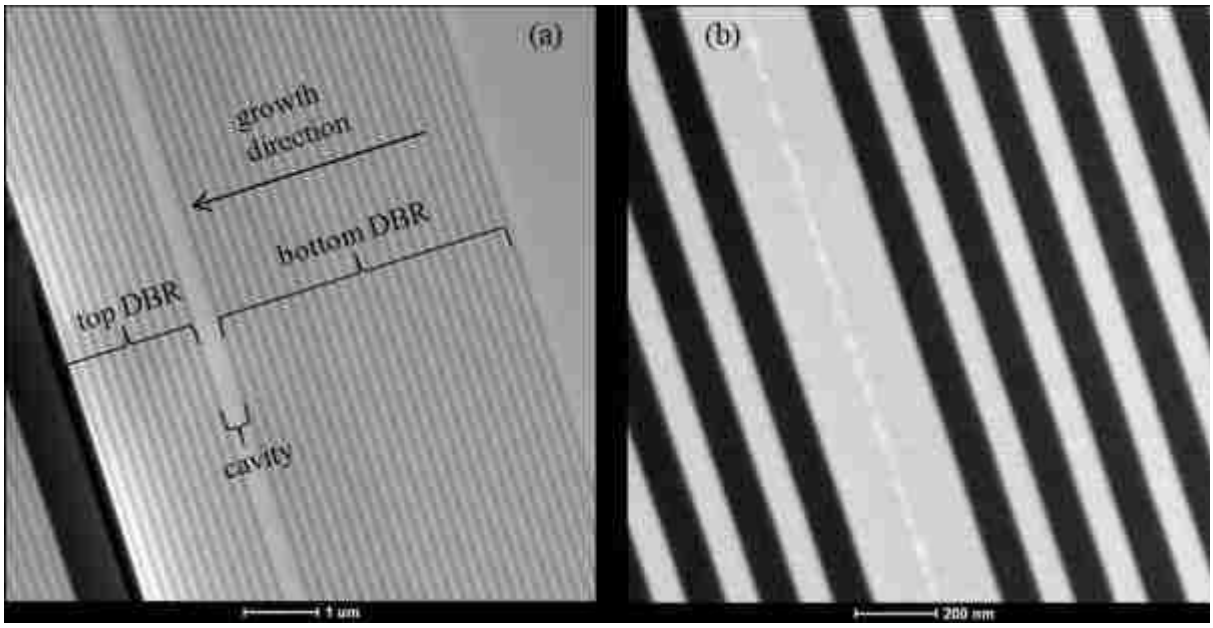

Figure 5.1. (a) TEM image of QDs-in-cavity sample. (b) Zoom in image of the cavity.

Room temperature reflectance simulation (with normal incidence) and experimental result are shown in Figure 5.2. The experimental result is normalized to its maximum value. As we can see, the experimental result repeats the main feature of the simulated data pretty well. The whole spectrum shifted to the shorter wavelength compare to simulation. This indicates the

actual layer thickness is less than the designed one. The cavity notch, which is shifted as well, is less sharp than the simulation result. We attribute this to the quality of the DBR mirrors.

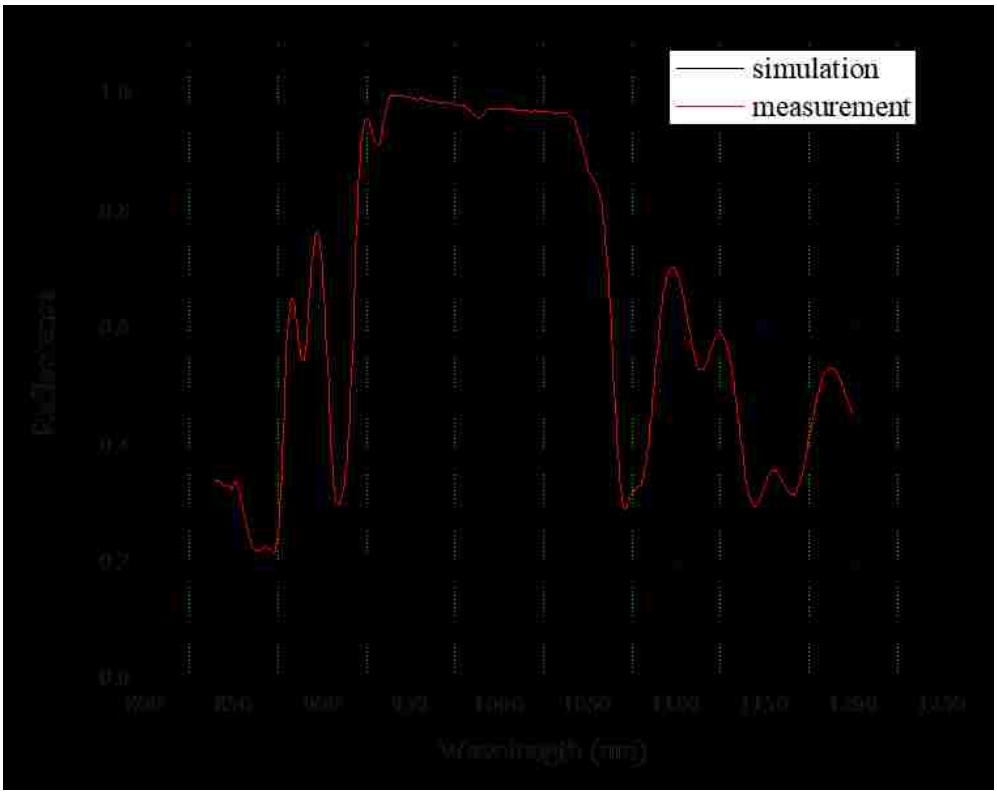

Figure 5.2. Simulated and measured reflectance spectrum of SF096.

PL was measured on different positions on the two pieces of cleaved sample at 10K. The excitation wavelength was 532nm and the intensity was about 1.21W/cm^2. Figure 5.3 shows the PL result at three positions: P1, P2, and P3. Positions on the sample are displayed in the insert of Figure 5.3. No emission from QDs was observed as we scan the sample from P6 to P5. The QDs emission started to show as we moved closer to P4. Based on the result of SF094, which has the same QDs recipe as SF096, we could tell that the QDs density should get higher and higher as go from P4 to P1. The shift of the emission peaks is due to the shift of the cavity notch as discussed above. The FWHM of the emission, around 5nm, agrees with the width of the cavity notch too. The strong peak at 820nm is GaAs bandedge emission, which is not blocked by the DBR.

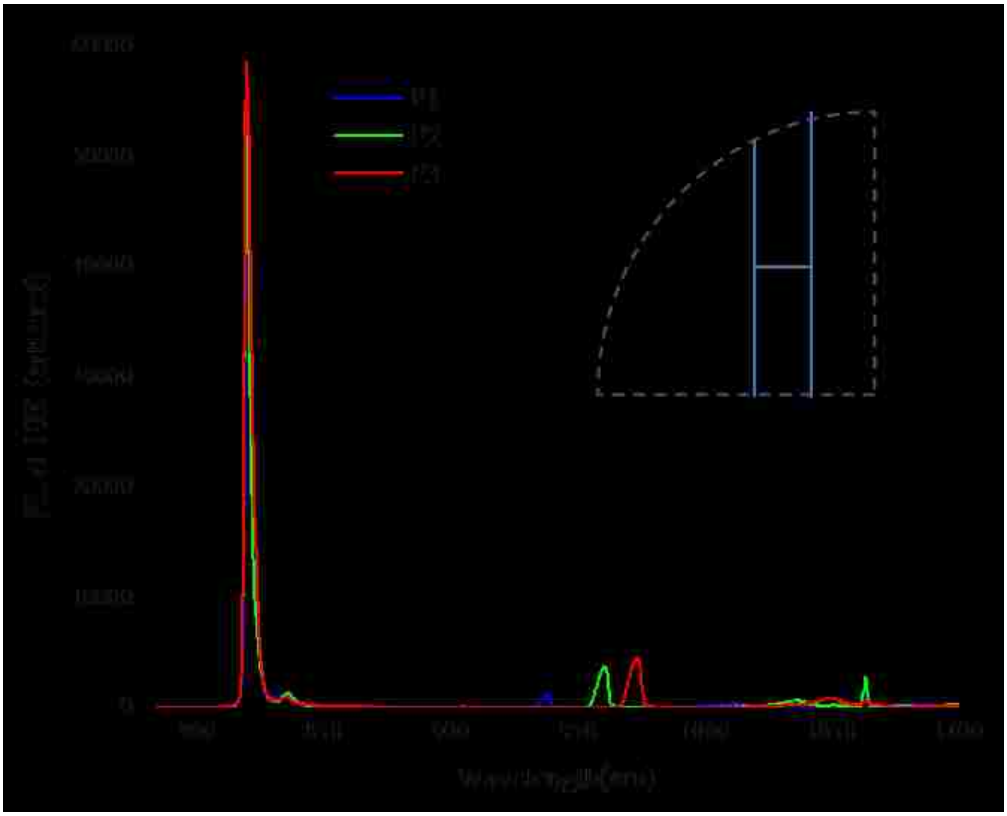

Figure 5.3. PL from different positions on SF096. Insert shows the rough positions on the sample. Dashed line is the quarter-inch wafer and solid line is where the sample was cleaved.

5.2 One-photon Excited Power Dependent PL of SQD-in-cavity

In this section, we will show the power dependent PL study of a SQD-in-cavity with 1hυ excitation. The experiment was performed with Horiba LabRAM HR800 system and He-Ne laser. The sample was kept at 10K with liquid helium.

To locate a SQD in sample SF096, we monitor the PL from the cavity notch while moving the sample along the direction of the QDs density change. From the temperature dependent study of SQD discussed in Section4.3, we know that the FWHM of a SQD PL is between 0.1meV and 0.2meV at 10K. Therefore, we would consider a SQD is pinpointed when we observe a PL peak with a FWHM within this range.

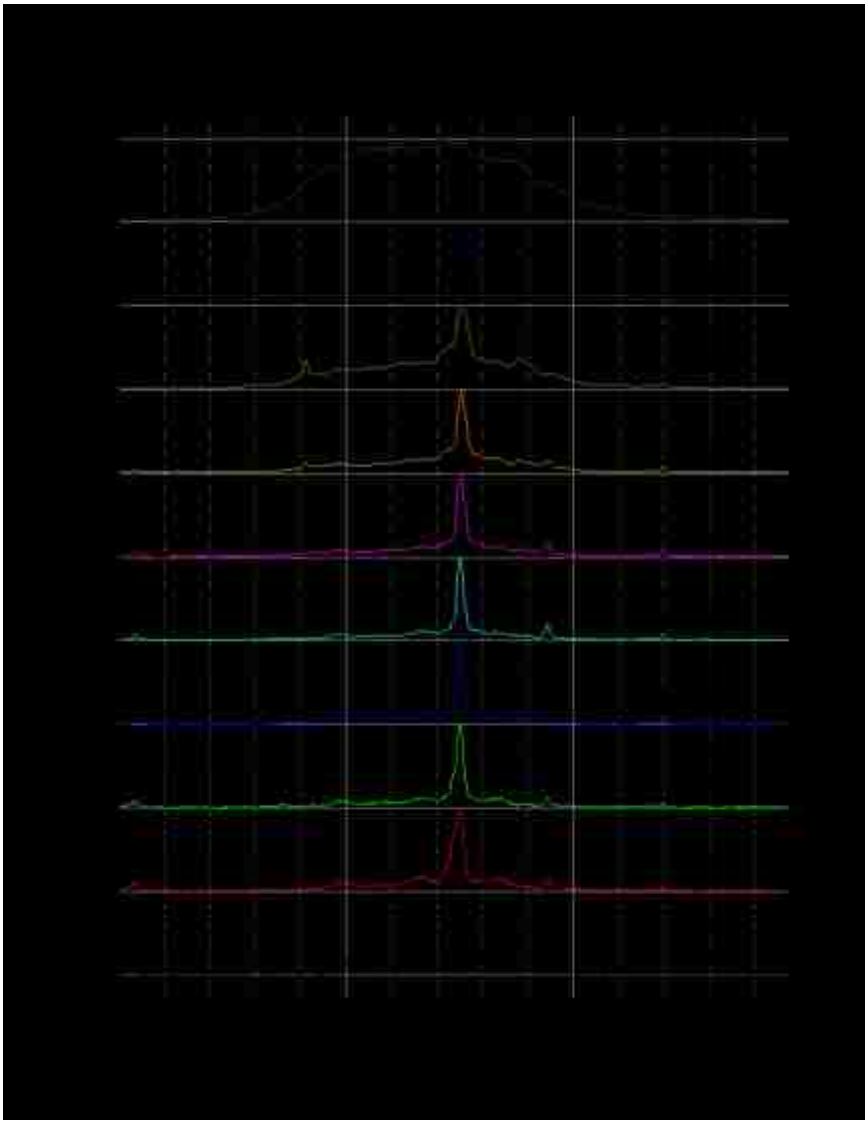

Figure 5.4. Normalized PL spectra of SQD-in-cavity at different 1hυ excitation powers. 100% power equals to I_{10} ~ 6mW.

Figure 5.4 presents the PL spectra of a SQD-in-cavity at various excitation powers. Each spectrum is normalized to its maximum. At 0.0032%I_{10}, a SQD peak at 1.2725eV is observed. As power increases, the SQD peak becomes more distinct. There are some other peaks, for example, the 1.2744eV peak and the 1.2691eV peak, can be seen within this excitation range. These peaks may come from other transitions of the same SQD. Below 3.2%I_{10}, the 1.2725eV peak is sitting on top of a board background emission, which we attribute to the acoustic phonon scattering [73]. When the excitation is higher than 3.2%I_{10}, the broad background becomes

remarkable and its shape differs from the acoustic phonon broadening of a SQD without a cavity. We assign this shape change to the cavity notch effect. The notch has a shape itself, when the excitation power is low, the PL signal is low and its shape is not affected by the notch. At high excitation power, the PL signal becomes strong but it is limited by the notch shape. Therefore, the PL at high excitation power deforms from its own shape which is presented at low excitation power.

Figure 5.5. Excitation power dependent integrated PL intensity of a SQD-in-cavity at 10K.

The integrated intensity as a function of the excitation power fraction of the 1.2725eV peak is plotted in Figure 5.5. The red straight line is the power law fitting function with a power law index s = 1.12. The highest three points are excluded from the fitting since the notch effect starts to play an important role in the PL shape and intensity. A power law index closed to one indicates that, at low excitation power, the cavity effect on the SQD PL intensity is linear respect to excitation power. This is not surprising, or contradict to the Purcell effect [77]. Although the

spontaneous emission rate of the SQD is modified by the cavity, each point in the excitation power dependent intensity figure would be shifted by the same ratio, resulting in no change in the power law fitting.

5.3 One-photon Excited Temperature Dependent PL of SQD-in-cavity

In this section, we will show the 1hυ excited temperature dependent PL of a SQD-in-cavity from sample SF096. As we will see, not only the SQD's emission shifts with temperature, the cavity transmission notch also varies with temperature. So the spectrum we get is a superposition of these two changes.

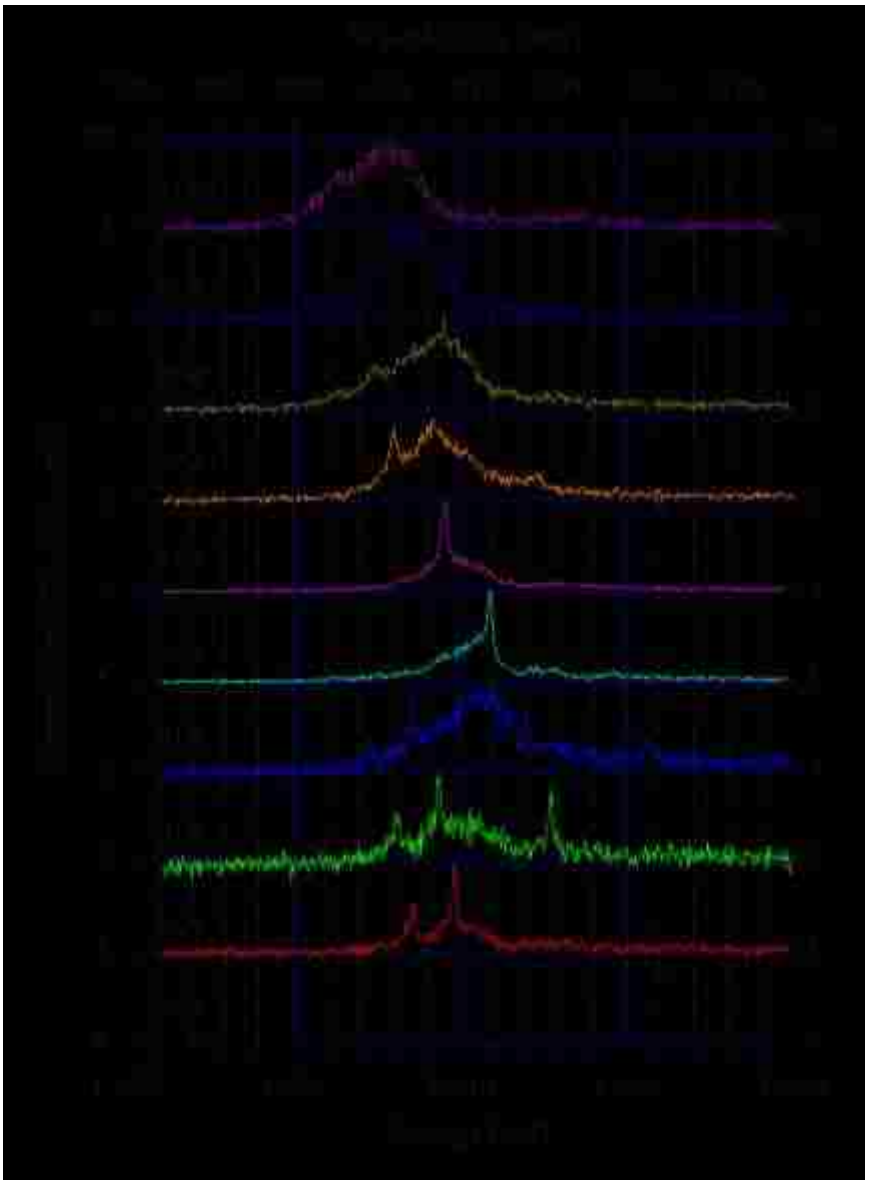

Figure 5.6. Normalized 1hυ excited temperature dependent PL of a SQD-in-cavity.

Normalized PL spectra at various temperatures are shown in Figure 5.6. At 10K, we can observe two peaks at 1.2688eV and 1.2700eV. We will label these two peaks as p1 and p2. They could be originated from one SQD or two different SQDs. At temperature increases, p1 and p2 shift to lower energy. They shift out of the transmission notch and cannot be observed anymore after 40K. Meanwhile, another peak at 1.2727eV starts to show at 30K. We label this peak as p3. It gradually redshifts into the notch and becomes strong at 50K and 60K. After 80K, it also moved out of the notch and can no longer be observed. The peak position as a function of the temperature of p1, p2, and p3 is plotted in Figure 5.7. The solid line is the fitting function by Varshni Law (Eq.(4.2)) with the fitting parameters presented in Table 5.1. As we can see, the peak position still follows Varshni Law quite well. The cavity notch also redshifts as temperature increases. This is due to the lattice expansion which shifts the transmission wavelength to a longer wavelength. But it has a smaller shift comparing with the SQD's emission.

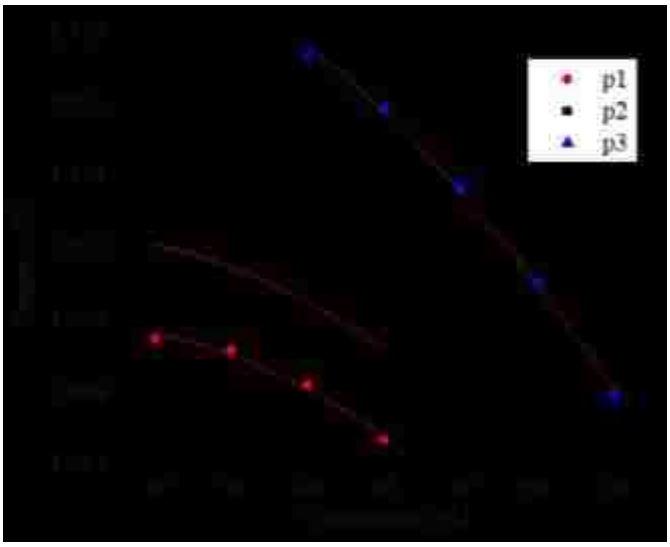

Figure 5.7. Varshni Law fit of the center position of p1, p2, and p3.

Table 5.1. Fitting parameters for each peak position as a function of temperature.

Varshni Law: $E = E_0 - \alpha T^2/(T+\beta)$, $\beta = 271K$.			
	E_0(eV)	α (μeV/K)	Adj.R^2
p1	1.2702	301.49	0.9753
p2	1.2690	299.47	0.9764
p3	1.2741	417.88	0.9976

5.4 Two-photon Excited PL of SQD-in-cavity

In this section, we will show the 2hυ excited PL of a SQD-in-cavity from sample SF096. The experiment setup is the same as the one used for 2hυ excitation of EQDs described in Section3.3. But the sample temperature was kept at 10K. The 2hυ excitation energy we used here is about 1.41eV. This energy was chosen such that it is below the GaAs bandgap and above the QD ground state transition.

Figure 5.8 presents the Normalized PL spectra of a SQD-in-cavity at various 2hυ excitation powers. Normalized PL spectra of the same SQD with 1hυ excitation are also plotted for comparison. With 2hυ excitation, we were only able to get the PL signal with 100%I_{20} and 50%I_{20} power. The signal is below the noise with 32%I_{20} even with a 300 seconds acquisition time. From the figure we can see, this SQD has two strong peaks at 1.2706eV and 1.2710eV under 1hυ excitation. There are also some distinct satellite peaks between 1.2720eV and 1.2740eV. Under 2hυ excitation, the 1.2706eV peak is still the most prominent one, to the right of which the 1.2710eV peak is also discernible but not as strong as it is under 1hυ excitation. As for the satellite peaks, the 1.272eV, the 1.273eV, and the 1.274eV peak are observable above the noise level. Therefore, we successfully excite the SQD-in-cavity with 2hυ excitation, but a power dependent study was limited by the maximum laser power we could generate.

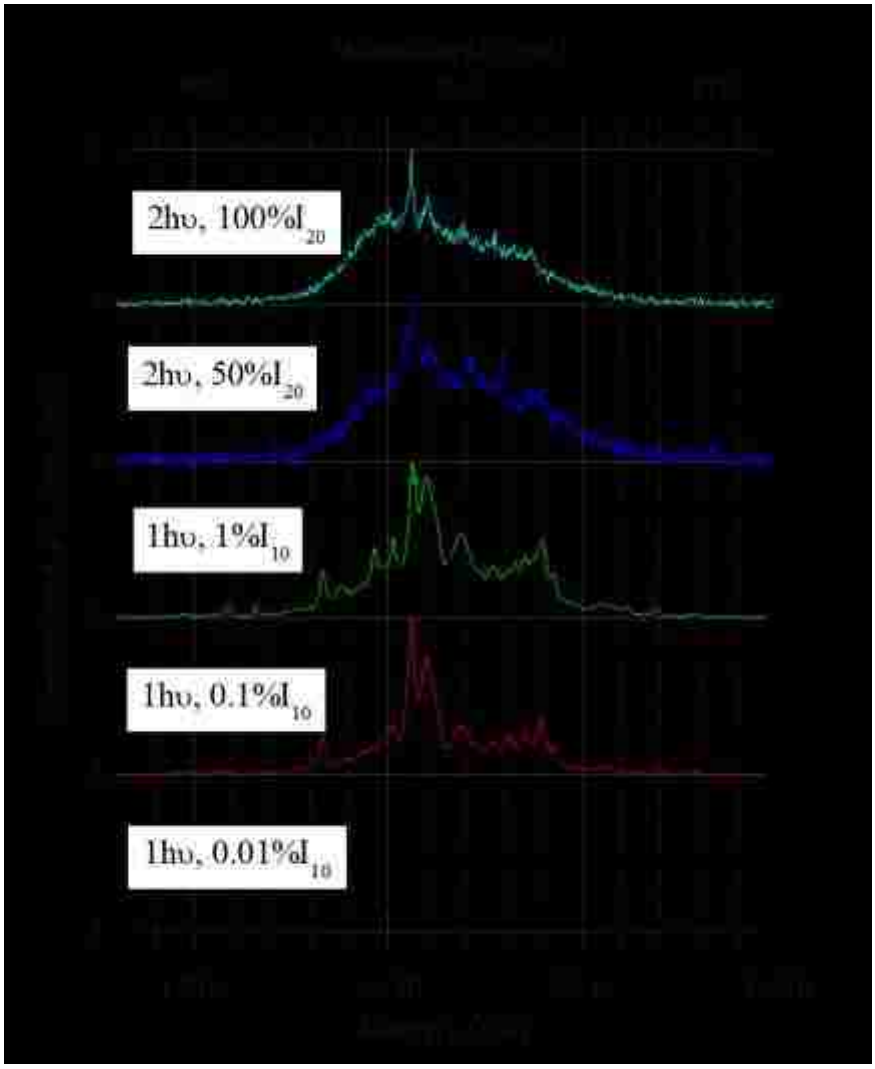

Figure 5.8. Normalized PL of SQD-in-cavity at various 2hυ and 1hυ excitation powers.

6 Conclusion and Outlook

In this dissertation, the PL behavior of InAs/GaAs QD samples was investigated under 1hυ and 2hυ excitation. Particularly, we examined the excitation power dependent PL of EQD and SQD, as well as SQD in a micro-cavity with 1hυ excitation. With 2hυ excitation, energy near half of the QDs ground state transition to half of the GaAs matrix bandgap was used to investigate the TPA in QDs. All the samples were grown by MBE and the morphology of these samples was characterized by AFM and TEM. A model was developed to explain the excitation power dependent PL intensity.

For EQD, a power law with power index of one was found for ground state transition with 1hυ excitation. Excitation energies at half of the QDs ground transition, 1st excited states transition, and the WL states transition are used to study the 2hυ excitation power dependent PL. A quadratic relationship between the integrated intensity and the excitation power indicates there is 2hυ process happening in the QDs system. PLE from half of the EQD's ground state transition to half of the GaAs matrix bandgap was performed, the result of which then confirms that there is direct 2hυ absorption in the QDs and WL when the 2hυ excitation energy is resonant with their levels. This serves as the first evidence of direct TPA induced PL of InAs QDs.

At SQD level, we identified a SQD with s, p, and d shells. The PL behavior of the X peak and X* peak of s and p shells with 1hυ and 2hυ excitation at various temperatures was discussed. With 1hυ excitation, the intensity of the X peak and X* peak of s and p shells all grow almost linearly with the excitation power at 5K. As temperature increases, the peaks redshift and broaden. The peak position as a function of temperature is described by Varshni Law [75]. The broadening of the PL peaks with increasing temperature can be explained by phonon broadening and photon broadening. With 2hυ excitation, we were able to observe SQD ground state

transition with excitation energy resonant with the SQD's excited state. This is the first evidence of 2hυ excited PL of a single InAs QD with near-bandgap excitation. However, the attempt at power dependent PL with 2hυ excitation was not successful since we could only distinguish the SQD PL within a very small excitation power range.

For SQD-in-cavity sample, we investigated its PL behavior at various excitation powers and various temperatures with 1hυ excitation. The linear relationship between the PL intensity and the excitation power at 10K reveals that the cavity effect on the SQD's PL is linear. As temperature increases, both the QD's PL and the cavity mode redshift. And the QD's PL shift more than the cavity mode. The PL peak position as a function of temperature still follows Varshni Law. With 2hυ excitation, we successfully observed SQD PL emitted from a cavity. But the SQD PL could not be observed when the excitation power is below half of the full power. So we could not do power dependent study with 2hυ excitation.

The prospective work may place emphasis on the QD-in-cavity sample. One of its applications is in the optical computing field. It has been demonstrated that a SQD in a micro-post cavity can serve as an efficient single photon source [34], [78], and an optical Kerr gate switch [79], [80]. Fabrication of such a micro-post sample after MBE growth employs electron beam lithography and dry etching [81]. Study of the TPA of such a micro-post sample will reveal more about its nonlinear optical property and may shine light on more possible applications.

Another interesting direction is to utilize QDs-in-cavity as a reflective optical limiter [45]. A typical absorptive optical limiter employs a nonlinear material which is transparent at low-intensity light and turns opaque at high-intensity light. The nonlinear material will absorb most of the high-intensity light which makes it easy to be damaged. On the other hand, we can put a nonlinear material between two DBRs to make a reflective optical limiter. When the light

intensity is low, it will transmit through the cavity mode. When the intensity becomes high, the nonlinear property of the material kicks in, destroying the cavity mode, turning the top DBR into a highly reflective mirror. To achieve such a sample, we need to add an etch-stopper structure [80] (for example, AlAs/$Al_{0.3}Ga_{0.7}As$ 5nm/232nm) during the MBE growth for removing the substrate. Then the cavity can be lifted off and we can test its transmission.

Reference

[1] J.-L. Zhu, Z.-Q. Li, J.-Z. Yu, K. Ohno, and Y. Kawazoe, "Size and shape effects of quantum dots on two-electron spectra," *Phys. Rev. B*, vol. 55, no. 23, pp. 15819–15823, 1997.

[2] Z. Li and X. Peng, "Size/shape-controlled synthesis of colloidal CdSe quantum disks: Ligand and temperature effects," *J. Am. Chem. Soc.*, vol. 133, no. 17, pp. 6578–6586, 2011.

[3] M. A. Reed, "Spatial quantization in GaAs–AlGaAs multiple quantum dots," *J. Vac. Sci. Technol. B Microelectron. Nanom. Struct.*, vol. 4, no. 1, p. 358, 1986.

[4] S. B. Brichkin and V. F. Razumov, "Colloidal quantum dots: synthesis, properties and applications," *Russ. Chem. Rev.*, vol. 85, no. 12, pp. 1297–1312, 2016.

[5] R. M. Sankaran, D. Holunga, R. C. Flagan, and K. P. Giapis, "Synthesis of blue luminescent Si nanoparticles using atmospheric-pressure microdischarges," *Nano Lett.*, vol. 5, no. 3, pp. 537–541, 2005.

[6] R. N. Pereira and A. J. Almeida, "Doped semiconductor nanoparticles synthesized in gas-phase plasmas," *J. Phys. D. Appl. Phys.*, vol. 48, no. 31, p. 314005, 2015.

[7] S. Maruo, O. Nakamura, and S. Kawata, "Three-dimensional microfabrication with two-photon-absorbed photopolymerization.," *Opt. Lett.*, vol. 22, no. 2, pp. 132–134, 1997.

[8] L. L. Erskine *et al.*, "Two-photon polymerization initiators for three- dimensional optical data storage and microfabrication," *Solid State Phys.*, vol. 398, no. March, pp. 51–54, 1999.

[9] G. S. He, T. C. Lin, P. N. Prasad, C. C. Cho, and L. J. Yu, "Optical power limiting and stabilization using a two-photon absorbing neat liquid crystal in isotropic phase," *Appl. Phys. Lett.*, vol. 82, no. 26, pp. 4717–4719, 2003.

[10] J. E. Ehrlich *et al.*, "Two-photon absorption and broadband optical limiting with bis-donor stilbenes," *Opt. Lett.*, vol. 22, no. 24, p. 1843, 1997.

[11] W. Denk, J. H. Strickler, and W. W. Webb, "Two-photon laser scanning fluorescence microscopy," *Science (80-.).*, vol. 248, no. 4951, p. 73 LP-76, Apr. 1990.

[12] L. a. Padilha *et al.*, "Frequency degenerate and nondegenerate two-photon absorption spectra of semiconductor quantum dots," *Phys. Rev. B - Condens. Matter Mater. Phys.*, vol. 75, no. 7, pp. 1–8, 2007.

[13] Y. Benny, Y. Kodriano, E. Poem, S. Khatsevitch, D. Gershoni, and P. M. Petroff, "Two-photon photoluminescence excitation spectroscopy of single quantum dots," *Phys. Rev. B*, vol. 84, no. 7, p. 75473, Aug. 2011.

[14] M. Scheibner, S. E. Economou, I. V. Ponomarev, C. Jennings, A. S. Bracker, and D. Gammon, “Two-photon absorption by a quantum dot pair,” *Phys. Rev. B*, vol. 92, no. 8, p. 81411, 2015.

[15] Q. Liu, B. D. Guo, Z. Y. Rao, B. H. Zhang, and J. R. Gong, “Strong Two-Photon-Induced Fluorescence from Photostable, Biocompatible Nitrogen-Doped Graphene Quantum Dots for Cellular and Deep-Tissue Imaging,” *Nano Lett.*, vol. 13, no. 6, pp. 2436–2441, 2013.

[16] L. Cao *et al.*, “Carbon Dots for Multiphoton Bioimaging Carbon Dots for Multiphoton Bioimaging,” *J. Am. Chem Soc.*, vol. 129, no. 37, pp. 11318–11319, 2007.

[17] A. Martí *et al.*, “Production of photocurrent due to intermediate-to-conduction-band transitions: A demonstration of a key operating principle of the intermediate-band solar cell,” *Phys. Rev. Lett.*, vol. 97, no. 24, pp. 1–4, 2006.

[18] A. Scaccabarozzi, S. Adorno, S. Bietti, M. Acciarri, and S. Sanguinetti, “Evidence of two-photon absorption in strain-free quantum dot GaAs/AlGaAs solar cells,” *Phys. Status Solidi - Rapid Res. Lett.*, vol. 7, no. 3, pp. 173–176, 2013.

[19] R. Tamaki, Y. Shoji, Y. Okada, and K. Miyano, “Spectrally resolved intraband transitions on two-step photon absorption in InGaAs/GaAs quantum dot solar cell,” *Appl. Phys. Lett.*, vol. 105, no. 7, pp. 1–5, 2014.

[20] G. S. He, Q. Zheng, K. T. Yong, A. I. Ryasnyanskiy, P. N. Prasad, and A. Urbas, “Two-photon absorption based optical limiting and stabilization by using a CdTe quantum dot solution excited at optical communication wavelength of ~ 1300 nm,” *Appl. Phys. Lett.*, vol. 90, no. 18, pp. 6–9, 2007.

[21] T. Moldaschl, W. Parz, T. Müller, S. Golka, G. Strasser, and K. Unterrainer, “Two-photon spectral hole burning spectroscopy of InAs/GaAs quantum dots,” *Appl. Phys. Lett.*, vol. 97, no. 2010, p. 11903, 2010.

[22] S. J. Boyle, A. J. Ramsay, A. M. Fox, and M. S. Skolnick, “Two-color two-photon Rabi oscillation of biexciton in single InAs/GaAs quantum dot,” in *Physica E: Low-Dimensional Systems and Nanostructures*, 2010, vol. 42, no. 10, pp. 2485–2488.

[23] P. P. Paskov, P. O. Holtz, B. Monemar, J. M. Garcia, W. V. Schoenfeld, and P. M. Petroff, “Photoluminescence up-conversion in InAs/GaAs self-assembled quantum dots,” *Appl. Phys. Lett.*, vol. 77, no. 6, p. 812, 2000.

[24] C. Kammerer, G. Cassabois, C. Voisin, C. Delalande, P. Roussignol, and J. M. Gérard, “Photoluminescence Up-Conversion in Single Self-Assembled InAs/GaAs Quantum Dots,” *Phys. Rev. Lett.*, vol. 87, no. 20, p. 207401, 2001.

[25] H. Oda, a. Yamanaka, N. Ozaki, N. Ikeda, and Y. Sugimoto, “Enhancement upconversion luminescence in InAs-quantum dots embedded GaAs photonic-crystal slab line-defect waveguide,” *2013 Conf. Lasers Electro-Optics Eur. Int. Quantum Electron. Conf. CLEO/Europe-IQEC 2013*, vol. 1, no. Cd, p. 8655, 2013.

[26] J. Phillips, K. Kamath, X. Zhou, N. Chervela, and P. Bhattacharya, “Photoluminescence and far-infrared absorption in Si-doped self-organized InAs quantum dots,” *Appl. Phys. Lett.*, vol. 71, no. 15, p. 2079, 1997.

[27] P. Aivaliotis, E. A. Zibik, L. R. Wilson, J. W. Cockburn, M. Hopkinson, and N. Q. Vinh, “Two photon absorption in quantum dot-in-a-well infrared photodetectors,” *Appl. Phys. Lett.*, vol. 92, no. 2, pp. 2006–2009, 2008.

[28] C. Gautham, D. W. Snoke, a. Rastelli, and O. G. Schmidt, “Time-resolved two-photon excitation of dark states in quantum dots,” *Appl. Phys. Lett.*, vol. 104, no. 14, p. 143114, Apr. 2014.

[29] T. Li and M. Dagenais, “Non-resonant below-bandgap two-photon absorption in quantum dot solar cells,” *Appl. Phys. Lett.*, vol. 106, no. 17, p. 171101, 2015.

[30] T. Nozawa, H. Takagi, K. Watanabe, and Y. Arakawa, “Direct Observation of Two-Step Photon Absorption in an InAs/GaAs Single Quantum Dot for the Operation of Intermediate-Band Solar Cells,” *Nano Lett.*, vol. 15, no. 7, pp. 4483–4487, 2015.

[31] A. F. Jarjour, T. J. Parker, R. A. Taylor, R. W. Martin, and I. M. Watson, “Two-photon absorption in single site-controlled InGaN/GaN quantum dots,” *Phys. Status Solidi C Conf.*, vol. 2, no. 11, pp. 3843–3846, 2005.

[32] D. Collins *et al.*, “Two-photon autocorrelation measurements on a single InGaN/GaN quantum dot.,” *Nanotechnology*, vol. 20, p. 245702, 2009.

[33] R. Bardoux, M. Funato, A. Kaneta, Y. Kawakami, A. Kikuchi, and K. Kishino, “Two-photon absorption induced anti-Stokes emission in single InGaN/GAN quantum-dot-like objects,” *Phys. Status Solidi - Rapid Res. Lett.*, vol. 7, no. 5, pp. 344–347, 2013.

[34] G. Solomon, M. Pelton, and Y. Yamamoto, “Single-mode Spontaneous Emission from a Single Quantum Dot in a Three-Dimensional Microcavity,” *Phys. Rev. Lett.*, vol. 86, no. 17, pp. 3903–3906, Apr. 2001.

[35] J. Gérard, B. Sermage, B. Gayral, B. Legrand, E. Costard, and V. Thierry-Mieg, “Enhanced Spontaneous Emission by Quantum Boxes in a Monolithic Optical Microcavity,” *Phys. Rev. Lett.*, vol. 81, no. 5, pp. 1110–1113, 1998.

[36] J. R. Arthur, “Interaction of Ga and As2 molecular beams with GaAs surfaces,” *J. Appl. Phys.*, vol. 39, no. 8, pp. 4032–4034, 1968.

[37] A. Y. Cho, “Epitaxial growth of gallium phosphide on cleaved and polished (111) calcium fluoride,” *J. Appl. Phys.*, vol. 41, no. 2, pp. 782–786, 1970.

[38] S. Franchi, G. Trevisi, L. Seravalli, and P. Frigeri, “Quantum dot nanostructures and molecular beam epitaxy,” *Prog. Cryst. Growth Charact. Mater.*, vol. 47, no. 2–3, pp. 166–195, 2003.

[39] Z. Y. AbuWaar, E. Marega Jr, M. Mortazavi, and G. J. Salamo, “In situ photoluminescence study of uncapped InAs/GaAs quantum dots,” *Nanotechnology*, vol. 19, no. 33, p. 335712, 2008.

[40] P. B. Joyce, T. J. Krzyzewski, G. R. Bell, T. S. Jones, E. C. Le Ru, and R. Murray, “Optimizing the growth of 1.3 μm InAs/GaAs quantum dots,” *Phys. Rev. B*, vol. 64, no. 23, p. 235317, 2001.

[41] M. J. Da Silva, A. A. Quivy, S. Martini, T. E. Lamas, E. C. F. Da Silva, and J. R. Leite, “Large InAs/GaAs quantum dots with an optical response in the long-wavelength region,” *J. Cryst. Growth*, vol. 278, no. 1–4, pp. 103–107, 2005.

[42] B. Ilahi *et al.*, “Toward long wavelength low density InAs / GaAs quantum dots,” *Phys. Lett. A*, vol. 357, no. October 2015, pp. 360–363, 2006.

[43] V. I. Trofimov, H. S. Park, and J.-I. Kim, “Growth and optical properties of InAs/GaAs quantum dot structures,” *Appl. Surf. Sci.*, vol. 226, no. 1–3, pp. 45–51, 2004.

[44] N. K. Cho, S. P. Ryu, J. D. Song, W. J. Choi, J. I. Lee, and H. Jeon, “Comparison of structural and optical properties of InAs quantum dots grown by migration-enhanced molecular-beam epitaxy and conventional molecular-beam epitaxy,” *Appl. Phys. Lett.*, vol. 88, no. 13, pp. 13–16, 2006.

[45] J. H. Vella *et al.*, “Experimental Realization of a Reflective Optical Limiter,” *Phys. Rev. Appl.*, vol. 5, no. 6, pp. 1–7, 2016.

[46] P. L. Gourley, T. J. Drummond, and B. L. Doyle, “Dislocation filtering in semiconductor superlattices with lattice-matched and lattice-mismatched layer materials,” *Appl. Phys. Lett.*, vol. 49, no. 17, pp. 1101–1103, 1986.

[47] E. C. Le Ru, J. Fack, and R. Murray, “Temperature and excitation density dependence of the photoluminescence from annealed InAs/GaAs quantum dots,” *Phys. Rev. B*, vol. 67, no. 24, p. 245318, 2003.

[48] W. Yang, R. Lowe-Webb, H. Lee, and P. Sercel, “Effect of carrier emission and retrapping on luminescence time decays in InAs/GaAs quantum dots,” *Phys. Rev. B*, vol. 56, no. 20, pp. 13314–13320, 1997.

[49] K. W. Sun, J. W. Chen, B. C. Lee, C. P. Lee, and a M. Kechiantz, “Carrier capture and relaxation in InAs quantum dots,” *Nanotechnology*, vol. 16, no. 9, pp. 1530–1535, Sep. 2005.

[50] D. Morris, N. Perret, and S. Fafard, “Carrier energy relaxation by means of Auger processes in InAs/GaAs self-assembled quantum dots,” *Appl. Phys. Lett.*, vol. 75, no. 23, pp. 3593–3595, 1999.

[51] B. Ohnesorge, M. Albrecht, J. Oshinowo, A. Forchel, and Y. Arakawa, “Rapid carrier relaxation in self-assembled InxGa1-xAs/GaAs quantum dots.,” *Phys. Rev. B. Condens.*

Matter, vol. 54, no. 16, pp. 11532–11538, 1996.

[52] R. Heitz *et al.*, "Energy relaxation by multiphonon processes in InAs/GaAs quantum dots," *Phys. Rev. B*, vol. 56, no. 16, pp. 10435–10445, 1997.

[53] T. Inoshita and H. Sakaki, "Electron relaxation in a quantum dot: Significance of multiphonon processes," *Phys. Rev. B*, vol. 46, no. 11, pp. 7260–7263, 1992.

[54] K. Schmidt, G. Medeiros-Ribeiro, M. Oestreich, P. Petroff, and G. Döhler, "Carrier relaxation and electronic structure in InAs self-assembled quantum dots.," *Phys. Rev. B. Condens. Matter*, vol. 54, no. 16, pp. 11346–11353, Oct. 1996.

[55] P. C. Sercel, "Multiphonon-assisted tunneling through deep levels: A rapid energy-relaxation mechanism in nonideal quantum-dot heterostructures," *Phys. Rev. B*, vol. 51, no. 20, pp. 14532–14541, 1995.

[56] J. Finley *et al.*, "Charged and neutral exciton complexes in individual self-assembled In(Ga)As quantum dots," *Phys. Rev. B*, vol. 63, no. 7, p. 73307, Jan. 2001.

[57] K. Hinzer *et al.*, "Optical spectroscopy of a single Al0.36In0.64As/Al0.33Ga0.67As quantum dot," *Phys. Rev. B*, vol. 63, no. 7, p. 75314, Jan. 2001.

[58] R. Vaxenburg, A. Rodina, A. Shabaev, E. Lifshitz, and A. L. Efros, "Nonradiative auger recombination in semiconductor nanocrystals," *Nano Lett.*, vol. 15, no. 3, pp. 2092–2098, 2015.

[59] J. E. Fouquet and a. E. Siegman, "Room-temperature photoluminescence times in a GaAs/Al(x)Ga(1−x)As molecular beam epitaxy multiple quantum well structure," *Appl. Phys. Lett.*, vol. 46, no. 3, p. 280, 1985.

[60] S. Sanguinetti *et al.*, "Carrier thermodynamics in InAs/In(x)Ga(1-x)As quantum dots," *Phys. Rev. B*, vol. 74, no. 20, p. 205302, 2006.

[61] A. C. Bleszynski, F. A. Zwanenburg, R. M. Westervelt, A. L. Roest, E. P. A. M. Bakkers, and L. P. Kouwenhoven, "Scanned probe imaging of quantum dots inside InAs nanowires," *Nano Lett.*, vol. 7, no. 9, pp. 2559–2562, 2007.

[62] R. W. Boyd, *Nonlinear Optics*, 3rd ed. 2008.

[63] M. Born and E. Wolf, *Principles of Optics*, 6th ed. 1980.

[64] C. J. R. Sheppard, "Approximate calculation of the reflection coefficient from a stratified medium," *Pure Appl. Opt. J. Eur. Opt. Soc. Part A*, vol. 4, no. 5, pp. 665–669, 1995.

[65] E. J. Johnson, J. Kafalas, R. W. Davies, and W. a. Dyes, "Deep center EL2 and anti-Stokes luminescence in semi-insulating GaAs," *Appl. Phys. Lett.*, vol. 40, no. 11, pp. 993–995, 1982.

[66] L. G. Quagliano and H. Nather, “Up conversion of luminescence via deep centers in high purity GaAs and GaAlAs epitaxial layers,” *Appl. Phys. Lett.*, vol. 45, no. 5, pp. 555–557, 1984.

[67] M. D. Sturge, “Optical absorption of gallium arsenide between 0.6 and 2.75 eV,” *Phys. Rev.*, vol. 127, no. 3, pp. 768–773, 1962.

[68] M. E. Ware *et al.*, “Polarized Fine Structure in the Photoluminescence Excitation Spectrum of a Negatively Charged Quantum Dot,” *Phys. Rev. Lett.*, vol. 95, no. 17, p. 177403, Oct. 2005.

[69] Y. Benny, Y. Kodriano, E. Poem, D. Gershoni, T. a. Truong, and P. M. Petroff, “Excitation spectroscopy of single quantum dots at tunable positive, neutral, and negative charge states,” *Phys. Rev. B - Condens. Matter Mater. Phys.*, vol. 86, no. 8, p. 85306, Aug. 2012.

[70] M. Zielinski *et al.*, “Excitonic complexes in natural InAs/GaAs quantum dots,” *Phys. Rev. B - Condens. Matter Mater. Phys.*, vol. 91, no. 8, pp. 1–6, 2015.

[71] R. Thompson *et al.*, “Single-photon emission from exciton complexes in individual quantum dots,” *Phys. Rev. B*, vol. 64, no. 20, p. 201302, Oct. 2001.

[72] Y.-J. Yu, W. Jhe, and Y. Arakawa, “High-resolution near-field spectroscopy of InAs single quantum dots at 70 K,” *Appl. Phys. Lett.*, vol. 83, no. 15, p. 3024, 2003.

[73] C. Kammerer *et al.*, “Efficient acoustic phonon broadening in single self-assembled InAs/GaAs quantum dots,” *Phys. Rev. B*, vol. 65, no. 3, pp. 1–4, 2001.

[74] P. Borri, W. Langbein, J. Hvam, and F. Martelli, “Well-width dependence of exciton-phonon scattering in InxGa1-xAs/GaAs single quantum wells,” *Phys. Rev. B*, vol. 59, no. 3, p. 2215, 1999.

[75] Y. P. Varshni, “Temperature dependence of the energy gap in semiconductors,” *Physica*, vol. 34, no. 1, pp. 149–154, 1967.

[76] D. Xiu-Ming, S. Bao-Quan, X. Yong-Hua, H. She-Song, N. Hai-Qiao, and N. Zhi-Chuan, “Temperature Dependence of Photoluminescence from Single and Ensemble InAs/GaAs Quantum Dots,” *Chinese Phys. Lett.*, vol. 25, no. 9, pp. 3440–3443, 2008.

[77] E. M. Purcell, “Spontaneous Emission Probabliities at Radio Frquencies,” *Phys. Rev.*, vol. 69, pp. 674–674, 1946.

[78] M. Pelton *et al.*, “An efficient source of single photons: A single quantum dot in a micropost microcavity,” *Phys. E Low-Dimensional Syst. Nanostructures*, vol. 17, no. 1–4, pp. 564–567, Nov. 2003.

[79] K. Morita, T. Takahashi, T. Kitada, and T. Isu, “Enhanced Optical Kerr Signal of GaAs/AlAs Multilayer Cavity with InAs Quantum Dots Embedded in Strain-Relaxed

Barriers," 2009.

[80] T. Takahashi, T. Mukai, K. Morita, T. Kitada, and T. Isu, "GaAs/AlAs multilayer cavity with InAs quantum dots embedded in strain-relaxed barriers for planar-type optical Kerr gate switches," *Jpn. J. Appl. Phys.*, vol. 49, no. 4 PART 2, 2010.

[81] B. Zhang *et al.*, "Fabrication of InAs quantum dots in AlAs/GaAs DBR pillar microcavities for single photon sources," *J. Appl. Phys.*, vol. 97, no. 7, p. 73507, 2005.

Appendix

A. Molecular Beam Epitaxy

A typical MBE growth chamber is shown in Figure A.1 [A1]. Each part in the figure will be briefly introduced below. An effusion cell is a crucible, usually made of pyrolytic boron nitride for low gas evolution and good chemical stability even at high temperature, with filaments around and thermocouple attached. High purity source material placed inside of the crucible evaporates when the crucible is heated up. The flux of the material can be finely controlled by changing the crucible temperature. Each cell has its own mechanical shutter in front to realize abrupt modulation of flux. Reflection high-energy electron diffraction (RHEED)

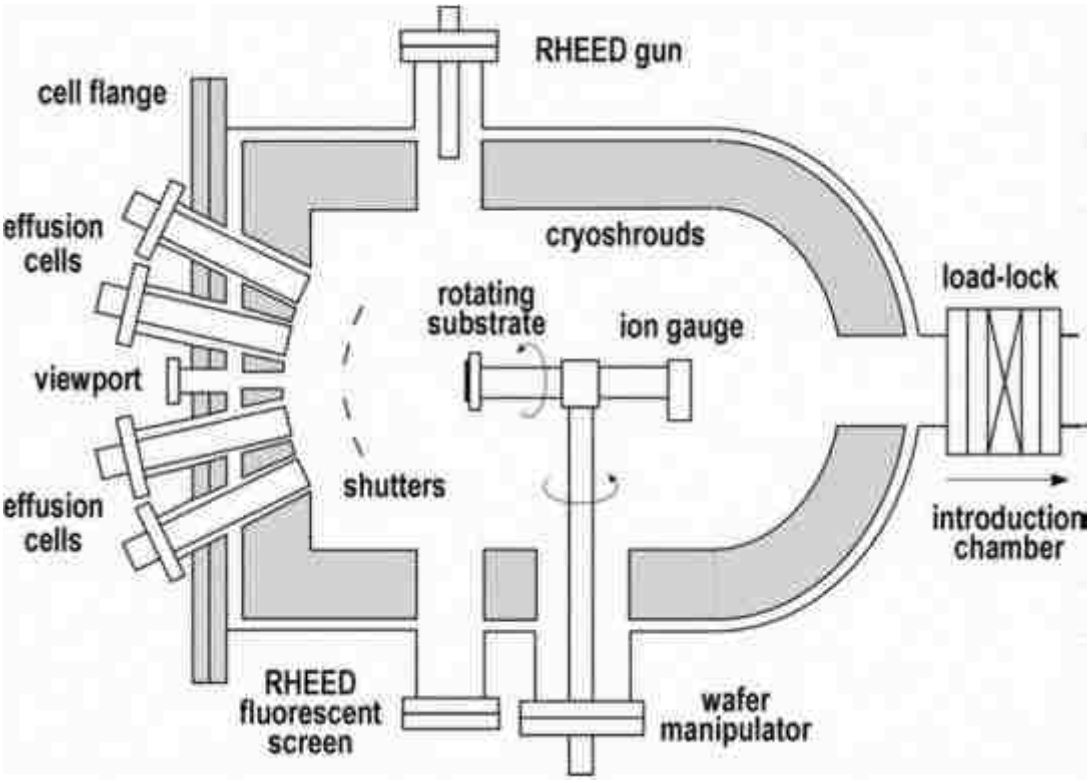

Figure A.1. Schematic diagram of a typical MBE growth chamber (top view) [A1].

gun shoots high-energy electron beam onto the substrate at a very shallow angle, and the

RHEED fluorescent screen collects the reflected electron beam which forms a diffractive pattern after interacts with the substrate surface. This gives us the growth dynamics *in-situ* and helps us to monitor the growth. The wafer manipulator can be turned and fixed at certain position to control the substrate holder to face certain directions. While loading and un-loading the substrate, we turn the manipulator to the "load position" (substrate holder facing the introduction chamber), so that an arm can come through the gate valve and grab the substrate. After loading the substrate, we will turn the manipulator to the "growth position" so that the substrate is facing the effusion cells. An ion gauge is also attached to the manipulator to measure flux at the substrate surface from each cell when the manipulator is turned to the "gauge position". Cryoshrouds are equipped

Figure A.2. Photo of Riber 32P MBE (taken by author).

all around the MBE chamber and are usually filled with high grade liquid nitrogen before and during the growth. They act as cold traps for background residual vapor to ensure an ultra-high

vacuum (UHV) environment inside of the chamber in addition to a multi-stage pumping system. This is important because the atomic or molecular beams from the source materials need to reach the substrate surface efficiently without collisions. UHV is also a precondition for low impurity crystal growth. The MBE growth chamber usually connects to an introduction (preparation) chamber and a load-lock. The load-lock is regularly vented for loading and unloading. The introduction chamber is for degas wafers before it enters the growth chamber.

The MBE we used in this project is a Riber 32P system. A picture of the system is shown in Figure A.2. It is equipped with one arsenic cell, two gallium cells, one indium cell, one aluminum cell, one silicone cell and one beryllium cell. The silicone cell and beryllium cell are for doping purpose, which is not used in this project.

[A1] M. Henini, *Molecular Beam Epitaxy: From Research to Mass Production*, 1st ed. Elsevier Science, 2012

B. AFM Characterization

The morphology of QDs are investigated with AFM first. AFM is a type of scanning probe microscopy, in which a mechanical probe is used to scan the sample surface and gather information, e.g. the atomic force between the probe and sample, about the surface morphology with a vertical resolution less than 1nm. Invented by G.Binning in the 1980s [B1], AFM has been widely utilized in different disciplines, including semiconductor technology, molecular biology and so on.

The QDs samples are characterized with AFM under tapping mode. Figure B.1 shows the

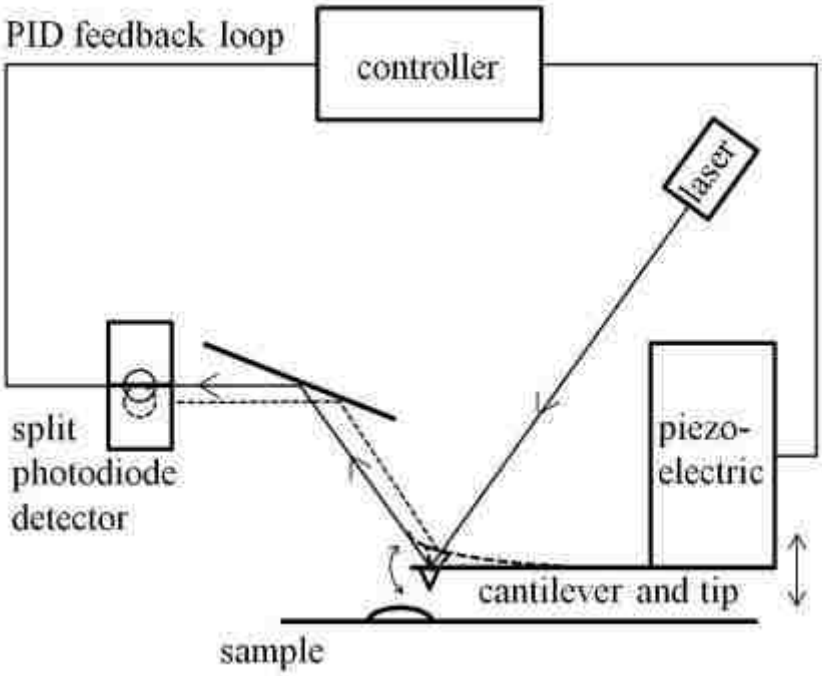

Figure B.1. Basic AFM tapping mode working principal.

schematic of the basic AFM working principal under tapping mode. Before engaging with the sample surface, the cantilever and tip is driven at or near its resonant frequency by a piezoelectric crystal. This causes the cantilever and tip to oscillate with certain amplitude. A laser beam is reflected by the cantilever and then collected by a split photodiode detector

consisting of two closed spaced photodiodes. When the cantilever and tip is not engaged with the sample surface, the laser signal is oscillating evenly between the two photodiodes, resulting in both photodiodes collecting same amount of signal. The cantilever is then moved towards the sample surface until the tip starts to tap the surface. Due to this contact with surface, oscillation amplitude of the cantilever is reduced. This change in amplitude deflects the laser beam, resulting in different signal collected by the two photodiodes. This difference is then sent through a proportional-integral-derivative (PID) feedback loop, which control the vertical position of the cantilever to maintain constant oscillation amplitude. During a lateral scan, this vertical position is collected as sample surface features.

The AFM we used in this project is Veeco Dimension V under ambient conditions as shown in Figure B.2.

Figure B.2. Photo of Veeco Dimension V AFM (taken by author).

All samples are characterized with AFM after growth to see the morphology of QDs. Figure B.3(a) shows the AFM image of sample SF044 with 2.0 MLs deposition of InAs at a rate of 0.075ML/s and no manipulator tile. From this AFM image we can tell that the QDs are uniformly distributed on the surface and the density is about $100\mu m^{-2}$. But size of the QDs is not uniform. Cross-section of some QDs, shown in Figure B.3(b), shows the profile of those QDs: the QDs have a lens shape in general; the big QDs (blue line) are about 40nm in diameter and 7nm in height; the small QDs (red line) are about 25nm in diameter and about 3nm in height;

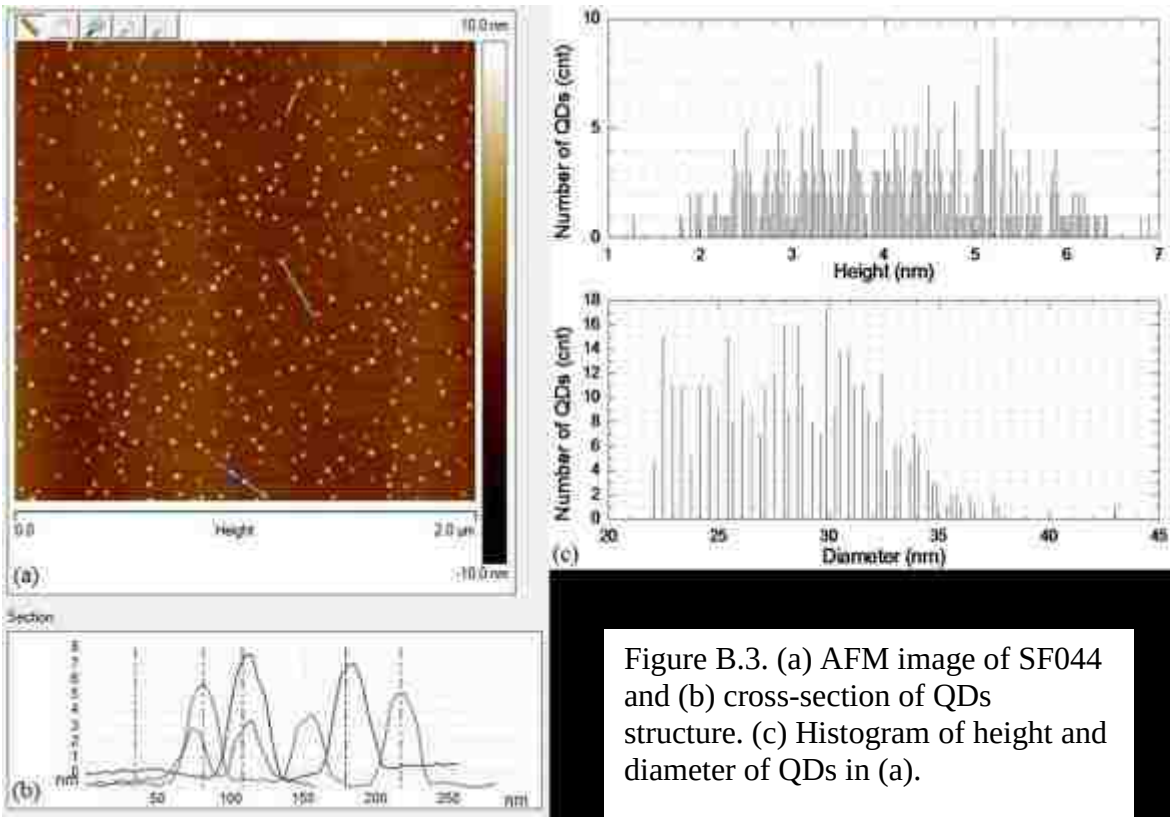

Figure B.3. (a) AFM image of SF044 and (b) cross-section of QDs structure. (c) Histogram of height and diameter of QDs in (a).

there are also QDs with size in between (green line). Histogram of the height and diameter of the QDs are shown in Figure B.3(c). Since the height of QDs is much smaller than its diameter, quantum confinement effect is much stronger in the vertical direction than in lateral. Thus, the height plays a more significant role in determining the QD's energy level, which will be reflected in the QD's PL energy. Therefore we focus more on the distribution of QDs height other than

diameter when anticipating their PL. From the height histogram shown in Figure B.3(c), we can see it is a bi-distribution centered at 3nm and 5nm. This results in a non-Gaussian PL as we will see later on.

With the same deposition amount and rate, we tilted the manipulator by 5° to grow sample SF046. Because of the tilted manipulator, we observed a gradient density of QDs formation. AFM image of this sample at three different positions along the indium flux is shown

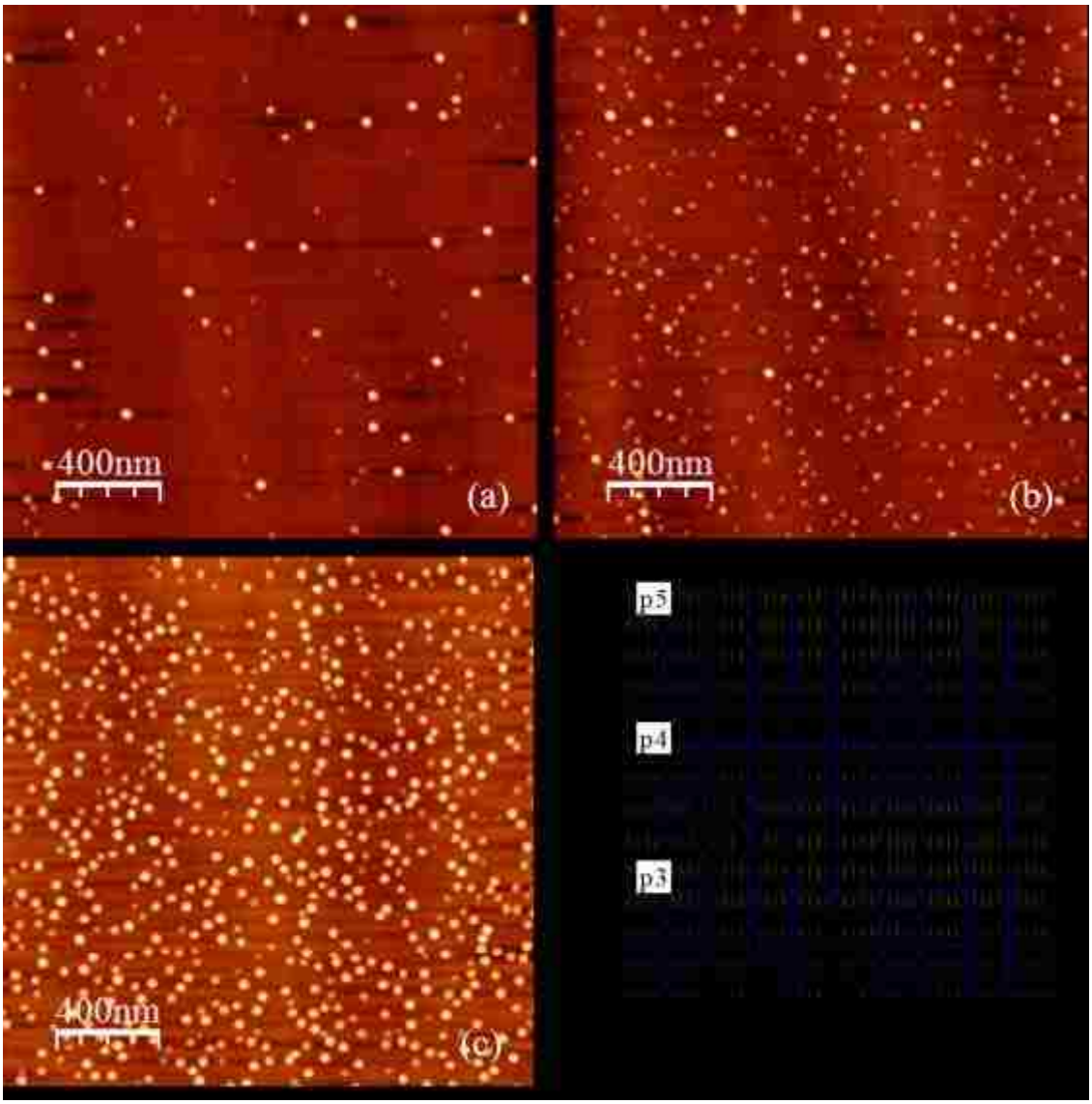

Figure B.4. AFM image of SF046 at (a) p5, (b) p4, (c) p3. (d) Height histogram of QDs at these three positions.

in Figure B.4: (a) position 5 (p5), (b) position 4 (p4) and (c) position 3 (p3). QDs density for each position is: p5 – 19/μm^2, p4 – 77/μm^2, and p3 – 146/μm^2 respectively. Figure B.4(d) shows the height histogram of QDs at these three positions. At p5, the low density region, QDs have a bi-size distribution with small dots around 2nm in height and big dots around 7nm in height. The density of QD smaller than 5nm and bigger than 5nm are both about 9/μm^2. At p4, the medium density region, much more small dots with height between 2nm and 3nm are formed. 93% of the QDs have height smaller than 5nm, while the rest has a quite uniform distribution ranging from 5nm to 8nm. At p3, the high density region, 64% of the QDs have height bigger than 3.5nm and they have a Gaussian distribution centered at 5.1nm. The rest has a quite uniform distribution from 1.5nm to 3.5nm. With this sample we learnt that the density of QDs can be controlled over one order of magnitude by tilting the manipulator for 5°. But the lowest density achieved with this sample is still too high for single QD PL. We then grew samples with less indium deposition amount as well as lower deposition rate to achieve lower QDs density.

[B1] G. Binnig and C. F. Quate, “Atomic Force Microscope,” Phys. Rev. Lett., vol. 56, no. 9, pp. 930–933, 1986.

C. TEM Characterization

Transmission electron microscope (TEM) was first demonstrated by Ernst Ruska and Max Knoll in 1931. Using a beam of electrons as its illumination source, TEM can achieve a significantly higher resolution than light microscope. Continuous development and refinement of the design and construction has made TEM a very popular technique in many disciplines, including material science, geology, biology, and medical science.

The TEM we used is FEI Titan high resolution TEM. Figure C.1 shows its simplified schematics. Electrons come out of a field emission gun with high energy (80-300keV). This electron beam goes through a series of electro-magnetic lenses before it reaches the specimen. Condenser lens 1 controls the crossover point of the beam before condenser lens 2. The strength of condenser lens 1 determines the probe size in scanning TEM mode. The combination of condenser lens 2 and its aperture affects the intensity of the beam and the size of the illumination area. The objective lens creates image of the specimen after the electron

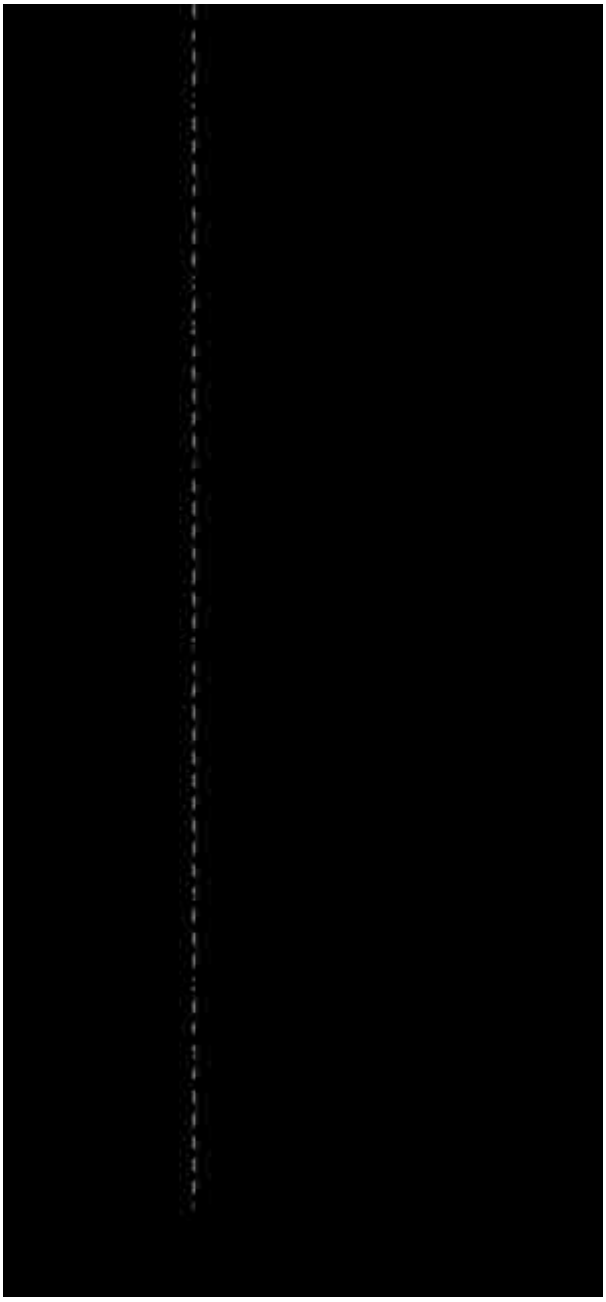

Figure C.1. Simplified schematics of TEM.

beam goes through it. Intermediate lens is used to switch between imaging mode and diffraction mode. In diffraction mode, we can view the reciprocal lattice of a crystal specimen and rotate the specimen to certain angle. This is important if we want to get high resolution image since the atoms need to align along the beam axis so that the image of each atom column does not interfere with each other. Projector lens magnifies the image and project it on the phosphor screen. A picture of the Titan TEM is shown in Figure C.2.

Figure C.2. Photo of Titan TEM (taken by author).

The specimen for TEM measurement needs to be extremely thin for the electron beam to go through. The region of view is typically less than 100nm thick. So a piece of crystal sample needs to be mechanically polished and then ion milled to have some thin areas for investigation. The diameter of the sample needs to be less than 3mm to fit into the sample holder. A solid material specimen can also be cut and polished by focused ion beam in a scanning electron microscope environment.

D. PL & PLE Measurement Setup

Photoluminescence is light emission from a material after photoexcitation. Figure D.1 presents the schematics of the Horiba LabRAM HR800 system that we used for our PL and PLE measurement. The system has two input options: a He-Ne laser comes with the system, and another aperture for any external light source. These two excitation beams are switched by a flip mirror. The excitation beam then goes through a neutral density filter wheel, consisting of six

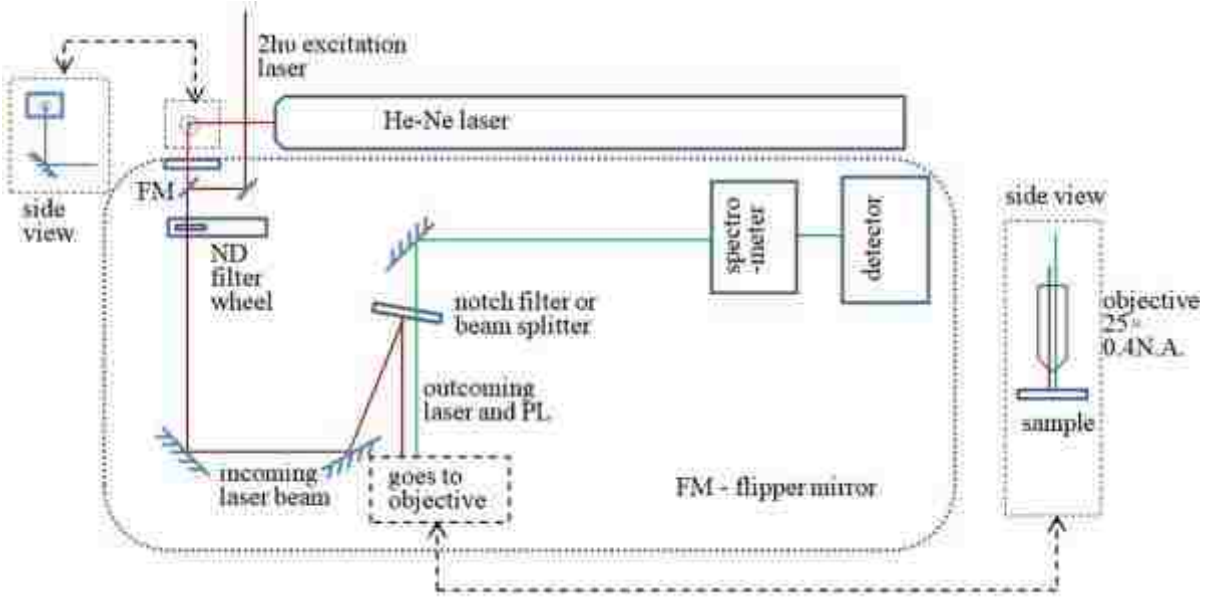

Figure D.1. Schematic of Horiba LabRAM HR800 system.

neutral density filters: OD(optical density)0.3, OD0.6, OD1, OD2, OD3, OD4. Optical density is the value of the logarithm with base 10 of the power transmission factor:

$$\mathrm{OD} = -\log_{10}\frac{P_{out}}{P_{in}}.$$

Therefore, the excitation power can be varied by inserting different neutral density filter in the beam path. The excitation beam then reflected by a couple of mirrors and a notch filter at the laser wavelength or a beam splitter before going into the objective, which focus the excitation

onto the sample. For below room temperature measurement, the sample is kept in a cryo-stat with liquid nitrogen or liquid helium flow and a heat to control the temperature. The cryo-stat is fixed on top of a motor stage to move in plane. Reflected laser and the PL from sample are collected by the same objective. They are then directed into a spectrometer and a detector. The spectrometer has a single diffraction grating which can be chosen from 150grooves/mm, 3000grooves/mm, 600grooves/mm, 1200grooves/mm, 1800grooves/mm. The higher the number, the higher the spectral resolution but shorter detection range. In general, we used the

Figure D.2. Photo of Horiba LabRAM HR800 system (taken by author).

150grooves/mm for EQDs PL and the 1200grooves/mm. There are three options for detectors: an electrical-cooled Si-CCD, a liquid nitrogen cooled InGaAs array, and a liquid nitrogen cooled single channel InGaAs detector. Each detector is designated for a wavelength range: Si-CCD for 1.1μm and below, InGaAs array for 1.1-1.5μm, and single channel InGaAs for 1.5-2.2μm. A picture of this system is shown in Figure D.2.

For PLE measurement, same setup is used. But instead of a fix excitation wavelength, the excitation laser is tuned through a wavelength range. And a fixed wavelength on the emission spectrum is monitored through this excitation range.

E. Two-photon Excitation Source System

The schematics of the 2hυ excitation source system is shown in Figure E.1. The system uses a Vitesse 800-2 as a seed laser, the output of which is 100fs pulses with a repetition rate of 80MHz at a wavelength of 800nm. The pulses go through a pulse stretcher first to have their peak power reduced to avoid destructing optical elements in the amplifier followed. Then the stretched pulses enter RegA 9050 amplifier, which uses the energy from a Verdi V-10 pump laser. The amplified pulses then go back to a pulse compressor to be recompressed to duration similar to their original. After the pulse compressor, the pulses enter an optical parametric amplifier (OPA) – OPA9850. It converts the 800nm input into two beams, signal and idler, the sum energy of which equals to the input. We define the idler beam as the beam ranging from 1.2μm to 1.6μm, and the signal beam as the beam ranging from 1.6μm to 2.4μm. A specific wavelength can be chosen by meeting the phase-matching condition of the OPA crystal (barium borate material). At the output of this OPA, long pass filter at 1050nm is put to block the visible light generated in the OPA. Long pass filter at 1550nm is put to block the idler beam.

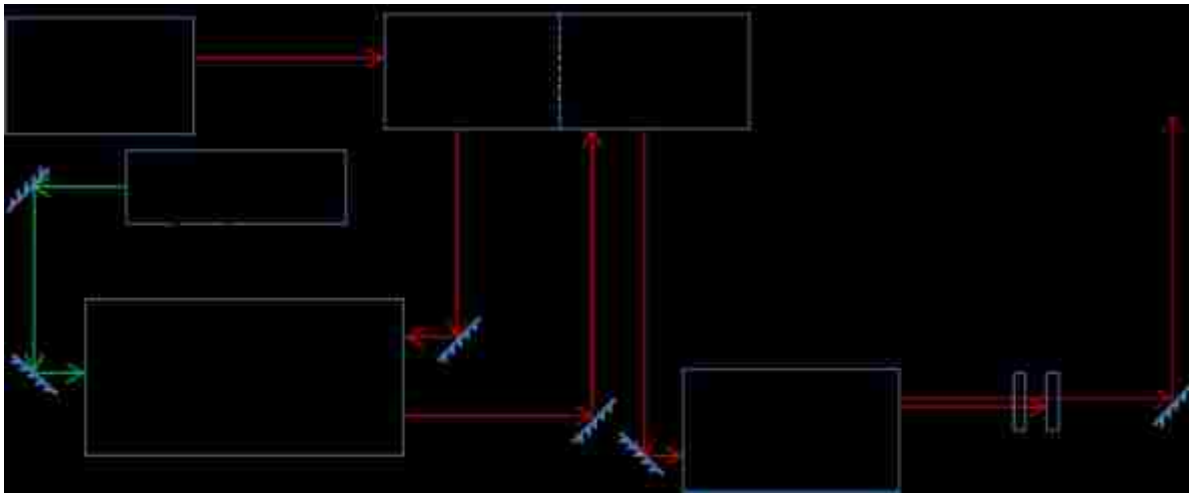

Figure E.1.Two-photon excitation laser system.

Figure E.2 is the spectra of the 2hυ excitation used in this research. Each spectrum corresponds to one OPA crystal angle. The intensity is kept at the same level by a gradient neutral density filter. As we can see the spectrum is in a good Gaussian shape at most of the wavelength. At some wavelength, the output is not that clean and have satellite peaks. The output has an average FWHM about 29.3meV, quite broad comparing with continuous-wave laser. Below 0.60eV, the output intensity of the laser becomes too small to excite the sample. Above 0.77eV, the higher energy side is cut off by the 1550nm long pass filter.

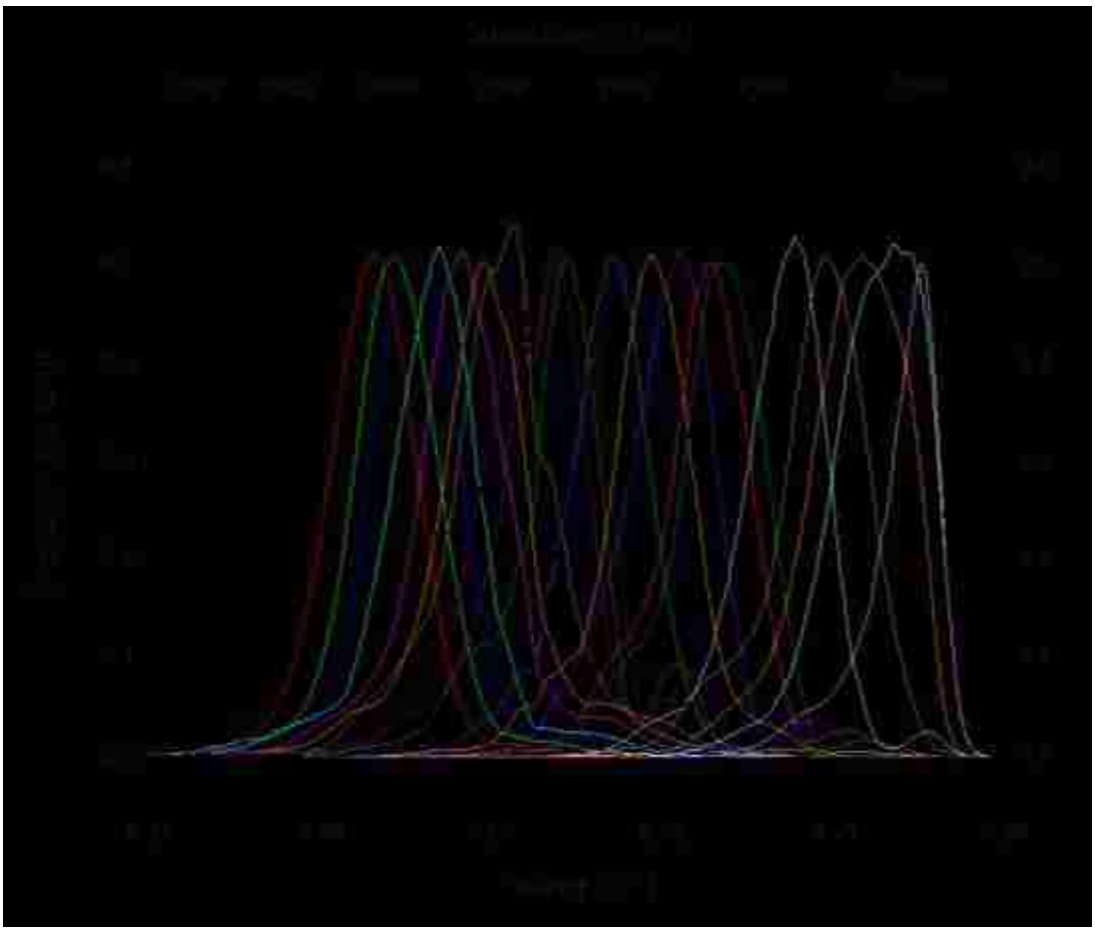

Figure E.2. Spectra of the 2hυ excitation laser.

F. Publication list

Publication related to dissertation research:

1. X. Hu, D. Guzun, M. E. Ware, Y. I. Mazur, and G. J. Salamo, "Two-photon Absorption Induced Emission of InAs/GaAs Quantum Dots", in Frontiers in Optics 2016, OSA Technical Digest (online) (Optical Society of America, 2016), paper JW4A.175.

2. In preparation, "Near Bandgap Two-photon Absorption Induced Photoluminescence of InAs/GaAs Quantum Dots", X. Hu, D. Guzun, M. E. Ware, Yu. I. Mazur, and G. J. Salamo.

Other publications:

3. Nanoscale Res. Lett., 12(1), 488 (2017), "Toward Single Atom Chains with Exfoliated Tellurium". H. O. H. Churchill, G. J. Salamo, S.-Q. Yu, T. Hironaka, X. Hu, J. Stacy, and I. Shih.

4. Nano Lett., 16 (1), 504–511 (2016), "Defect-free self-catalyzed GaAsP/GaAs nanowire quantum dots grown on silicon substrate". J. Wu, A. Ramsay, A. M. Sanchez, Y. Zhang, D. Kim, F.S.F. Brossard, X. Hu, M. Benamara, M. Ware, Y. Mazur, G. Salamo, M. Aagesen, ZMM. Wang, and H. Liu.

5. AIP ADVANCES 3, 072112 (2013), "Molecular beam epitaxial growth of Bi2Te3 and Sb2Te3 topological insulators on GaAs (111) substrates: a potential route to fabricate topological insulator p-n junction". Z. Zeng, T. A. Morgan, D. Fan, C. Li, Y. Hirono, X. Hu, Y. Zhao, J. S. Lee, J. Wang, Z. M. Wang, S.Q. Yu, M. E. Hawkridge, M. Benamara and G. J. Salamo.

6. J. Vac. Sci. Technol. B 31, 03C105 (2013), "MBE Grown GaAsBi/GaAsDouble Quantum Well Separate Confinement Heterostructures". D. Fan, P. C. Grant, S.-Q. Yu, V. G. Dorogan, X. Hu, Z. Zeng, C. Li, M. E. Hawkridge, M. Benamara, Yu, I. Mazur, G. J. Salamo, S. R. Johnson, and Z. M. Wang.

7. Advanced Optical Materials, 1: 201–214 (2013), "Epitaxially Self-Assemblied Quantum Dot Pairs". J. Wu, X. Hu, J. Lee, E.-S. Kim, and Z. M. Wang.

8. Appl. Phys. Lett. 101, 181103 (2012), "Molecular Beam Epitaxy Growth of GaAsBi/GaAs/AlGaAs Separate Confinement Heterostructures". D. Fan, Z. Zeng, X. Hu, V. G. Dorogan, C. Li, M. Benamara, M. E. Hawkridge, Yu, I. Mazur, S.-Q. Yu, S. R. Johnson, Zh. M. Wang, and G. J. Salamo.

9. Appl. Phys. Lett. 99, 243113 (2011), "Bismuth nano-droplets for group-V based molecular-beam droplet epitaxy". C. Li, Z. Q. Zeng, D. S. Fan, Y. Hirono, J. Wu, T. A. Morgan, X. Hu, S. Q. Yu, Zh. M. Wang and G. J. Salamo.

10. M. Benamara, Y. I. Mazur, P. Lytvyn, M. E. Ware, V. Dorogan, X. Hu, L. D. de Souza, E. Marega, M. Theodores, G. Marques, and G. Salamo. (2015) 'Ordering of InGaAs Quantum Dots Grown by Molecular Beam Epitaxy under As2 gas flux', MRS Proceedings, 1792. doi: 10.1557/opl.2015.537.